UNIVERSITY OF CALIFORNIA
RIVERSIDE

Synthesis and Tunneling Spectroscopy of Tunable Materials for Topological Superconductivity

A Dissertation submitted in partial satisfaction
of the requirements for the degree of

Doctor of Philosophy

in

Physics

by

Cliff Chen

December 2021

Dissertation Committee:

Dr. Peng Wei, Chairperson
Dr. Yongtao Cui
Dr. Kirill Shtengel

The Dissertation of Cliff Chen is approved:

Committee Chairperson

University of California, Riverside

Acknowledgments

Chapter 6 is based on work the author published in ACS Applied Material Interfaces, reference [27].

The list of people who have helped me over my time at UCR is many, and here I give thanks. I would like to start by acknowledging my family for their continued support throughout my time at UCR, especially in of COVID-19 which came at such an unfortunate time. Graduate school is not easy and was never meant to be. Having a base of support back at home has always helped to ease the burden on my shoulders. Without their help this journey would not have been possible.

I would also like to thank my lab mate Jason Tran for his extensive help over the years. Although our PhD projects are very different, he has always been available to aid me in whatever my needs are (even on the weekends). Vacuum chamber maintenance, liquid Helium transfers, and general equipment troubleshooting are some of the many things we tackled together over the years. I hope that I have been able to help him as much as he has helped me. I will be forever grateful for having worked together with him.

Another group of important individuals that deserve acknowledgment are the facilities staff at UCR, particularly Dong Yan. Dong has always been diligent in his maintenance and upkeep of the cleanroom, even during the initial waves of COVID-19. Much of my research depended on usage of equipment in the nano-fabrication facility and without his continued support in keeping the lights on, I would not have been able to accomplish so much.

And last, but certainly not least, I would like to thank my advisor Peng Wei. I

appreciate his help over the years and his willingness to let me tackle problems on my own, something that not all advisors are willing to do with new students, especially if it is their first student. My time in his lab has certainly been a busy experience, from setting up equipment to mentoring new students, but that was not a bad thing. It is a one of a kind experience that can only happen at the conception of a lab, and with it comes a wealth of insight about what it takes to build a good lab. And for that I am very grateful.

To my family for all their support.

ABSTRACT OF THE DISSERTATION

Synthesis and Tunneling Spectroscopy of Tunable Materials for Topological Superconductivity

by

Cliff Chen

Doctor of Philosophy, Graduate Program in Physics
University of California, Riverside, December 2021
Dr. Peng Wei, Chairperson

This thesis presents experimental work on the synthesis and characterization of materials for topological superconductivity. First, an introduction to the theory of conventional and topological superconductors is presented along with an overview of current experimental work in the field. There are two main material systems considered in this work: Au (111) and $NbSe_2$ thin films. The Au (111) approach is a hybrid superconducting system that seeks to leverage the strong spin-orbit interaction in the surface states of Au (111) films to engineer Majorana zero modes. Tunneling experiments presented on these films reveal the presence of surface state superconductivity and enhanced Zeeman effect from large Landé g-factors. The $NbSe_2$ approach explores the synthesis of this material in wafer scale substrates and the effects of lattice strain on the superconducting properties of the films. Raman spectroscopy reveals that in-plane strain, controlled by synthesis temperature, is responsible for altering the electronic properties of the material.

Contents

List of Figures

Chapter 1

Introductions

1.1 In Search of Better Hardware

Quantum computers are heralded as the next paradigm for information technology. These new machines promise massive parallelism, exponential speedups, and super secure transfer of data as some of their key selling points. Large tech companies like Microsoft, Google, and IBM have certainly bought into the hype and are now big players in the quantum computing race. Google, for instance, reported the first demonstration of quantum supremacy using superconducting qubits [11]. Meanwhile IBM has brought their quantum services to the cloud where users can submit custom programs to be ran on actual quantum hardware [26]. In short, with so much money and manpower backing the field, it seems that achieving a reliable quantum computer isn't too far off in the future.

Of course, that doesn't mean there are no major hurdles in the way. It should come as no surprise that trying to build a computer using quantum mechanics was going to be a long climb upwards. Beneath the shiny veneer of quantum computing hype lies a

myriad of problems that stem from one core truism: quantum states are sensitive. In fact, the very act of measurement and the way one measures a quantum state changes the state itself [116]. Add on to this the fact that no human involvement is required for measurement as the environment is also a perfectly good measurer, it is becomes clear that steps must be taken to ensure the purity of quantum states [131]. Luckily, Peter Shor provides an answer to this problem of decoherence with the introduction of quantum error correction [151]. The idea is to redundantly encode information into multiple qubits upon which one can perform syndrome analysis to detect for errors and apply the appropriate operation to correct them. Problem solved, right?

Unfortunately, not quite. The need for more qubits means the need for more hardware, and the need for more hardware means the number of additional problems can scale faster than what the error correcting codes can handle. There are new correction schemes that can work with rather noisy qubits, but the fundamental problem of noisy qubits persists [44]. A new way to encode information in quantum hardware must be found, and that is the motivation for the work in this thesis.

Enter topology. Topology is the study of deformations or homeomorphisms as mathematicians would call them. The idea is that two objects, whether they be physical objects or mathematical objects, are "similar" if they can be deformed into one another. A common example is that a coffee mug is the same as a donut because the two objects possess a single hole. The only way to change the donut so that it is no longer homeomorphic to the coffee mug is to rip the donut apart. By doing so we have removed the property that ties two the objects together, a.k.a. the fact that there was a hole. This concept of

"holeness" is a topological property of both objects and cannot be removed under small perturbations; for example, simply stretching the donut doesn't remove the presence of the hole. Consequently, this suggests a unique way of storing information. Encoding data into the topological properties of the system can protect it from noise and extend its lifetime. That is, until the noise rises to the point that it changes the topology of the system, which is akin to ripping the donut.

Physicists have been taking advantage of topology to aid them in their studies of the universe for quite some time now. It shows up in many fields from classical electromagnetics to fluid dynamics to modern theory of superconductors. In fact, Gauss' law is an example of a topological concept in physics: any deformation of the Gaussian surface enclosing a charge will not change the value of the surface integral unless that deformation encapsulates new charge [154]. Similarly, Dirac has invoked topological arguments in an effort to address the existence of magnetic monopoles [59]. As this thesis will showcase, physicists have extended the use of topology to the study of the electronic properties of solids. The past couple of decades has resulted in new classifications of materials based on the topological nature of their electronic behavior. This new understanding has resulted in discoveries that leverage these topological properties to create robust qubits for quantum computing [71, 72]. We will explore one possible path in this thesis.

1.2 Overview of Thesis

We take a hardware approach to solve the noisy qubit problem, with an emphasis on exploring the fundamental electronic properties of topological superconducting materials.

A critical challenge that arises whenever building a new qubit is how to synthesize the required materials. This forms the first major body of work presented here. The second challenge is understanding how to engineer the correct physics in our materials to make them viable for quantum computing. This is an active area of research at many institutions, and we present our contributions to this effort.

Chapter 2 starts with a general overview of "conventional" superconductivity. Superconductivity has grown to encompass a wide variety of phenomena and we only cover certain parts. We introduce concepts from the semi-classical Ginzburg-Landau theory and expand upon them in the fully quantum BCS theory. Topics covered include: the superconducting order parameter and its symmetries, the influence of a magnetic field on a superconductor, Bogoliubov quasi-particles, and quantum tunneling of superconductors.

Chapter 3 introduces the theory behind topological superconductivity. We cover the origins of Majorana fermions and how they can appear in solid-state systems. From there we dive into the first theoretical realizations of Majorana fermions as well as subsequent experimental efforts taken to observe them in real life. We also introduce the material system covered in this thesis and the next steps being undertaken to improve it.

Chapter 4 explores the experimental methods used to synthesize and characterize the materials. This includes an overview of the growth methodology and the principles behind the proper synthesis of high-quality materials. We also discuss the cryostat and measurement electronics used to characterize the samples grown.

Chapter 5 presents the results of synthesis and tunneling spectroscopy measurements taken on Nb-Au films. We demonstrate the ability to grow high quality epitaxial

Au (111) thin films on sapphire. To study these films, we take a bit of an unconventional approach to fabricating tunnel junctions using silver paste. Such methodology is commonly used to create point contact junctions, but our results demonstrate that this can also be used to for tunneling by the additional deposition of an appropriate tunnel barrier material. Our devices demonstrate superconductivity in the surface bands of Au (111), and we discuss signatures of topological superconductivity.

Chapter 6 focuses on the growth and characterization of $NbSe_2$ thin films. $NbSe_2$ is a member of the transition metal dichalcogenide family, a group of compounds that are part of the "next-generation" of 2D materials after the discovery of graphene. We provide an overview of the interest in transition metal dichalcogenides and the properties that make $NbSe_2$ unique. We demonstrate the growth of $NbSe_2$ thin films and discuss how lattice strain can be used to control superconductivity in this material.

Chapter 7 concludes with some final thoughts about the work presented and the path moving forward.

Chapter 2

Superconductivity:

Ginzburg-Landau and BCS

Superconductors are materials that possess no electrical resistance once the temperature drops below a threshold known as the critical temperature. H. Kamelingh Onnes discovered this anomaly in 1911 when he dipped elemental mercury into liquid Helium and found the resistivity dropped to zero [163]. Since his discovery, the zoo of superconductors and the corresponding theory to describe them has grown immensely. Similarly, the field of superconducting electronics has equally grown to a large size with some of the most sensitive electronic detectors being made out of superconductors [23]. The purpose of this chapter is not to provide a thorough review of all types of superconductors, properties and their applications. Instead, we aim to review some of the basics regarding the essential physics of superconductors relevant to our discussion of topological superconductivity.

2.1 Ginzburg-Landau Approach to Superconductivity

One of the most celebrated semi-classical approaches to superconductivity comes from Ginzbug-Landau (GL) theory, named after Vitaly Ginzburg and Lev Landau. Their treatment of superconductivity was based on Landau's prior work on the theory of second-order phase transitions. The starting point is the concept of the order parameter which is a numeric quantity that is zero before the transition and non-zero after the transition. By studying behavior of this quantity, one can determine whether a transition has occurred as well as other details of the transition. A characteristic of GL theory for superconductors is that the order parameter is described by a *complex* number $\psi = \Delta e^{i\theta}$. Initially, this complex number was interpreted as a pseudo-wavefunction of the superconducting electrons with $|\psi|^2$ being the density n_s of the electrons. Later findings would prove this interpretation to be false, with BCS theory to provide a more apt description of the order parameter.

2.1.1 The Free Energy and Ginzburg-Landau Equations

Free Energy Expansion

The validity of Ginzburg-Landau (GL) theory rests on two assumptions:

1. The temperature of the superconductor is near the critical temperature or $|\frac{T-T_c}{T_c}| \lesssim 1$.

2. The order parameter ψ and electromagnetic fields do not have rapid spatial variations.

Due to these assumptions, GL theory works best as a phenomenological theory describing macroscopic behavior where the microscopic mechanics are not of crucial importance. We start our discussion with the Landau expansion of the Helmholtz free energy density of a superconductor [158]:

$$f_s = f_n + \alpha|\psi|^2 + \frac{\beta}{2}|\psi|^4 + \frac{1}{4m}|(\frac{\hbar}{i}\nabla - \frac{2e}{c}\mathbf{A})\psi|^2 + \frac{B^2}{8\pi} \tag{2.1}$$

Here α, β are the temperature dependent coefficients of the expansion with $\beta > 0$, and f_n is the free energy of the system in the non-superconducting state which we take to be constant. m, e refer to electron mass and charge respectively and $\mathbf{A}$ is the vector potential. From here a variety of macroscopic phenomena can be derived. As a simple exercise, we will show that superconducting transition is second-order with respect to temperature. Let's consider the case with zero fields and no gradients in the order parameter. Then the free energy expansion reduces to:

$$f_s = f_n + \alpha|\psi|^2 + \frac{\beta}{2}|\psi|^4 \tag{2.2}$$

The natural state of the system in thermal equilibrium is the one with the lowest free energy which guides us to search for the value of ψ that minimizes the above expression. Taking a derivative with respect to $|\psi|$ and setting the expression equal to zero, we arrive at:

$$0 = \alpha|\psi| + \beta|\psi|^3 \tag{2.3}$$

The value of $|\psi|$ depends crucially on the sign of α. If $\alpha > 0$, the minimum of eqn. 2.2 occurs at $|\psi| = 0$ which means that the system remains in the normal, non-superconducting state. On the other hand, $\alpha < 0$ implies f is minimized at $|\psi|^2 = -\frac{\alpha}{\beta}$. We can now Taylor expand the temperature dependent parameters α, β to 1st and 0th order respectively based on the assumption that we are below but close to the transition temperature to obtain:

$$|\psi| = \sqrt{\frac{-\alpha(T - T_c)}{\beta}} \qquad \alpha < 0,\ T < T_c \tag{2.4}$$

We see that as the temperature approaches T_c and moves below, α changes sign from positive to negative, and the order parameter smoothly transitions from zero to a nonzero value, characteristic of a 2nd order phase transition. This is clear from Figure 2.1 which shows $|\psi|$ increasing continuously from zero at the transition temperature T_c.

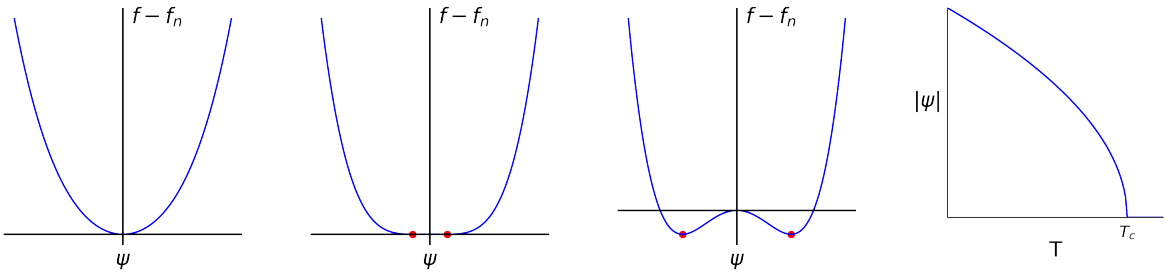

(a) $\alpha > 0, T > T_c$ **(b)** $\alpha \lessapprox 0, T \lessapprox T_c$ **(c)** $\alpha < 0, T < T_c$ **(d)** $|\psi|$ vs T

Figure 2.1: Evolution of free energy as α changes sign. The red dots indicate the new minimum when $\alpha < 0$. Figure (d) shows that the order parameter approaches zero continuously as $T \to T_c$

In addition, the above derivation also hints at another property of the superconducting transition, and that is the spontaneous breaking of a continuous symmetry, something found commonly in Landau's theory of phase transitions. Consider that we derived what value the magnitude $|\psi| = \Delta$ should take, but what about the phase? What value does it take on? The answer is whatever the system deems most favorable at the moment of the transition. This rather vague claim is due to the fact that the above free energy expression is dependent purely on the magnitude of the order parameter. As such, the free energy has a $U(1)$ symmetry; the phase is allowed to vary freely, and it will have no bearing on the transition. In reality, because the order parameter is complex, it still must acquire *some* phase after the transition, and it does so spontaneously by picking whatever value it deems worthy based on the current state of the material. Therefore, after the transition the system is no longer invariant under rotations of the phase. This symmetry breaking is intimately tied to the theory of Nambu-Goldstone modes [68, 20] which are low-energy excitations that appear whenever a continuous symmetry is broken.

The Ginzburg Landau Differential Equations

To work with more complicated situations involving fields and gradients, we turn to the Ginzburg-Landau differential equations. We derive these equations by minimizing the full free energy expression (2.1) with respect to both ψ and $\mathbf{A}$. It should be pointed out that we are minimizing with respect to the full order parameter ψ and not $\Delta = |\psi|$. This requires us to take the derivative with respect to ψ^*. Similarly, we minimize with respect to $\mathbf{A}$ through the transformation $\mathbf{A} \to \mathbf{A} + \delta\mathbf{A}$ and keep only the first order terms.

$$\frac{\delta f_s}{\delta \psi^*} = \alpha\psi + \beta\psi|\psi|^2 + \frac{1}{4m}(\frac{\hbar}{i}\nabla - \frac{2e}{c}\mathbf{A})^2\psi = 0 \tag{2.5}$$

$$\frac{\delta f_s}{\delta \mathbf{A}} = \frac{2e}{c}\left[\psi(\frac{\hbar}{i}\nabla + \frac{2e}{c}\mathbf{A})\psi^* - \psi^*(\frac{\hbar}{i}\nabla - \frac{2e}{c}\mathbf{A})\psi\right] - \nabla \times (\nabla \times \mathbf{A}) = 0 \tag{2.6}$$

Using the fact that $\mathbf{j} = \frac{c}{4\pi}\nabla \times \mathbf{B}$ and simplifying the algebra, we arrive at the Ginzburg-Landau equations [158].

$$\alpha\psi + \beta\psi|\psi|^2 + \frac{1}{4m}(\frac{\hbar}{i}\nabla - \frac{2e}{c}\mathbf{A})^2\psi = 0 \tag{2.7}$$

$$\frac{e\hbar}{2mi}(\psi^*\nabla\psi - \psi\nabla\psi^*) - \frac{2e^2}{mc}|\psi|^2\mathbf{A} = \mathbf{j} \tag{2.8}$$

From here we can actually derive a well known property of superconductors called flux quantization. Magnetic fields passing through an annulus made of superconducting material can only do so in integer spacing of $h/2e$ in SI units or $hc/2e$ in CGS units. Consider the situation shown in Figure 2.2.

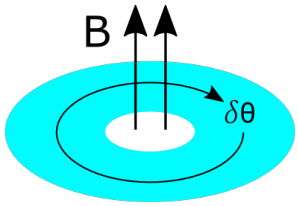

Figure 2.2: Magnetic field threading a superconducting annulus.

The circular geometry poses a particular constraint on the superconducting phase θ. Specifically, if one were to complete one full rotation around the annulus and add up all the differential changes in the phase, they would find that the total phase difference would be equal to an integer multiple of 2π. This has to be the case because the order

parameter must remain single valued. Should the phase differ by any other amount, this would result in an ambiguity as to what is the correct value of the order parameter at a particular location on the annulus. Mathematically, this constraint is equal to:

$$\oint \nabla\theta \cdot d\mathbf{l} = 2\pi n \tag{2.9}$$

Now we make use of equation 2.8. We assume that the magnitude of the order parameter does not vary along the path we take in the annulus; this is justifiable if we are deep within the superconductor where field effects are sufficiently screened out. Therefore, our order parameter has the spatial dependence: $\phi(\mathbf{r}) = \Delta e^{i\theta(\mathbf{r})}$. This allows us to rewrite equation 2.8 as

$$\mathbf{j} = \frac{e}{m}|\psi|^2(\hbar\nabla\theta - \frac{2e}{c}\mathbf{A}) \tag{2.10}$$

In addition, assume that no current is flowing in the region of the annulus where we take our circular path so that $\mathbf{j} = 0$. Then we get an expression for $\nabla\theta$ in terms of $\mathbf{A}$. Substituting this value of $\nabla\theta$ into the constraint equation gives:

$$\oint \nabla\theta \cdot d\mathbf{l} = 2\pi n = \oint \frac{2e}{\hbar c}\mathbf{A} \cdot d\mathbf{l} \tag{2.11}$$

$$\oint \frac{2e}{\hbar c}\mathbf{A} \cdot d\mathbf{l} = \int \frac{2e}{\hbar c}\mathbf{A} \cdot d\mathbf{S} = \frac{2e}{\hbar c}\Phi \tag{2.12}$$

$$\Phi = \frac{nhc}{2e} \tag{2.13}$$

We see that the flux threading the annulus is quantized in units of $hc/2e$ (CGS units). This quantization forms the basis for the detection and control of sensitive quantum

devices. The classic example is the superconducting SQUID which acts as a highly sensitive magnetometer enabling the detection of very small magnetic fields down to $10^{-13}\ T$ [39]. It also serves as the basis for the Little-Parks effect [92] in which the transition temperature of a superconducting ring varies periodically with the amount of magnetic flux threaded through the loop. This effect has been proposed as a means to detect unconventional superconductivity and novel pairing mechanisms [90]. Specifically, the Little-Parks effect is typically periodic in integer units of the flux quantum $n\Phi = nhc/2e$. However, different pairing mechanisms such as triplet pairing can result in a shift so that periodicity is now in units of half-integer flux quanta $(n + 1/2)\frac{hc}{2e}$ [54]. Furthermore, the precise threading of magnetic flux may allow for control over topological phase transitions for Majorana zero modes using flux-induced methods, but more remains to be seen on this front [162].

2.1.2 Superconductivity in Magnetic Fields

In the previous section, we touched on one interaction between the magnetic field and a superconductor. However, the situation dealt with the superconductor affecting the magnetic field in a region unoccupied by the superconductor itself. What are about the sections that are occupied? The answer is the Meissner effect. Shortly after Onnes' discovery of superconductivity, Walther Meissner found that superconductors expel magnetic fields from their interior, much like a Faraday cage shielding its innards from electrostatic fields [109]. This effect is caused by surface currents in the superconductor that create a diamagnetic response to cancel out the external magnetic field.

The effect is not perfect, however. The magnetic field does in fact penetrate into the superconductor but only a small distance λ, called the penetration depth, that is on the

order of tens to hundreds of nanometers. Furthermore, under suitably large magnetic fields the superconducting state will be broken and a return to the normal state will occur. The field at which this transition occurs is known as the critical field B_c and can be understood in terms of an energy argument. At low temperatures, the superconducting state is the default state because its free energy is lower in comparison to that of the normal state. As the magnetic field increases, the diamagnetic response of the superconductor also increases to maintain the shielding. At some point the energy gained by establishing the diamagnetism will put the free energy of the superconducting state above that of the normal state causing a phase transition back to the non-superconducting state. The critical field is thus the crossover point when the diamagnetic energy + the superconducting free energy surpasses that of the normal state:

$$F_s - F_n = -\frac{\alpha^2}{2\beta} = -\frac{B_c^2}{8\pi} \tag{2.14}$$

Here we used the fact that there is no field deep within a superconductor so equation 2.2 can be used to calculate the free energy difference $F_s - F_n$. We have also neglected any contributions to the free energy from the surface layer where the magnetic penetration takes effect assuming that the layer is thin relative to the bulk. The last equality is found through the fact that since $\mathbf{B} = 0$ inside the the superconductor, then $\mathbf{M} = -\mathbf{H}/4\pi$. Therefore, the work done to establish this magnetization is given as

$$-\int_0^H \mathbf{M} \cdot d\mathbf{H} = B^2/8\pi \tag{2.15}$$

This completes the result in equation 2.14. We refer to this "version" of the critical field as the thermodynamic critical field [158] as it is calculated based on an energy argument involving the thermodynamic potentials.

A Higher Critical Field for Parallel Orientations

One key aspect left out of the discussion so far is the geometry of the superconductor and its orientation with respect to the magnetic field. As we will derive shortly, a thin film of superconducting material oriented parallel to a magnetic field will have a higher critical field than if it was oriented perpendicularly. This enhancement of the critical field by proper orientation of a superconducting film is of crucial importance for the discussion of Majorana zero modes as it bolsters the ability to tune a topological phase transition without destruction of the superconducting state.

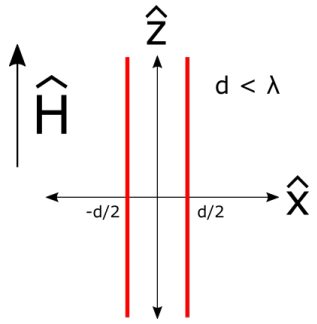

Figure 2.3: A thin superconducting film of thickness d lying y-z plane aligned parallel to an external magnetic field in the z-direction.

To see how this effect can occur using Ginzburg-Landau theory, we start by making a modification to the free energy density. So far, we have been working with the Helmholtz free energy density which is valid in situations in which $\mathbf{B} = \mathbf{H} + 4\pi\mathbf{M}$ is constant. In the

event that we wish to hold the external auxiliary magnetic field $\mathbf{H}$ constant as one would do in a laboratory setting, we need to use the Gibbs free energy density g instead. The two quantities are related as: $g = f - \mathbf{B} \cdot \mathbf{H}/4\pi$ [158].

With these changes in mind, consider Figure 2.3 where $\mathbf{H}_{ext} = H\hat{z}$ and our thin film lies in the y-z plane. We take the planar area of the film to be much greater than the thickness d and penetration depth λ so that our we can ignore boundary effects along the perimeter and focus on the bulk. We calculate the Gibbs free energy per unit area as:

$$G = \int_{d/2}^{-d/2} f - \mathbf{B} \cdot \mathbf{H}/4\pi \; dx \tag{2.16}$$

$$= \int_{d/2}^{-d/2} f_n + \alpha|\psi|^2 + \frac{\beta}{2}|\psi|^4 + \frac{1}{4m}|(\frac{\hbar}{i}\nabla - \frac{2e}{c}\mathbf{A})\psi|^2 + \frac{B^2}{8\pi} - \mathbf{B} \cdot \mathbf{H}/4\pi \; dx \tag{2.17}$$

To proceed further, we make an approximation of the magnetic field inside the superconductor. Specifically, we take $\mathbf{B} \approx \mathbf{H}_{ext}$. This approximation is valid since $d < \lambda$ so the sample does not develop a strong diamagnetic response meaning there is little field variation across the sample thickness. Therefore, we can take the London gauge in which $A_y = \int B \; dx \approx Bx$ holds true. We also neglect any variation in the phase of the order parameter so θ stays constant as well across the thickness. Completing the integration gives:

$$G = d\left[f_n + \alpha|\psi|^2 + \frac{\beta}{2}|\psi|^4 - \frac{H_{ext}^2}{4\pi}\right] + \frac{e^2 H_{ext}^2 d^3 |\psi|^2}{12mc^2} \tag{2.18}$$

Now the value of the order parameter is the one that minimizes this free energy so setting $\delta G/\delta|\psi| = 0$ and solving for $|\psi|$ to find the non-trivial solution:

$$|\psi|^2 = -\frac{\alpha}{\beta} - \frac{e^2 H_{ext}^2 d^2}{6mc^2} \tag{2.19}$$

The breakdown of superconductivity occurs when $|\psi| \to 0$. We set $\psi = 0$ and solve for H_{ext} to get:

$$H_{ext} = \sqrt{-\frac{6\alpha mc^2}{\beta e^2 d^2}} = \frac{\sqrt{24} H_c \lambda}{d} \tag{2.20}$$

The last equality made use of two facts:

1. Equation 2.4 showed that $-\alpha/\beta = |\psi|^2_{H=0} = n_s(H = 0)$.

2. The penetration depth can be defined in terms of the superconducting number density $n_s(H = 0)$ [73]: $\lambda = \sqrt{\frac{mc^2}{16\pi n_s e^2}}$

We see from equation 2.20 that the in-plane critical field is inversely proportional to the thickness d of the film. Thinner the sample, the higher the critical field. We also see that the value is proportional to the penetration depth λ. The relationship between these parameters and the critical field can again be understood in terms of an energy argument. With thin samples and large penetration depths, the external field enters the superconductor wholly. Therefore, as far as the external magnetic field is concerned, it does not "see" the superconductor which means there is very little diamagnetic response that would increase the free energy of the system. Consequently, the superconducting state remains the state with the lower energy and superconductivity is allowed to resist the deteriorating effects of the magnetic field. We will use this effect to our advantage when engineering topological superconductors.

2.2 BCS Theory of Superconductors

While Ginzburg-Landau theory was successful in its prediction of macroscopic superconducting phenomena, its validity holds only near the transition temperature where fluctuations in the order parameter is small. Furthermore, the theory is phenomenological and does not seek to provide a microscopic picture of what *causes* superconductivity, instead opting to describe the *effects*. The first truly "quantum" breakthrough in the theory of superconductivity came in 1957 thanks to Bardeen, Cooper, and Schrieffer [18]. They accurately proposed that superconducting currents were comprised of **pairs** of electrons, now called Cooper pairs, and that the formation of these pairs came as a result of electron-phonon interactions. Their pivotal work laid the groundwork for much of the modern theory of the microscopic physics of superconductors. In this section we will review through the salient portions of BCS theory relevant to our later discussion of Majorana zero modes.

Mean Field Hamiltonian and Canonical Transformation

We begin our discussion with the mean field BCS Hamiltonian also known as the Bogoliubov-de Gennes Hamiltonian. Derivation of this Hamiltonian can be found in reviews and lecture notes of BCS theory and we simply quote the result [157, 79]. It should be noted that this approach is different from the original derivation by Bardeen, Cooper, and Schrieffer who used a variational approach instead.

$$H_{BCS} = \sum_{\boldsymbol{k}} \left[\sum_{\sigma} \epsilon_{\boldsymbol{k}} c^{\dagger}_{\boldsymbol{k}\sigma} c_{\boldsymbol{k}\sigma} + \Delta c^{\dagger}_{\boldsymbol{k}\uparrow} c^{\dagger}_{-\boldsymbol{k}\downarrow} + \Delta^{*} c_{-\boldsymbol{k}\downarrow} c_{\boldsymbol{k}\uparrow} + \text{const.} \right] \tag{2.21}$$

Here $\epsilon_{\boldsymbol{k}} = \frac{\hbar^2 k^2}{2m} - \mu$ is the kinetic energy relative to the Fermi level μ. In addition, we no longer use ψ as our order parameter and instead use Δ as is traditional for BCS theory. Solutions to this Hamiltonian can be found via a canonical transformation known as the Bogoliubov-Valatin transform [22]. To complete this transform, we rewrite the first term in the Hamiltonian using the anti-commutation relations for fermionic operators: $\{c_{\boldsymbol{k}\sigma}, c^\dagger_{\boldsymbol{k'}\sigma'}\} = \delta_{\boldsymbol{k}\boldsymbol{k'},\sigma\sigma'}$ and the fact that the sum is over all $\boldsymbol{k}$.

$$H_{BCS} = \sum_{\boldsymbol{k}} \left[\epsilon_{\boldsymbol{k}} c^\dagger_{\boldsymbol{k}\uparrow} c_{\boldsymbol{k}\uparrow} + \epsilon_{\boldsymbol{k}}(1 - c_{-\boldsymbol{k}\downarrow} c^\dagger_{-\boldsymbol{k}\downarrow}) + \Delta c^\dagger_{\boldsymbol{k}\uparrow} c^\dagger_{-\boldsymbol{k}\downarrow} + \Delta^* c_{-\boldsymbol{k}\downarrow} c_{\boldsymbol{k}\uparrow} + \text{const.} \right] \tag{2.22}$$

We express this Hamiltonian now as a matrix equation and by solving for the eigenvalues and eigenvectors we can arrive at the Bogoliubov-Valatin transformation matrix that diagonalizes Hamiltonian.

$$H_{BCS} = \sum_{\boldsymbol{k}} \begin{pmatrix} c^\dagger_{\boldsymbol{k}\uparrow} & c_{-\boldsymbol{k}\downarrow} \end{pmatrix} \begin{pmatrix} \epsilon_{\boldsymbol{k}} & \Delta \\ \Delta^* & -\epsilon_{\boldsymbol{k}} \end{pmatrix} \begin{pmatrix} c_{\boldsymbol{k}\uparrow} \\ c^\dagger_{-\boldsymbol{k}\downarrow} \end{pmatrix} + \text{const} \tag{2.23}$$

We have absorbed the single $\epsilon_{\boldsymbol{k}}$ term into the constant as it simply provides an overall offset to the Hamiltonian. The energy eigenvalues can be easily solved for to obtain:

$$E_{\boldsymbol{k}} = \sqrt{\epsilon^2_{\boldsymbol{k}} + |\Delta|^2} \tag{2.24}$$

In addition, the eigenvectors are given as:

$$\gamma_{\boldsymbol{k}\uparrow} = u^*_{\boldsymbol{k}} c_{\boldsymbol{k}\uparrow} - v_{\boldsymbol{k}} c^\dagger_{-\boldsymbol{k}\downarrow} \tag{2.25}$$

$$\gamma_{-\boldsymbol{k}\uparrow} = v^*_{\boldsymbol{k}} c^\dagger_{\boldsymbol{k}\uparrow} - u^*_{\boldsymbol{k}} c_{-\boldsymbol{k}\downarrow} \tag{2.26}$$

$$|u_{\boldsymbol{k}}|^2 = \frac{1}{2}(1 + \frac{\epsilon_{\boldsymbol{k}}}{E_{\boldsymbol{k}}}) \tag{2.27}$$

$$|v_{\boldsymbol{k}}|^2 = \frac{1}{2}(1 - \frac{\epsilon_{\boldsymbol{k}}}{E_{\boldsymbol{k}}}) \tag{2.28}$$

Let's take some time to discuss the above results. First, the eigenvector solutions are known as Bogoliubov quasi-particles or Bogoliubons, and they are a superposition of both electrons and holes; this makes it obvious that these particles are not Cooper pairs since they can only be made of at most one electron. Second, these quasi-particles do not come for free: equation 2.24 shows that we must pay a minimum cost of Δ to create a Bogoliubon. As a result, the order parameter Δ is often referred to as the superconducting gap as it sets the energy gap that must be overcome to establish an excitation. The coefficients $u_{\boldsymbol{k}}$, $v_{\boldsymbol{k}}$ that appear in the eigenvectors are known as the coherence factors, and they set the relative weights of the electron and hole contributions. The behavior of the coefficients with respect to the kinetic energy $\epsilon_{\boldsymbol{k}}$ is plotted in Figure 2.4. As our kinetic energy moves above the Fermi level, the quasi-particles transition to a more electron-like character while below the Fermi level the particles behave more hole-like. Incidentally, this also shows that it is possible to achieve Bogoliubons with equally weighted electrons and holes. In other words, we have made a quasi-particle that can potentially act as its own anti-particle, something that is necessary in the formation of Majorana zero modes.

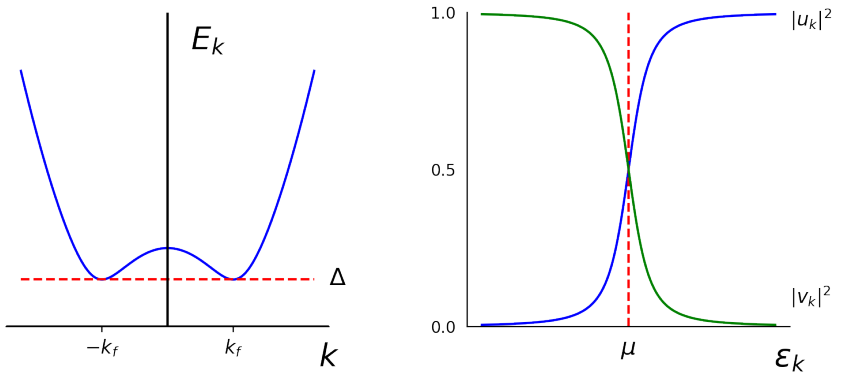

(a) Bogoliubon energy spectrum. **(b)** Coherence factor amplitudes vs ϵ_k

Figure 2.4: (a) Due to the presence of the superconducting gap, the energy spectrum is always non-zero. Here the Fermi level lies at E=0. (b) Below the Fermi energy, the coherence factor $|v_k|^2$ dominates and the quasi-particles are mainly composed of holes. At the Fermi energy, the quasi-particles are equally weighted superpositions of electrons and holes. Above, they are mostly electrons.

With these quasi-particle solutions, we can rewrite the mean field Hamiltonian in the following diagonal form:

$$H_{BCS} = \sum_{\boldsymbol{k},\sigma} E_{\boldsymbol{k}} \gamma^{\dagger}_{\boldsymbol{k}\sigma} \gamma_{\boldsymbol{k}\sigma} + \text{const.} \tag{2.29}$$

Now it becomes clear that under the Bogoliubov-Valatin transform that our Hamiltonian can be expressed in terms of non-interacting fermionic quasi-particles; this is because there are no off-diagonal terms that couple different quasi-particle operators. The form of this Hamiltonian is similar to that of the harmonic oscillator and suggests that the ground

state consists of no quasi-particle excitations. But, if the ground state has no quasi-particles, then what is it comprised of? The answer is Cooper pairs, and we will explore how the BCS ground state supports the creation of electron pairs in the next section.

Before we move on, there may be some confusion as to why equation 2.24 only has positive eigenvalues when there should also be a negative value as well due to the square root. The answer is that we are taking the perspective of Landau and view these quasi-particles as positive energy excitations above a ground state [156]. Therefore, instead of interpreting one of the eigenvector solutions as the creation of negative energy particles, we alternatively view it as the annihilation of positive energy particles. Many presentations of BCS theory take this excitation perspective and present the energies as such. Furthermore, some treatments purposefully double the degrees of freedom further by considering a duplicate set of quasi-particles but with negative energies. This is often done to aid in the mathematical treatment of the theory or interpretation of experimental data [40, 157].

2.2.1 BCS Ground State

Since the ground state contains no Bogoliubons, the corresponding wavefunction must act as a "vacuum" to the quasi-particle operators $\gamma_{\boldsymbol{k}\sigma}$. One way is to create such a wavefunction is to take advantage of the fact that the Bogoliubon operators obey fermionic commutation relations [34]:

$$|\Psi_{BCS}\rangle = \prod_{\boldsymbol{k}\sigma} \gamma_{\boldsymbol{k}\sigma} |0\rangle \tag{2.30}$$

Here the product is over all $\boldsymbol{k}$ and spin σ, and the $|0\rangle$ represents the true vacuum state. This wavefunction indeed behaves as a vacuum to the quasi-particles because acting on this state with $\gamma_{\boldsymbol{k}'\sigma}$ for any $\boldsymbol{k}'$ would result in a zero. This is due to the fact that the operator would anti-commute with all operators in the product resulting in a wavefunction that is equal to the negative of itself, hence it must be zero. One can now substitute in the definitions of the quasi-particle operators in terms of the electron operators to obtain the wavefunction as it is traditionally expressed [158, 18]:

$$|\Psi_{BCS}\rangle = \prod_{\boldsymbol{k}} (u_{\boldsymbol{k}} + v_{\boldsymbol{k}} c^{\dagger}_{-\boldsymbol{k}\downarrow} c^{\dagger}_{\boldsymbol{k}\uparrow}) |0\rangle \tag{2.31}$$

There are several key points to note about this wavefunction:

1. The wavefunction is comprised of Cooper pairs since it involves the creation of electrons in pairs at opposite momentum.

2. The coherence factor $v_{\boldsymbol{k}}$ sets the probability that a pair of electrons participates in the ground state while $u_{\boldsymbol{k}}$ is the probability that it does not. Incidentally, this also explains why as $v_{\boldsymbol{k}}$ increases in magnitude, the corresponding quasi-particle operator $\gamma^{\dagger}_{\boldsymbol{k}}$ gains more of a hole-like character. The reason is that the corresponding electron $c^{\dagger}_{\boldsymbol{k}}$ is more likely to be part of the ground state and not be available to participate in the superposition that forms the quasi-particle.

3. Not all pairs created are Cooper pairs. For electrons below the Fermi level deep in the Fermi sea, all nearby electron states are occupied. As a result, a phonon cannot scatter one electron state to another as it is already occupied. Only near the Fermi

level where there are empty states can the electron-phonon interaction take effect. Therefore, Cooper pairs are only formed from electrons near the Fermi surface.

4. The wavefunction has an indeterminate number of particles. Instead, if one were to expand the product, it can shown that the wavefunction is a superposition of all possible electron states with an **even** number of electrons occurring in pairs.

The evenness of the ground state means that adding an additional Cooper pair to a superconductor cannot change the fermion parity (even-oddness) of the system. Even the creation of a Bogoliubon in an *isolated* superconductor does not change the parity since it involves a Cooper pair breaking apart into *two* quasi-particles. In the case of topological superconductors, however, it is possible to end up with a ground state that can have even or odd parity [71, 47, 134]. This is due to the fact that Majorana zero modes are excitations at zero energy, allowing them to change the parity of the system without changing the energy.

2.2.2 The Energy Gap and its Symmetries

The energy gap Δ as presented so far has been a constant. In reality, the gap is in general a position or momentum dependent function [152]:

$$\Delta(\boldsymbol{r}) \propto \langle c_\downarrow(\boldsymbol{r}) c_\uparrow(\boldsymbol{r}) \rangle_T \tag{2.32}$$

$$\Delta(\boldsymbol{k}) \propto \sum_{\boldsymbol{k'}} V_{\boldsymbol{k}\boldsymbol{k'}} \langle c_{\boldsymbol{k}\downarrow} c_{-\boldsymbol{k}\uparrow} \rangle_T \tag{2.33}$$

Here $\langle ... \rangle_T$ represents a thermal average such as in statistical mechanics. We show the gap function in both its real and momentum space versions. The key point of emphasis

here is that because the gap function depends on the electron operators $c_{\boldsymbol{k}}$, it must also obey the same the symmetry requirements under exchange of these operators. In particular, the gap function follows the SPOT principle[91]: the gap function, and consequently the wavefunction of the Cooper pairs, must remain anti-symmetric under spin S, parity P, orbit O, and time T permutation operations; this can be expressed as $SPOT = -1$. This implies that either one or three of these possible permutations must be anti-symmetric. Different combinations of which ones are anti-symmetric and which ones are not lies at the heart of unconventional superconductivity [153].

Equations 2.32, 2.33 show the gap function for a superconductor that obeys one type of pairing relation. In this case, it pairs electrons of opposite spin which means that the Cooper pairs have a singlet spin wavefunction. This is common for superconductors whose gap functions are equal to a constant, also known as s-wave superconductors; as a result, the spin part of the gap function carries the anti-symmetry property. In general, determining the precise $\boldsymbol{k}$-dependence of Δ is a non-trivial task, and it is common to work with a form of the gap function that is expanded to low orders in $\boldsymbol{k}$ [170, 160, 134]. Some choices for the functions are:

$$\Delta(\boldsymbol{k}) \propto \begin{cases} \text{const.} & \text{s-wave} \\ k_x + ik_y & \text{2D chiral p-wave} \\ cos(k_x) - cos(k_y) & \text{2D } d_{x^2-y^2}\text{-wave} \end{cases} \tag{2.34}$$

For our discussion of Majorana zero modes in 1D nano-wires, the gap function will have a p-wave symmetry with $\Delta \propto sin(k)$. This choice of pairing is key to achieving Majoranas in nano-wire setups because it is odd in k which guarantees that $\Delta \to 0$ as

$k \to 0$. The vanishing of the gap ensures that the quasi-particle band structure cannot be adiabatically connected to a trivial Bose-Einstein condensate which means that the superconductor remains topological [71, 8]. The existence of solid-state superconductors with intrinsic p-wave symmetry is still debated with some experimental evidence supporting their existence [100]. However, such materials are not needed for Majorana zero modes as it has been shown that it is possible to engineer effective p-wave pairing by combining conventional materials in the right way [6].

2.2.3 Density of States and Tunneling Into Superconductors

The existence of the energy gap Δ in a superconductor has consequences for its quasi-particle density of states. When the superconducting gap forms, it must expel all single electron states from that region of the energy diagram. So what happened to those states that were present before the superconducting transition? The answer is that they are pushed to the edges of the gap causing a spike in the density of states near the gap as we will show.

To derive the new density of states, we can use the fact that the total number of single electron states is conserved [158]. This is because the electron operators $c_{\boldsymbol{k}}$ are connected to the new quasi-particle operators $\gamma_{\boldsymbol{k}}$ via a unitary transform (Bogoliubov-Valatin transform) which is an isomorphism and must preserve the number of states. Consequently, the states within an interval $d\epsilon$ before the transition must map onto quasi-particle states that live in an interval dE after the transition. Here ϵ and E refer to the energies of the states in the normal and superconducting state respectively. This implies the following relation:

$$D_n(\epsilon)d\epsilon = D_s(E)dE \Rightarrow D_s(E) = D_n(\epsilon)\frac{d\epsilon}{dE} \tag{2.35}$$

We make the approximation that $D_n(\epsilon) \approx D_n(\mu)$ since we only care about the states close to the Fermi level μ. Therefore, the normal density of states can be approximated as a constant. Working out $d\epsilon/dE$, we find:

$$D_s(E) = \begin{cases} D_n(\mu)\frac{E}{\sqrt{E^2-|\Delta|^2}} & E > |\Delta| \\ 0 & E < |\Delta| \end{cases} \tag{2.36}$$

Figure 2.5a shows the classic gap feature associated with superconductors where there is a spike near the gap edges.

Tunneling Spectroscopy

The density of states can be directly observed using tunneling probes in which the differential conductance of the probe is proportional to the density of states of the superconductor. To see how this can occur, consider the situation shown in Figure 2.5b in which a normal metal is separated from a superconductor by a thin barrier that allows electrons to tunnel through:

Here we consider the semiconductor model of tunneling [158]. This means that electrons undergo elastic transitions from one material to the other after accounting for the applied potential difference eV. In addition, the density of states of the superconductor is reflected about the chemical potential. This is akin to doubling the degrees of freedom and treating the negative energy Bogoliubons as being a completely filled Fermi sea. Our

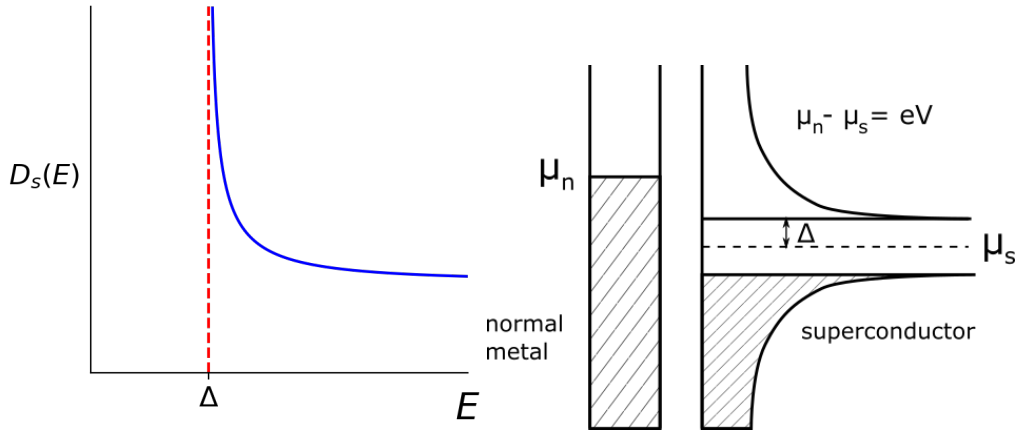

(a) Superconductor density of states **(b)** Tunneling diagram of a NIS junction

Figure 2.5: (a) Below the gap Δ, there are no available quasi-particle states. The states that were present in the gap before the superconducting transition are pushed to side causing a spike in the density of states near the gap edge. (b) Semiconductor-model of tunneling into a superconductor. The density of states for the superconductor is doubled with the bottom half filled up to form a Fermi sea. Electrons from the normal metal can tunnel horizontally to the empty states in the superconductor.

energy scale is measured relative to the Fermi level of the normal metal. We can express the current flowing from the normal metal to the superconductor as follows:

$$I_{n\to s} \propto \int |t|^2 D_n(E) f_n(E) D_s(E+eV)(1-f_s(E+eV))dE \tag{2.37}$$

This equation expresses the electrical current as a probability current. The chance for an electron to hop over is equal to: probability that initial state has an electron available $f_n(E) \cap$ probability of tunneling $|t|^2 \cap$ probability that final state is empty to receive the electron $1-f_s(E+eV)$. Upon integration over all possible states, we get the current in one

direction. The total current flowing through the interface must include the reverse current $I_{s\to n}$ as well:

$$I_{tot} = I_{n\to s} + I_{s\to n} \propto \int |t|^2 D_n(E) D_s(E+eV)(f(E) - f(E+eV))dE \tag{2.38}$$

$$f(E) = \frac{1}{1+e^{E/k_b T}} \tag{2.39}$$

Here we assume that the Fermi-Dirac distribution works well for the electron distribution functions in the normal metal and superconductor. To see how the density of states can be extracted, we approximate the normal metal's DOS as a constant as before and consider the differential conductance dI/dV:

$$G = dI/dV \propto D_n(\mu)|t|^2 \int D_s(E)(-\frac{\partial f(E+eV)}{\partial(eV)})dE \tag{2.40}$$

Our final result shows that the differential conductance is simply the density of states of the superconductor convolved with the derivative of the Fermi-Dirac function. This derivative is Gaussian-like and accounts for the thermal broadening associated with finite temperatures. In the limit $T \to 0$, the conductance will approximate the DOS of the superconductor very well. For topological superconductors, it has been theoretically predicted that tunneling into a Majorana zero mode will give a quantized conductance of $2e^2/h$ at zero bias (V = 0) [86].

Chapter 3

Topological Superconductivity

In recent decades, it has become clear that topology can play a powerful role in determining the electronic behavior of solids. The rise of topological insulators, magnetic skyrmions, topological superconductors, etc. are testament to the ever growing use of topology to discover new quantum excitations in solids [108, 132, 57]. One of the driving forces behind the interest in these topological excitations is the fact that they are governed by global properties of the system rather than local effects. As a result, they are naturally robust against perturbations. The focus of this chapter is to explore one of these topological particles called Majorana zero modes and see how they arise in superconducting systems.

3.1 The Original Majorana Fermions

The origin of Majorana fermions dates back to the 1930s to the nascent period of quantum field theory. It is around this time that Italian physicist Ettore Majorana stepped into the scene with a modification of Dirac's equation. In particular, he recognized the

importance of a specific representation of the matrices used in Dirac's equation [40]. This subtle change enabled his discovery of the particle that bears his name.

$$(i\gamma^\mu \partial_\mu - m)\psi = 0 \tag{3.1}$$

Here $\partial_\mu = (\partial_t, -i\partial_x, -i\partial_y, -i\partial_z)$ and γ^μ are a set of 4×4 matrices known as the Dirac matrices. Note that we have set $\hbar = 1$ as is standard with particle physics discussions. The γ^μ do not have a unique form. In particular, Majorana chose the matrices to be purely imaginary:

$$\gamma^0 = i\begin{pmatrix} 0 & -\sigma^1 \\ \sigma^1 & 0 \end{pmatrix} \qquad \gamma^1 = i\begin{pmatrix} 0 & \sigma^0 \\ \sigma^0 & 0 \end{pmatrix}$$

$$\gamma^2 = i\begin{pmatrix} \sigma^0 & 0 \\ 0 & -\sigma^0 \end{pmatrix} \qquad \gamma^3 = \begin{pmatrix} 0 & \sigma^2 \\ -\sigma^2 & 0 \end{pmatrix}$$

Here the σ^μ are the 2×2 Pauli matrices with σ^0 being the identity and $\sigma^{(1,2,3)} = \sigma^{(x,y,z)}$. This choice for the Dirac matrices makes the Dirac equation real with ψ being a purely real solution. Furthermore, the Dirac equation decouples into two independent sets of uncoupled equations.

$$(i\partial_t - \boldsymbol{p} \cdot \boldsymbol{\sigma})\psi_r - im_r\sigma_2\psi_r^* = 0 \tag{3.2}$$

$$(i\partial_t - \boldsymbol{p} \cdot \boldsymbol{\sigma})\psi_l - im_l\sigma_2\psi_l^* = 0 \tag{3.3}$$

Since the two sets of equations are uncoupled, the "mass" term is allowed to be different for each set. We won't solve the equations here, but instead we highlight some properties manifest within Majorana's equation that carry over to the condensed matter version.

1. The reality of ψ_r and ψ_l implies that these fields are invariant under charge-conjugation symmetry meaning these particles are their own anti-particles.

2. Majorana's equations are no longer invariant under the substitution: $\psi \to \psi e^{i\theta}$ with θ being a real constant. This means the particles do not have a gauge symmetry that supports coupling to the electromagnetic field and, thus, the particles are charge-neutral.

3. When discussing solutions to the Majorana equation, the spinor fields ψ_r and ψ_l are sometimes written in a 4-component form as:

$$\Psi_l = \begin{pmatrix} -i\sigma^2\psi_l^* \\ \\ \psi_l \end{pmatrix} \qquad \Psi_r = \begin{pmatrix} \psi_r \\ \\ i\sigma^2\psi_r^* \end{pmatrix} \tag{3.4}$$

   This form may seem unusual since it artificially doubles the degrees of freedom but writing it as such comes naturally in superconducting systems as we will see shortly.

3.2 Majorana Fermions in Solids

The prior section examined Majorana fermions as individual particles in their own right. In solids, however, the only genuine particles are the electrons and ions that make up the atoms. This certainly does not mean that Majorana fermions cannot appear

in solids, rather they will manifest as quasi-particles. Unsurprisingly, Majorana fermions naturally arise in superconducting materials. The Bogoliubov-de Gennes (BdG) formalism of superconductivity easily facilitates a description of quasi-particles that includes Majorana fermions. To see this, we follow reference [40] and write the mean-field Hamiltonian in real-space:

$$\mathcal{H} = \int d\boldsymbol{r} \left[\sum_{\sigma} (-\frac{\hbar^2}{2m}\nabla^2 - \mu) c_{\sigma}^{\dagger}(\boldsymbol{r}) c_{\sigma}(\boldsymbol{r}) + \Delta(\boldsymbol{r}) c_{\uparrow}^{\dagger}(\boldsymbol{r}) c_{\downarrow}^{\dagger}(\boldsymbol{r}) + \Delta^*(\boldsymbol{r}) c_{\uparrow}(\boldsymbol{r}) c_{\downarrow}(\boldsymbol{r}) \right] + \text{const.} \tag{3.5}$$

To write this in matrix form like equation 2.23, we define a 4-component column vector known as a Nambu spinor:

$$\Psi(\boldsymbol{r}) = \begin{pmatrix} c_{\uparrow}(\boldsymbol{r}) \\ c_{\downarrow}(\boldsymbol{r}) \\ c_{\downarrow}^{\dagger}(\boldsymbol{r}) \\ -c_{\uparrow}^{\dagger}(\boldsymbol{r}) \end{pmatrix} = \begin{pmatrix} \psi(\boldsymbol{r}) \\ i\sigma_y \psi^{\dagger}(\boldsymbol{r}) \end{pmatrix} \tag{3.6}$$

It should be noted that in defining this column vector, we have doubled the degrees of freedom. Specifically, $c_{\downarrow}(\boldsymbol{r})$ is not independent from $c_{\downarrow}^{\dagger}(\boldsymbol{r})$ since the two are related by Hermitian conjugation. Therefore, the number of eigenvectors and eigenvalues we obtain will be doubled and only half of the solutions will be independent and physical; in other words, there will be two solutions that refer to the *same* quantum state. This redundancy gives rise to charge conjugation or particle-hole symmetry in superconductors as shown below.

Using this vector we can write the Hamiltonian as:

$$\mathcal{H} = \int d\boldsymbol{r}\Psi^{\dagger}(\boldsymbol{r}) \begin{pmatrix} (-\frac{\hbar^2}{2m}\nabla^2 - \mu) & \Delta(\boldsymbol{r}) \\ \Delta^*(\boldsymbol{r}) & -\sigma_y(-\frac{\hbar^2}{2m}\nabla^2 - \mu)\sigma_y \end{pmatrix} \Psi(\boldsymbol{r}) + \text{const.} \tag{3.7}$$

One can diagonalize this Hamiltonian like we did for equation 2.23 to derive the eigenvector solutions. We will not do this here and instead discuss a bit more on the Nambu spinor. In defining this vector, one can already see some similarities to the spinor fields in equation 3.4. In particular, the Nambu spinor is invariant under charge conjugation $\mathcal{C}$.

$$\mathcal{C}\Psi(\boldsymbol{r}) = \tau_y\sigma_y(\Psi^{\dagger}(\boldsymbol{r}))^T = \Psi(\boldsymbol{r}) \tag{3.8}$$

$$\tau_y\sigma_y = \begin{pmatrix} 0 & 0 & 0 & -1 \\ 0 & 0 & 1 & 0 \\ 0 & 1 & 0 & 0 \\ -1 & 0 & 0 & 0 \end{pmatrix} \tag{3.9}$$

Here τ_y and σ_y refer to the Pauli matrices in particle-hole and spin space respectively. Specifically, τ_y acts on the upper and lower halves of the Nambu spinor while σ_y acts on the operators within the halves. This invariance automatically implies that superconducting systems are capable of supporting excitations that are their own anti-particle. Furthermore, this also implies that these particle are charge neutral. This shouldn't be too surprising since the previous discussion of BCS theory showed that it was possible to achieve Bogoliubons with equal superpositions of electrons and holes. The formalism here simply highlights this fact more readily.

However, just because a superconductor can support particles that are their own anti-particles does not mean that it is topological. We saw earlier that BCS theory requires quasi-particles to pay an energy price of Δ to exist. Majorana zero modes, on the other hand, are zero-energy excitations that live right at the Fermi level. In fact, the requirement of zero energy inherently guarantees that the excitation is its own anti-particle via charge conjugation symmetry of the Hamiltonian [9, 40]. This property means that for every eigenstate with energy E, there is another eigenstate with energy $-E$; negative energy is considered here because we have artificially doubled the degrees of freedom with the Nambu spinor. Therefore, zero energy particles will consequently end up as their own charge-conjugate partner, a.k.a. their own anti-particle. In general, an operator that creates a Majorana zero mode must obey [141]:

$$\hat{\gamma},\ \hat{\gamma}^2 = 1,\ [\hat{H}, \hat{\gamma}] = 0 \tag{3.10}$$

The question now is: what has to occur for our system to support these kinds of operators? The answer to this question was kindly provided by Alexei Kitaev in his toy model of a superconducting nano-wire which will be covered below [71].

3.3 Kitaev's Nanowire

This section will be based largely on Kitaev's paper on unpaired Majorana fermions [71]. As it turns out, creating an operator that satisfies the first two conditions of equation 3.10 is not difficult. It is actually a simple mathematical exercise to define new fermionic creation/annihilation operators $\gamma, \gamma^\dagger$ that obey the Majorana rules in terms of the old fermionic operators $c, c^\dagger$.

$$\gamma_1 = c + c^\dagger \tag{3.11a}$$

$$\gamma_2 = -i(c - c^\dagger) \tag{3.11b}$$

$$c = (\gamma_1 + i\gamma_2)/2 \tag{3.11c}$$

$$c^\dagger = (\gamma_1 - i\gamma_2)/2 \tag{3.11d}$$

We refer to these new operators as Majorana operators, and we need *two* of them to define a single Dirac operator c. This forms the basis for why Majorana zero modes can only appear in pairs, and it is also the reason why they are often referred to as "half" of an electron. We will now use these operators to write down the Hamiltonian for a 1D lattice chain that is the basis for Kitaev's nano-wire.

$$H = \sum_i \left[-\mu(c_i^\dagger c_i - \frac{1}{2}) - t(c_i^\dagger c_{i+1} + c_{i+1}^\dagger c_i) + \Delta c_i c_{i+1} + \Delta^* c_i^\dagger c_{i+1}^\dagger \right] \tag{3.12}$$

$$H = \frac{i}{2} \sum_i \left[-\mu\gamma_{i,1}\gamma_{i,2} + (t + \Delta)\gamma_{i,2}\gamma_{i+1,1} + (-t + \Delta)\gamma_{i,1}\gamma_{i+1,2} \right] \tag{3.13}$$

This Hamiltonian describes the lattice in Figure 3.1. We will not solve for the energy eigenstates here but instead highlight two distinct regimes of this system. Consider equation 3.13 in two scenarios:

1. $t, \Delta = 0, \mu < 0$. The Hamiltonian reduces down to a simple harmonic oscillator like form reminiscent of the diagonalized BCS Hamiltonian 2.29. The ground state is therefore a state that is empty of any particles occupying the lattice. This is the trivial state.

2. $|\Delta| = t > 0, \mu = 0$. Then the Hamiltonian becomes $H = it\sum_i \gamma_{i,2}\gamma_{i+1,1}$. This Hamiltonian is very similar to the trivial case except that the pairing occurs for operators γ from *different* lattice sites. This also means that the Majorana operators at the ends of the lattice are left out of the Hamiltonian as they have no neighboring partners. However, they do not "disappear" so to speak because the total number of Majorana operators must be conserved; each lattice sites provides two Majorana fermions so to have two Majoranas disappear would imply a lattice site suddenly vanished which is unphysical. Rather, they combine to form a highly non-local fermion that is localized at the ends of the wire with an energy of zero; the zero energy cost is why the operators are "zeroed" out of the Hamiltonian. This is the topological state of the nano-wire.

Scenario 2 is important for the observation of single Majorana fermions because the definition of the Majorana operators in equation 3.11 makes no indication that the corresponding particles should be spatially separated. This is the reason why Majorana

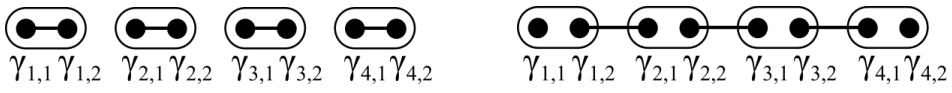

(a) Trivial Phase **(b)** Topological Phase

Figure 3.1: The lattice structure for Kitaev's 1D nano-wire. Each lattice site (indicated by the oval, corresponding to operator c_i) contains two Majorana fermions $\gamma_{i,1}, \gamma_{i,2}$. (a) In the trivial phase, the Majoranas pair within each lattice site as indicated by the black line connecting them. (b) The topological phase has the Majoranas pair between lattice sites. As a result, the Majoranas at the ends of the wire are left unpaired. The appearance of these edges states is what separates the trivial and topological phases of the wire despite the bulk pairing appearing to be the same.

zero modes are difficult to come by: they just pair up with their partner Majorana and form a regular Dirac fermion. It is under this new pairing that we have truly bisected a Dirac fermion such that the pair of Majoranas appear far apart from each other.

The presence of the Majorana edge state also has consequences for the ground state of the system. In the original BCS theory, the ground state 2.31 only contained an even number of electrons (fermions) because the base particles were Cooper pairs. However, Majorana zero modes have zero energy and thus live at the Fermi level with the Cooper pairs for free. This means the ground state in the topological phase can support an odd number of fermions, and the ground state manifold becomes degenerate with respect to fermion parity. Manipulating the fermion parity of the system via topological phase transitions serves as the basis for topological quantum computation as we will discuss in a later section.

Interestingly enough, the existence of these edge modes can also be determined from studying the bulk properties. The excitation spectrum of the bulk is:

$$E = \pm\sqrt{(2tcos(k) + \mu)^2 + 4|\Delta|^2 sin^2(k)} \tag{3.14}$$

Here k lives in the 1st Brillouin zone with $-\pi \leq k \leq \pi$. This spectrum is markedly different from the Bogoliubon spectrum 2.24. In particular, the second term with the energy gap Δ is now k dependent, and it is an odd function of k which guarantees the energy spectrum closes(go to zero) at $k = 0, k = \pi$ under suitable tuning of the parameters μ, t. The gap closing signals a topological phase transition by changing the sign of the topological invariant:

$$Z(H) = sgn(\mathrm{Pf}\, H(k = 0))sgn(\mathrm{Pf}\, H(k = \pi))) \tag{3.15}$$

Here Pf stands for the Pfaffian operation, and it has the relation $(\mathrm{Pf}\, M)^2 = det(M)$ for a skew-symmetric matrix M. Just to clarify the notation above, equation 3.15 is the product of the signs of the Pfaffian of the Hamiltonian at $k = 0$ and $k = \pi$. This quantity is known as a topological invariant, and, in this case, it is a $\mathbb{Z}_2$ invariant meaning it has two possible values, ± 1; 1 is trivial, -1 is topological. In general, topological invariants are used to classify mathematical structures based on homeomorphisms [132]. In other words, two objects A, B are the "same", share the same value of the topological invariant, if there exists a continuous, invertible transformation (homeomorphism) $f : A \leftrightarrow B$ that changes A to B and vice versa. In the discussion of topological superconductors and insulators, the object in question is the Hamiltonian, and two Hamiltonians are topologically equivalent if

it is possible to smoothly transform one Hamiltonian into the other without closing the bulk gap. In general, the topological invariant cannot change unless the bulk gap closes. As a result, if two regions of the system possess different topological invariants, whether these are regions in real space or parameter space, a gap closing must occur at the transition between these two spaces. This gives rises to the commonly found edge states seen in topological insulators [67]. The correlation between the bulk gap closing and edge states is known as the bulk-edge (bulk-boundary) correspondence principle [145, 9].

In our case, the invariant changing sign indicates the closing of the bulk spectrum gap and vice versa. Shown in figure 3.2, as we tune the parameters μ, t, the bulk spectrum closes first at $k = 0$, opens up, and then closes again at $k = \pi$. At each gap closing, the Pfaffian changes sign signaling the transition to and from the topological phase. The change in sign is tied to the particle-hole symmetry of the Hamiltonian. At finite k, the states with energy E have a particle-hole symmetric partner with energy $-E$. The two exceptions to this rule are the states at $k = 0, k = \pi$; these states map onto themselves under charge conjugation. Since the Pfaffian is related to the determinant, which is a product of all the energy eigenvalues, this means that at finite k the eigenvalues occur in $\pm$ pairs. Therefore, a gap closing at finite k would not be able to change the Pfaffian since the eigenvalues transform as $E \to -E$ and $-E \to E$, thus preserving the sign of the product. At $k = 0, k = \pi$ however, there are no pairs of energy eigenvalues since these states map onto themselves. Therefore, the gap closing at these k values is allowed to change the sign of the Pfaffian. This is why p-wave superconductivity is crucial for the appearance of Majorana zero modes: it makes Δ an odd function of k which in turn ensures the bulk gap can close

at $k = 0$ and thus change the value of the topological invariant.

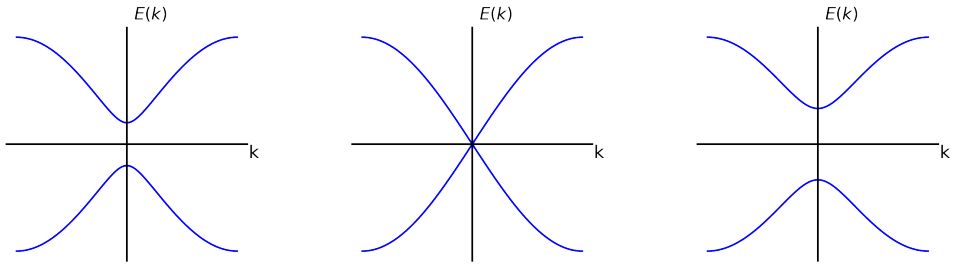

(a) $\mu = -3t$

Trivial

(b) $\mu = -2t$

Phase Transition

(c) $\mu = -1t$

Topological

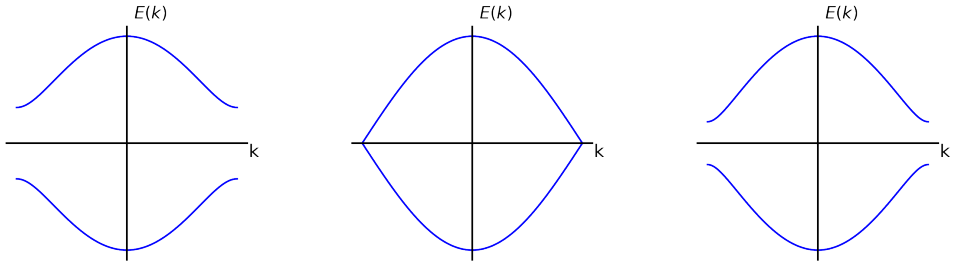

(d) $\mu = 1t$

Topological

(e) $\mu = 2t$

Phase Transition

(f) $\mu = 3t$

Trivial

Figure 3.2: Evolution of the nano-wire's bulk spectrum as we tune the Hamiltonian parameters μ, t. The phase transition occurs when the bulk gap closes (goes to zero) in (b), (e). After the closing in (b), the gap reopens and the wire enters the topological regime (c), (d) with the appearance of Majorana zero modes along the edges.

One useful simplification of the topological invariant is found when the superconducting gap Δ is much smaller than the other energy parameters in the system. Then

equation 3.15 simplifies to equation 3.16 in which v represents the number of Fermi points of the system in the normal state in the interval $(0, \pi)$ [40, 71]. This provides a simply guide to identifying possible 1D topological superconductors: simply look for systems in which it is possible for one to occupy an odd number of Fermi points in the right half of the Brillouin zone. We will see how to engineer this scenario when discussing the nano-wire approach to Majorana zero modes. This criterion only applies to fully gapped systems however.

$$Z = (-1)^v \tag{3.16}$$

One may wonder now about the stability of the topological phase. Is it possible to destroy the Majorana zero modes with small perturbations to the Hamiltonian? The answer, thankfully, is no. One cannot move the Majoranas away from zero energy individually; doing so would violate particle-hole symmetry as one Majorana would remain at zero but its particle-hole symmetric partner would be at finite energy [9]. Therefore, one must couple the Majoranas if one wishes to move these particles away from the Fermi level. However, the presence of the bulk gap means that there are no zero-energy excitations in the bulk that can couple the Majorana zero modes, and the spatial separation of the modes prevents any meaningful overlap of the wavefunctions. Therefore, the Majorana fermions are protected both energetically and spatially. This level of protection naturally means that Majorana zero modes possess long lifetimes which is why they are incredibly attractive for use in quantum computation.

3.4 Detecting Majorana Zero Modes

Now that we know it is possible to achieve Majorana zero modes theoretically, how do we experimentally confirm their existence? There are a number of detection schemes available, but, for the sake of brevity, we highlight three approaches to tackling this problem: tunneling, Josephson effects, and Majorana-based teleportation.

Tunneling spectroscopy is one of the most common ways experimentalists use to probe for Majorana fermions. It was theoretically predicted that tunneling into a Majorana bound state should result in a conductance peak at zero bias whose amplitude should be equal to exactly $2e^2/h$ [86]. The idea is that when the bias voltage V is below the gap $|\Delta|$, there can only be two possible scattering processes available: normal reflection and Andreev reflection. Normal reflection simply sends the electron back to where it came, but Andreev reflection is a special process only available in superconductors. In this unique scenario, the incident electron drags a partner electron from below the Fermi level to form a Cooper pair and enter the superconductor while producing a hole that is backscattered away in the tunneling lead. Normally Andreev reflection is suppressed in tunnel junctions by the presence of the barrier, but a Majorana bound state modifies the scattering process by raising the Andreev reflection probability to unity at zero bias resulting in a perfect conductance channel of $2e^2/h$. Away from $V = 0$ but $V < |\Delta|$, the conductance quickly drops to zero due to the lack of available states and the presence of the barrier preventing further Andreev reflection. In terms of experimental progress using tunneling, the results have been promising but also inconclusive. We will discuss more on the shortcomings of this approach in the context of semiconducting nano-wires in the next section.

Another direction for detection is to analyze the effects of Majorana fermions on Josephson effects. This approach was relevant before tunneling signatures came into picture. In Kitaev's original paper [71], he showed that when two p-wave superconductors are connected by a narrow quantum wire, the current-phase relation is 4π periodic instead of the conventional 2π periodicity; this is commonly dubbed the "fractional" Josephson effect. The reason is that the supercurrent passing across the junction is carried by *single* electrons as opposed to Cooper pairs. The effect is valid in both DC and AC cases, although in the AC case, the frequency of oscillation, $eV/\hbar$, needs to be set such that the junction evolves adiabatically with the occupation of the Andreev bound states in the junction unchanged [82]. On the other hand, in the limit of short junctions in which there is overlap of the Majorana wavefunctions, non-adiabatic transitions are required to restore the 4π effect [37]. The fractional Josephson effect further extends to modifying the I-V relation as well since phase and voltage in a Josephson junction are related as $2eV/\hbar = d\phi/dt$. Consequently, Shapiro steps can also be used as a measure of Majorana zero modes [147, 158]. This effect occurs when the junction is irradiated with photons and the Josephson frequency is equal to an integer multiple of the photon frequency: $n\omega_p = 2eV/\hbar$. The result is a series of step structures in the I-V curve (or spikes in the dI/dV) of the junction. With the 4π effect in place, the steps only appear for even integer multiples of the photon frequency resulting in missing steps in the Shapiro staircase [64]. Some experimental work confirmed missing Shapiro steps in Josephson junctions made from InAs quantum wells, although it was established that no topological phase was achieved [31].

The last approach incorporates elements of the two previous methods and is known as electron teleportation through Majorana bound states [47]. The idea is to form an island of a topological superconductor and take advantage of the charging energy associated with adding electrons to the island. Since the ground states of the superconductor are degenerate with respect to fermion parity, it is possible to tune the charging energy such that a ground state with an even number of electrons has the same energy as one with an odd number. When this happens, electrons can undergo resonant tunneling into one Majorana bound state on the island and appear at the other end with phase coherence. The coherence implies that interfering an electron that passes through the island with one that does not will result in interference effects in the tunneling conductance. The mixing of the two electrons can be done in an Aharonov-Bohm interferometer and the resulting conductance is periodic in units of $h/2e$ flux threaded through the device [171]; the setup is similar to that of a superconducting SQUID. This approach is particularly attractive for experimentalists because it both demonstrates the non-local behavior of Majorana zero modes and serves as a way to measure the parity state of a pair of Majoranas [164].

3.5 Realizing Majorana Zero Modes

While Kitaev showed that unpaired Majorana zero modes can appear from something as simple as a re-pairing of Majorana fermions in a lattice, achieving this effect in reality is another story in entirely. One of the key building blocks of Kitaev's theory is p-wave superconductivity, a property that does not appear readily in nature [100, 142]. Therefore, physicists have turned to engineering the required superconducting properties

using hybrid systems. Here we will review one of the major material thrusts physicists have been pushing to achieve Majorana zero modes before discussing the approach taken in this thesis.

3.5.1 Semiconducting Nano-wires

Semiconducting nano-wires stand at the forefront of achieving Majorana zero modes in 1D systems. The idea behind this approach is to form an effective p-wave pairing utilizing four ingredients: superconductivity, spin-orbit coupling, magnetism, and Fermi level tunability. Superconductivity is a given requirement in any scheme for Majorana fermions, but what is the role of the other three?

Spin-orbit coupling correlates the spin of an electron with its momentum. This effect is the result of the spin-orbit interaction and broken inversion symmetry at interface of materials. For the Rashba variety of spin-orbit coupling, it is often incorporated in a Hamiltonian with the term: $\alpha(\boldsymbol{p} \times \hat{z}) \cdot \boldsymbol{\sigma}$ [104]. Here $\hat{z}$ is the direction perpendicular to the surface of the material, $\boldsymbol{\sigma}$ is the Pauli spin matrix vector, $\boldsymbol{p} = \hbar \boldsymbol{k}$ is the electron momentum, and α is the strength of the coupling. Through this interaction, the energy dispersion of the electrons splits into two spin-dependent bands; one spin species moves to higher k values and the other moves down as shown in Figure 3.3. The spin-direction lies in-plane, perpendicular to the length of the wire. If we introduce a magnetic field into the Hamiltonian via $\mu B \sigma_z$ along the $\hat{z}$ direction, this results in the spin-orbit bands anti-crossing to create a gap at $k = 0$ [88]. Consequently, we enter a "spin-less" regime. Now, if we move the Fermi level into the gap so that we only have one pair of Fermi points, we have

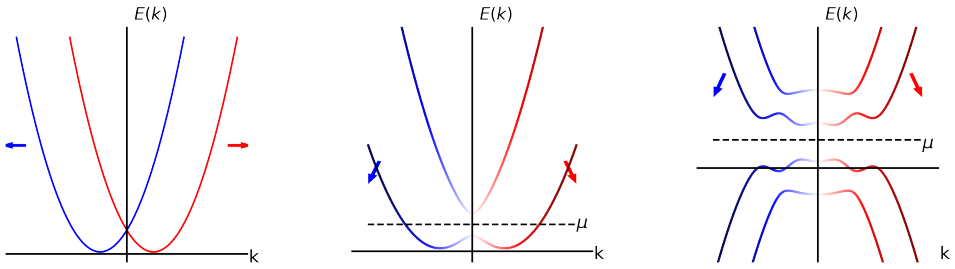

(a) Spin-orbit split bands **(b)** With magnetic field **(c)** With superconductivity

Figure 3.3: (a) Spin-orbit coupling splits the bands based on electron spin. Here the spins are aligned perpendicular to the wire length but in-plane. (b) Adding a magnetic field perpendicular to the spin-orbit field introduces a gap at $k = 0$ and aligns the spins partially allowing for a "spin-less" regime. The Fermi level is indicated by μ which is tuned to lie within the Zeeman gap ensuring so that only one band is occupied. (c) Superconductivity opens a second gap at higher k thus fully gapping the spectrum about the Fermi level. Spin-orbit coupling keeps some level of anti-alignment in the spins allowing s-wave pairing to still occur. Increasing the magnetic field will cause the gap at $k = 0$ to close signaling a transition.

the possibility of creating spin-less superconductivity once we introduce the pairing Δ.

Why is "spin-less" important? Recall that in Kitaev's nano-wire [71], spin was not considered. Incorporating spin can actually nullify topological superconductivity by introducing a Kramer's degeneracy [6]: the spin adds an additional degree of freedom, allowing for the possibility that two Majorana fermions can appear at each end of the nano-wire. This is problematic because the two Majoranas at each end can combine to form a regular Dirac fermion thus destroying the entire effort behind Kitaev's original proposal. Luckily, the magnetic field breaks time-reversal symmetry and removes the Kramer's degeneracy by

polarizing the spins. It does not polarize it completely, however. Spin-orbit coupling still anti-aligns the two spin-bands to some extent based on momentum. This is crucial because many proposals involving semiconducting nano-wires utilize s-wave superconductors which can only form singlet Cooper pairs [122, 99]. The anti-alignment ensures superconducting pairing can still happen in this system.

Continuing the setup, we now tune the Fermi level into the gap so that only one pair of Fermi points exist; in other words, we only occupy one band. This is a requirement for achieving a topological phase transition because when the superconducting gap is the lowest energy scale in the system, the topological invariant 3.15 reduces to [71]:

$$Z(H) = (-1)^p \tag{3.17}$$

Here p is the number of pairs of Fermi points. One may think of this as though each occupied band provides a pair of Majorana zero mode so occupying an odd number of bands will ensure one pair of Majoranas remains leftover. Finally, we introduce superconductivity Δ, and the final payoff for incorporating all four effects is that the occupied band now experiences an effective p-wave pairing once the topological criterion is achieved: $B > \sqrt{\mu^2 + \Delta^2}$ [7]. Thus, we have successfully engineered a 1D p-wave superconductor with Majorana zero modes at its edges.

Some of the earliest successes in identifying signatures of Majorana zero modes come from this approach. This is due to the fact that high-quality InAs or InSb nano-wires can be reliably grown and form clean, epitaxial interfaces with superconducting aluminum [80, 98]. In addition, these nano-wires possess large g-factors that allow the system to achieve

greater Zeeman gaps needed for Fermi level tuning without destruction of superconductivity from magnetic fields. In recent times, it has also been verified that these wires can even grow into each other, allowing the formation of complex networks required for quantum braiding schemes [121, 52].

First evidences of Majorana zero modes based on this material system came around 2012 [42, 32, 113]. Various groups reported observations of zero-bias peaks in the dI/dV spectrum of nano-wires with proximity induced superconductivity. An example of such a device from work done in 2016 is shown in Figure 3.4. These peaks only exist at finite magnetic fields, only for fields perpendicular to the spin-orbit direction, and survive under a range of chemical potentials, all in agreement with qualitative, theoretical predictions. However, the peaks amplitudes were not quantized at $2e^2/h$ and some results could be explained in terms of more trivial effects like Kondo resonance. Studies were also performed using InSb quantum wells patterned into nano-wires for SQUID devices [135]. As the magnetic field was tuned to induce a topological transition, the first (odd) Shapiro step disappeared as an indication of the fractional Josephson effect. Similar work has been done in InAs wires in which a sensitive SQUID detector was used to measure a change in the frequency of the radiation outputted from the Josephson junction as a sign of the 4π effect [84].

However, this approach has experienced a few setbacks. In particular, tunneling spectroscopy was relied on as the go-to method for Majorana detection. This approach has since been demonstrated both theoretically and experimentally inadequate due to the fact that sub-gap Andreev bound states can appear very close to zero bias giving false signatures

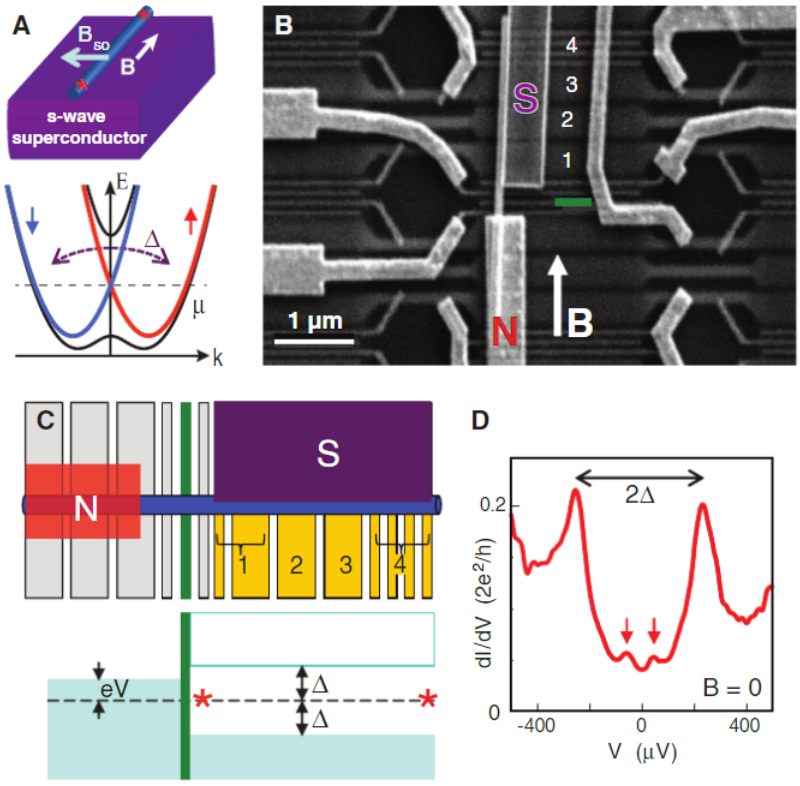

Figure 3.4: (A) Schematic of the InSb nanowire proximitized by a superconductor with the associated spin-orbit split bands. (B) SEM image of the nanowire device. (C) Schematic of the nanowire setup. S corresponds to the parent superconductor and N is the normal metal used for the tunneling lead. The green line is the electrostatic gate used to tune a section of the nanowire to form a tunnel barrier. Only one Majorana mode is probed in this setup. (D) The differential conductance at 65mK under zero magnetic field. In addition to the two coherence peaks, two smaller peaks are seen that correspond to Andreev bound states. From reference [113]/ Reprinted with permission from AAAS.

of Majoranas [94, 95, 111]. Moreover, the conductance of these states can also take on values equal to $2e^2/h$ which further complicates interpretation of the data. As a result, previous work done showing the fusion of two Andreev bound states to form a Majorana bound state as well as the demonstration of $2e^2/h$ zero bias conductance has been called into question [185, 45]. Moreover, many experiments only examined tunneling into one end of the wire which cannot confirm the non-locality of Majoranas, i.e. there should be *two* zero bias peaks at either ends of the wire in the topological phase. Recent experimental evidence has demonstrated both of these shortcomings in InSb wires [181]. Yu et. al. show the presence of nearly quantized conductance peaks at zero bias on one end of a quantum wire in the supposed topological regime but do not observe any peaks at the other end of the wire. It is clear that more decisive detections schemes must be employed to accurately confirm the existence of Majorana zero modes.

A final comment of this approach is the issue of scalability. While it has been demonstrated that these wires can be grown reliably enough for basic research, it is still an open question whether it is possible to achieve a level of control required for large scale devices. The epitaxy procedures for existing nano-wire networks can be quite complicated [52], and this is not accounting for the additional fabrication processes required for adding electrostatic gates and leads. Therefore, moving forward with this methodology will require further mastery over the material growth aspect.

3.5.2 Majorana Zero Modes Have Struck Gold

If semiconductors can be leveraged for their spin-orbit effects to achieve Majorana zero modes, what about metals? It has been demonstrated previously that the surface

bands in an Au (111) film experience large spin-orbit coupling of $110meV$ [85]. This is attractive because the size of the topological gap at finite k generally increases with large spin-orbit strengths [5]. Therefore, combining gold films with superconducting and magnetic materials should yield similar results to that of semiconducting nano-wires. This is the material approach taken within this thesis and will be the point of emphasis for the tunneling studies performed.

Both theory and experiment have already demonstrated promise with this approach. Theory shows that Majorana zero modes can localize and persist in such a film as long as its width is narrowed down to approximately the superconducting coherence length [129]; this helps to reduce the strictness of the 1D-ness requirement. In addition, it has also been calculated that electrostatic gates are capable of tuning the Fermi level of the surface bands despite screening effects of the metallic film [130].

Experimental progress has achieved a number of milestones with this material system so far [169, 105]. First, deposition of an EuS dielectric results in a large shift of the surface band bottoms towards the Fermi level. This is important because the Zeeman gap that opens in the Rashba bands occurs near the band bottom so we need to bring the band bottoms closer to the Fermi energy so that electrostatic gates can actually tune the chemical potential without suffering from screen effects. In addition, EuS is ferromagnetic so its exchange field can enhance the Zeeman gap. Second, superconductivity has been demonstrated to exist in the surface bands. This is also important because the surface bands are separated from the bulk bands by an energy gap so it is not immediately obvious that proximity superconductivity can be transferred to the surface states; achieving this

theoretically requires scattering processes to induce pairing in the surface states [130]. Fortunately, tunneling signatures reveal the presence of two superconducting gaps that cannot be accounted for by spin-splitting of the density of states.

The culmination of these two successes has allowed for the observation of zero bias peaks using STM near the edges of EuS islands deposited on Au nano-wires. This is shown in Figure 3.6. The peaks only appear after a certain finite in-plane magnetic field is achieved, and they appear at the same time at opposite ends of the island. This non-locality helps to rule out possible Andreev bound state signatures as there is no a priori reason why two such peaks will appear at the same time, unless they are Majoranas. In addition, the appearance of these two zero bias peaks is well corroborated with numerical simulations. The peaks in question were observed along the edge of an island that was aligned right up against the edge of the Au nano-wire. Simulations show that this scenario results in a concentration of the Majorana wavefunction at the two observed points accounting for the zero bias peaks; EuS islands located away from the Au wire edge would show a smeared out wavefunction instead.

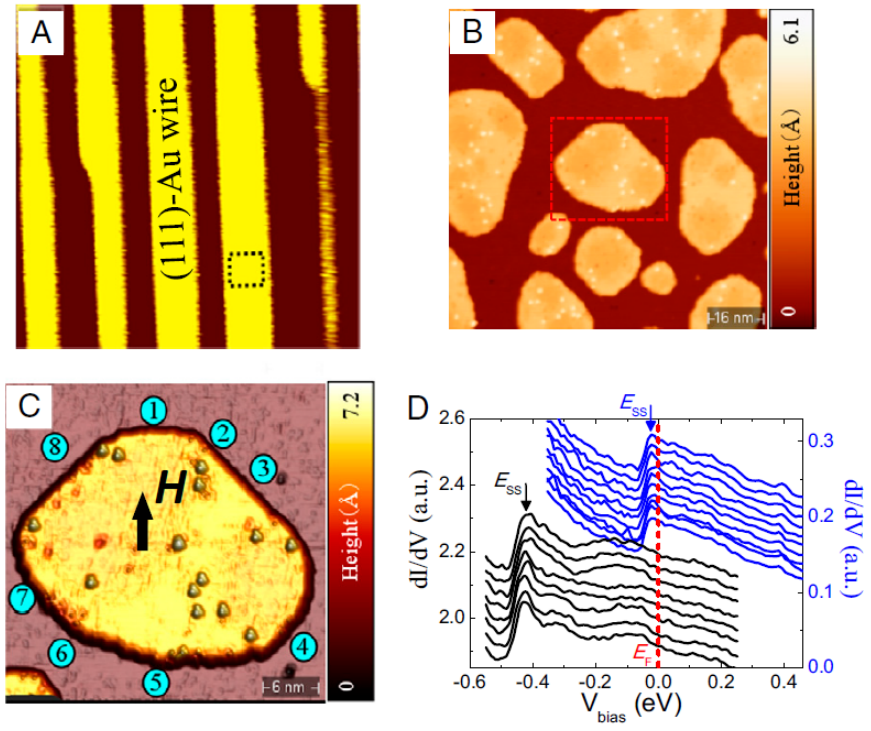

Figure 3.5: Fabricated gold nano-wires with EuS islands deposited on the surface. The plot shows a peak in the dI/dV scan at high bias voltages corresponding to the Au (111) surface band bottom. The peak position shifts dramatically closer to the Fermi energy (blue curve) once EuS covers the surface. This is important for tunability of the Fermi level. From reference [105]/ Reprinted with permission from National Academy of Sciences.

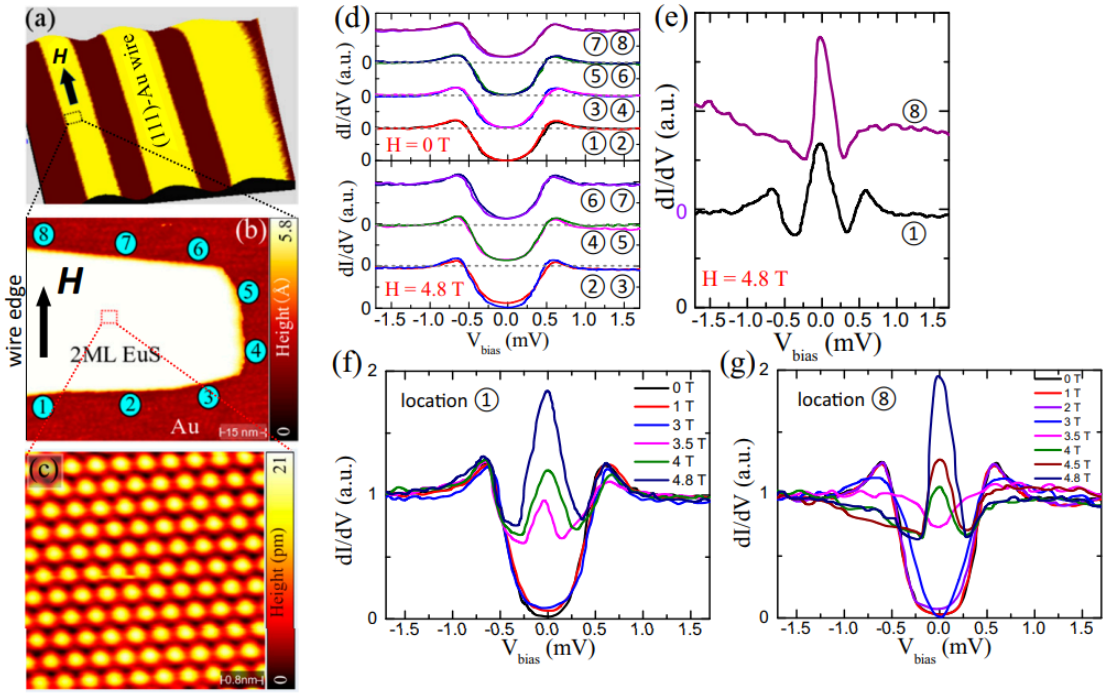

Figure 3.6: EuS islands on top an epitaxial Au nano-wire. An STM is used to scan along the edges of the island. The scans show a hard superconducting gap along the edges of the island except for the edge that lines up with the edge of the Au nano-wire. At points 1 and 8, a zero bias peak emerges as the magnetic field is tuned in accordance with theory simulations. From reference [105]/ Reprinted with permission from National Academy of Sciences.

In wake of these achievements, further refinement of the Au (111) system has been proposed and summarized in reference [177]. Recall that prior work using gold nano-wires suffered from two main limitations: high Fermi energy relative to the Rashba band bottoms, which results in the occupation of multiple subbands, and a small Landé g-factor of 2, which required high magnetic fields to close the trivial gap and open the topological gap [169, 105]. This is why deposition of EuS on top of the Au surface and the use of an interface exchange field was a necessary step to help resolve both of these issues. As it turns out, one can pursue the use of EuS even further and flip the prior work on its head: instead of EuS films on top of gold wires, it more advantageous to deposit EuS wires on top of a gold film.

This new approach, which shares similarities to the ideas in reference [123], is shown in Figure 3.7 [177]. An EuS strip is deposited on top of a superconducting gold film. The region under the EuS experiences a large shift in the chemical potential of the surface bands relative to the uncovered gold. Through a combination of normal and Andreev reflection with the surrounding bare regions, a bound state in the region under the strip can be created. Next, adding sufficient Zeeman energy to exceed the superconducting gap Δ results in a gapless band structure (shown in 3.7 (b: b)) that is capable of supporting zero energy states for Majorana zero modes. The shifting of the chemical potential is a key ingredient in this approach as it is responsible for ensuring that the gap closure points do not appear too close to each other which limits the size of the topological region in the phase diagram [177]. Therefore, deposition of EuS, or similar material, to modulate the chemical potential is necessary.

It should be mentioned that one key advantage of this approach in comparison to semiconducting nano-wires is scalability. Single element metal films are regularly grown in labs and are simpler to achieve when put against materials that require the proper reactions between constituents; for instance, the growth of high mobility HgTe quantum wells required for observation of the quantum spin Hall effect took some time to achieve [81]. Moreover, existing fabrication tools, such as ion millers, are readily available to pattern these films into 1D networks for Majorana braiding, unlike semiconducting quantum wires which require special growth procedures [52].

Of course, this does not mean there are no challenges ahead. In particular, deposition of EuS into 1D wire networks remains to be seen. Moreover, theoretical work indicates that the size of the topological regime varies periodically with respect to the width of the wire and the chemical potential shift under the wire [177]. This will require fine tuning of material parameters to ensure a robust topological transition. An additional question also arises: are there other materials besides EuS that can fulfill a similar role? A key bottleneck in the engineering of synthetic topological superconductors lies in the proper synthesis of each ingredient material. For the Au (111) system, this material must fulfill two important requirements: Fermi energy tuning and enhanced Zeeman interaction. In a later section of this thesis, we will explore one possible alternative: tellurium.

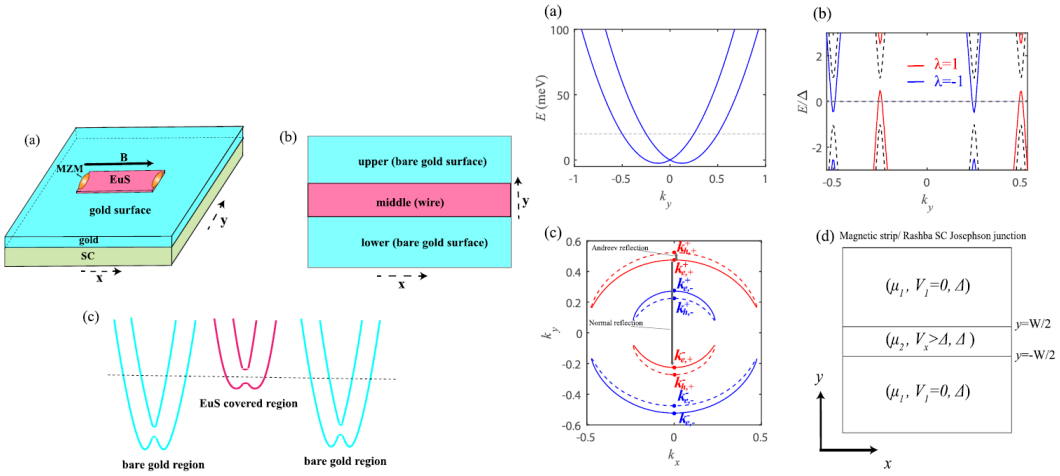

(a) EuS Wire Geometry **(b)** Band Structure of the EuS wire setup

Figure 3.7: (a: a-b) Schematic of an EuS wire on top of a gold film. (a:c) The EuS dielectric shifts the Rashba bands relative to Fermi energy in comparison to the bare gold regions. (b: a) The Rashba bands of the EuS wire in the normal state. (b: b) The Bogoliubov-de Gennes spectrum along k_y for a Zeeman field = 0 (black-dotted) and with a Zeeman field (colored). The red and blue colors correspond to states with spin parallel or anti-parallel to the field. When $V_{Zeeman} > \Delta$, the gap closes. (b: c) The E = 0 contour of the energy spectrum. (b: d) The corresponding geometry for the band structure calculations. Reprinted with permission from the American Physical Society, reference [177].

3.6 Quantum Computation Using Majorana Zero Modes

The end goal for all the work being done in Majorana zero mode research is to build a quantum computer. Unlike "conventional" approaches to quantum computing such as transmons or trapped ions [127, 76] which rely on manipulation of multi-level systems, a Majorana based computer revolves around working with a set of degenerate ground states. Specifically, Majorana zero modes, despite being described by a fermion

operator γ, do not obey traditional exchange statistics [134]. Moving Majoranas around each other, otherwise known as "braiding", is a non-Abelian operation. The end result is not the original wavefunction with a ± 1 factor tacked on the front, but an entirely different state. In general, the braiding operator for two Majoranas γ_n, γ_m can be written as [9]:

$$U(\gamma_n, \gamma_m) = exp(\pm\frac{\pi}{4}\gamma_n\gamma_m) = \frac{1}{\sqrt{2}}(1 \pm \gamma_n\gamma_m) \tag{3.18}$$

Consider two pairs of Majorana zero modes γ_1, γ_2 and γ_3, γ_4. Each pair can combine to form a Dirac fermionic mode so that we have four possible logical quantum states $|00\rangle |01\rangle, |10\rangle, |11\rangle$; here $|00\rangle$ means neither pair formed a mode and $|11\rangle$ means both formed a mode. Under exchange of γ_2 from the first pair and γ_3 from the second pair, we can transform the state $|00\rangle$ into: $U(\gamma_2, \gamma_3)|00\rangle = \frac{1}{\sqrt{2}}(|00\rangle - i|11\rangle)$ [9]. This ability to generate new states from exchange operations lies at the heart of Majorana based quantum computers. The added bonus to all of this is that the resulting quantum states are long lived as a result of topological protection.

However, as with any approach, there is no free lunch. One of the key drawbacks to Majorana quantum computing is the need for high fidelity braiding operations. Physically exchanging Majoranas is difficult as it must be done adiabatically to ensure the system does not leave the ground state manifold [36]. Luckily, recent work has shown that physical braiding is not necessary. It turns out that tunneling measurements are capable of measuring the parity of a Majorana island [164]; this is called measurement-based braiding. Such a scheme will significantly simplify the hardware needed for executing quantum logic gates.

Another challenge is the issue of parity. A collection of isolated Majorana qubits have a total fixed fermion parity and exchanges of Majoranas will not change it. This is also the reason why superpositions of states with different fermion parity are not possible and why Majorana qubits require at least *two* pairs of Majoranas. The situation can change, however, if a quasi-particle tunnels onto the island and switches the parity [69]. This event can happen due to environmental perturbations or even within the Majorana island itself as a result of thermal excitations. This process is called quasi-particle poisoning and its frequency of occurrence is a genuine concern in the design of Majorana devices [4].

Chapter 4

Experimental Methods

4.1 Molecular Beam Epitaxy and Thin Film Growth

4.1.1 The Hardware

Molecular beam epitaxy (MBE) is the process of depositing thin films on substrates in ultra high-vacuum using thermally heated material sources [65]. The high vacuum extends the mean free path of any gaseous atom so the evaporated material travels ballistically from the source to the substrate. In addition, atmospheric contamination is reduced to a minimum allowing the growth of very high quality materials such as HgTe quantum wells for quantum spin hall studies [78]. The MBE system used for the work in this thesis is shown below along with a representative diagram of the system. Here we explore the operation and purpose of the different components of the vacuum chamber.

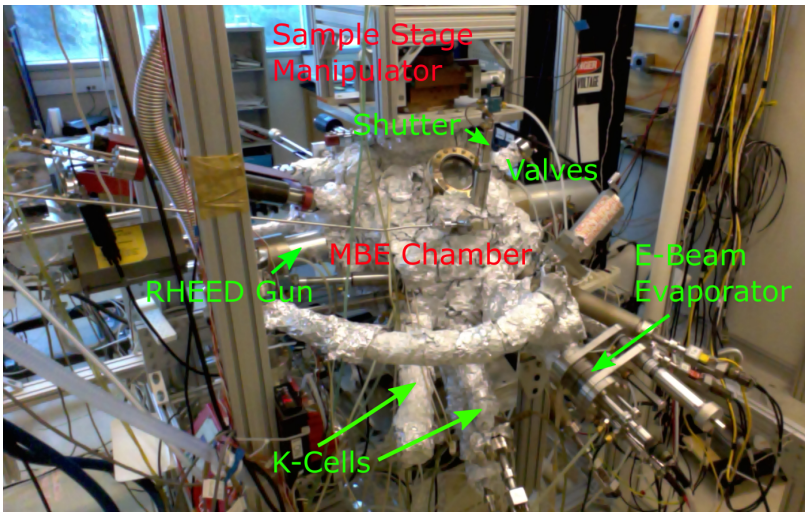

Figure 4.1: Ultra high-vacuum MBE chamber

Pumping System The ultra high-vacuum is held by a combination of pumps: scroll, turbo, and ion. Scroll pumps achieve "rough" vacuum ($10^{-2} - 10^{-3}$ Torr) to prepare the system for the other pumps. The high-vacuum regime ($10^{-6} - 10^{-8}$ Torr) is achieved via turbo pumps; these pumps are similar to that of a jet turbine with multiple sets of blades spinning at high speeds to extract air from the system. The blades of a turbo pump cannot handle high airflow loads and require a backing pumping (such as a scroll pump) to remove air expelled by the turbo. The final pump that is used to bring the system into the ultra high-vacuum regime ($< 10^{-8}$ Torr) is the ion pump. This pump works similar to that of a large capacitor: gas molecules passing through are ionized and then accelerated towards a reactive, solid electrode to bond with the electrode material. Like the turbo pump, ion pumps require another backing pump to pull the system into the high-vacuum regime before operation. The various sections of the vacuum system are connected by conflat flanges and below tubes with gate valves used to isolate the different sections.

Knudsen Cells Name after Martin Knudsen, the Knudsen cell (K-Cell for short) is an thermal evaporator for low-vapor pressure materials. Material is placed into a crucible and then heated by running current through nearby filaments. Control of the evaporation rate of the material is accomplished by controlling the heating power. K-cells are best suited for low temperature evaporation materials such as tellurium, selenium, bismuth, etc. It can also be used to evaporate higher temperature metals like gold or aluminum but care has to be taken to ensure proper shielding of the filaments otherwise excess heating of surrounding vacuum parts can occur. Below shows the inner structure of a homemade K-cell. Supporting metal pieces are made either from molybdenum or tantalum due to their high thermal integrity. The heater wiring is tantalum wire wound through PBN (poly-boron nitride) rings. A small thermo-couple (C or K type) is mounted near the crucible to measure the temperature. Alumina ceramic pieces are used to electrically isolate the wiring from the rest of the K-cell parts.

E-Beam Evaporator Refractory metals like tungsten or niobium require much higher temperatures to evaporate than what is available from K-cells. To accomplish this, e-beam evaporation is used. The process involves heating a thin filament to achieve thermionic emission. The emitted electrons are then accelerated by a potential difference and redirected so they bombard the evaporating material. This form of heating can achieve temperatures above 2500°C. There are two general types of e-beam evaporators: crucible and rod. Crucible-based evaporators hide the emitting filament away from the evaporation source. The emitted electrons are then redirected using a magnetic field through a 270° arc to bom-

bard the material. This type of evaporation system is commonly found in cleanrooms. The e-beam evaporator used in this thesis is of the latter rod variety. Here a rod of the material to be evaporated is biased at high positive voltages relative to a nearby filament. A picture of the evaporator is shown below. The advantage of this setup is that the electrons are focused to a much smaller area on the rod allowing easier evaporation of high melting point materials. The disadvantage is that the filament is exposed to the resulting evaporation and can weaken over time from ion bombardment.

4.1.2 Thin Film Growth

The process of depositing thin films onto a substrate is the starting point of much of modern condensed matter nanoscience. This thesis primarily makes use of only thermal or e-beam evaporation, but there are other choices as well such as sputtering, pulse-laser, chemical vapor, atomic-layer, etc. Despite the differences between each methodology, they all share three common characteristics when it comes to thin film growth: choice of substrate, temperature profile, and level of material flux. Proper tuning of these three parameters is crucial for high-quality growth of thin films.

Substrate Choice

Substrate choice is the starting point of any growth process as choosing the right substrate can easily make or break a growth. The first point of consideration in picking a substrate is lattice mismatch, i.e. the difference in lattice parameters between the substrate and the desired film. Atoms like to line up with existing atoms and so picking a substrate

with similar lattice parameters on the surface to that of the film greatly aids in achieving the right growth. Mismatching the lattice introduces strain into the film and results in defects as the film tries to relax itself [50, 165]. Moreover, the defects can act as scattering centers that impact the physical and electrical properties of the film [3]. But, this negative view of lattice mismatch is only one side of the coin. We can turn the problem on its head and instead take advantage of strain to engineer new properties into the film [27, 93]. This will be the subject of Chapter 6.

However, it is often not possible to pick substrates with matching parameters either due to lack of options, lack of desired properties of the substrate, or deterioration of the substrate in response to the growth conditions. Luckily, lattice mismatch is only one part of the story. In recent times, the rise of van der Waals materials has demonstrated the growth of films on substrates with large lattice mismatches [183, 55, 114]. Therefore, other substrate factors such as wettability, presence of dangling bonds, and step edges are equally important players in the growth process. For example, in the case of copper epitaxy, control of the surface termination of sapphire (Al_2O_3) changes the surface morphology and substrate-epilayer bonding of the deposited films [120]. Similarly, the growth of high quality $NbSe_2$ on MoS_2 was achieved due to the inert surface of the substrate despite the large mismatch [77]. In general, developing proper passivation techniques can reduce reactivity of the substrate surface which allow for increased wettability and a reduction in the number of nucleation sites [41, 159].

A final comment on this section is the influence of substrate cleaning. Obviously contaminants on the substrate surface will hinder proper growth of the film. How to remove

said contaminants is easier said than done, however. We will go over the cleaning methods used in the growth of Nb-Au and $NbSe_2$ films in the later chapters.

Temperature Profile

The second knob to tune is the temperature profile of the growth process. Atoms impinging on the surface of the substrate will have a limited lifetime to move around on the surface before they settle down or bond with another atom [183]. The temperature of the substrate controls the mobility and lifetime of these "adatoms" with higher temperatures leading to higher mobilities. For epitaxial layer growth, it is important that mobilities be sufficiently high so that adsorbed adatoms can travel far enough to find the edge of the growing film; if it does not find the edge, then the adatom will fixate at some point on the substrate and form a new nucleation site. How high is sufficient depends on the film grown and the substrate. In the growth of epitaxial Te capping layers on Bi_2Te_3, the sample was cooled to 150K for growth [125] whereas epitaxial niobium on sapphire required temperatures from 750°C to 900°C [172]. Figuring out the correct temperature is very much a trial and error game as every growth system is different, and there is often difficulty in measuring the true temperature of the substrate.

Material Flux

Adjusting the rate of material flux impinging the substrate also has significant effects on the growth of thin films, particularly for heteroepitaxial films. First off, changing the ratios of constituent elements changes the stoichiometry of the compounds produced. For example, the MBE growth of $MnBi_2Te_3$ versus $MnBi_4Te_7$ was found to be governed

by the amount of Mn flux relative to Bi and Te [83]. Secondly, the reactivities of the constituent elements affects which materials need to be supplied in excess. The MBE growth of transition metal dichalcogenides is often characterized by the oversupply of chalcogen flux due to the low reactivity of the transition metals [184, 114]. Under supply can lead to vacancies and dangling bonds within the films. Moreover, different elements have distinct evaporation temperatures meaning the sticking ratio of adatoms will differ by element [183]. Fine tuning the correct flux ratio of the sources also requires trial and error for each type of growth and growth system.

Reflection High Energy Electron Diffraction

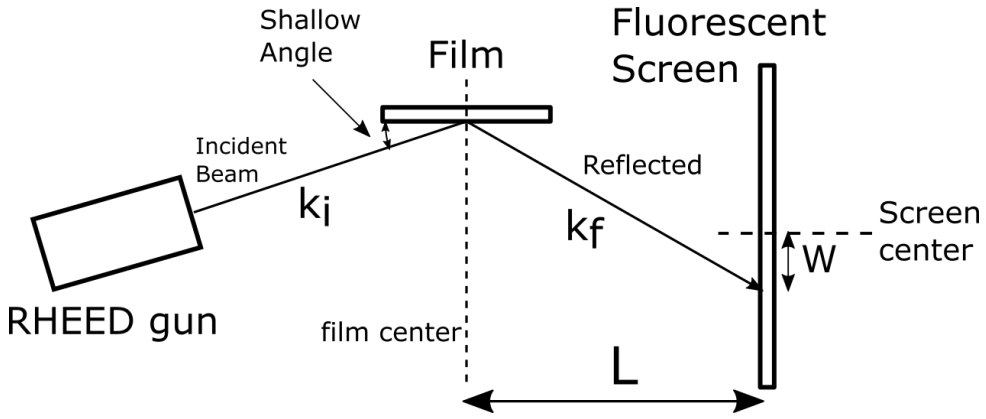

(a) RHEED Diagram

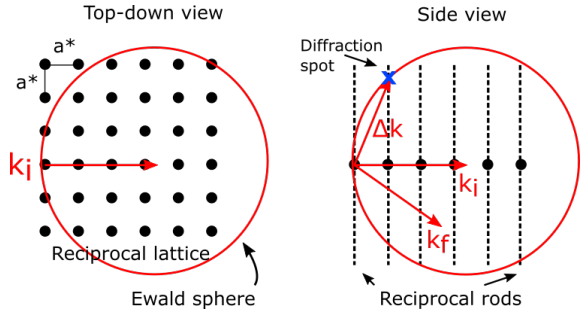

(b) Reciprocal lattice and Ewald's sphere

Figure 4.4: (a) Schematic of the RHEED setup for imaging the film surface during growth. The distance between the point of incidence to the screen is L. The diffraction pattern forms streaks on the screen with a spacing of w. (b) Ewald's sphere provides a useful tool to understand the diffraction condition 4.1. Since the film is treated as a 2D surface, the reciprocal lattice in 3D is a grid of rods emanating from the surface. Intersection of the rods with Ewald's sphere (radius = k_i) indicates a diffraction peak.

Adjusting the knobs on the three parameters discussed tunes what kind of growth will occur. There are three common models describing the different growth types: Frank-van der Merwe (layer by layer), Volmer-Weber (island), or Stranski-Krastanov (island + layer) [62, 165, 183]. A rule of thumb for determining the type of growth mode is based on the surface energy of the film, the substrate, and the interface between the two. For instance, if the film has a higher surface energy, island growth occurs in an attempt to minimize the film surface area; if the substrate dominates, layer growth occurs to wet the substrate as much as possible. Other principles discussed previously, such as lattice mismatch and temperature, also affect what growth mode takes place as well as the kinetics of the crystal formation.

However, from an experimentalist perspective, these principles are just theoretical guides, and in-situ empirical evidence of the growth process still serves as the best judge for what kind of growth type has actually occurred. In this thesis, the tool used to make this judgment call is reflection high energy electron diffraction (RHEED) [101]. The basic principle of RHEED is to shoot a small, highly energetic beam of electrons (15keV) at the substrate at a shallow, glancing angle. The reflected electrons are imaged by a fluorescent screen to form a diffraction pattern from which one can learn information about the film surface. A diagram of the setup is shown in Figure 4.4.

The location of the diffraction streaks is determined by the von Laue condition [13]:

$$\Delta \boldsymbol{k} \cdot \boldsymbol{R} = 2\pi m \tag{4.1}$$

Here $\Delta \boldsymbol{k}$ is the change in wavevector of the scattered electron and $\boldsymbol{R}$ is lattice vector of the film's surface. This condition basically states that the change in wavevector $\boldsymbol{k}$ must be an element of the reciprocal lattice of the film surface. Furthermore, since we are only working with the surface, the corresponding reciprocal lattice in 3D consists of an array of rods shown in Figure 4.4. Ewald's sphere [13] helps to determine the location of the diffraction maxima. This sphere has a radius of $\boldsymbol{k}_i$ with the origin of the reciprocal lattice sitting at the edge of the sphere. Intersection of the reciprocal rods with the sphere indicate a diffraction peak. In reality the intersection of the rods and the sphere will not occur as points but more commonly as streaks. This is due to the fact that realistic RHEED beams have a finite dispersion in their energy (not perfectly monochromatic), and the reciprocal lattice points of a film are not perfectly singular so the reciprocal rods have a finite width.

The different growth modes can be determined by the shape of the RHEED streaks. Layer-by-layer growth corresponds to narrow lines, island growth corresponds to dots, and island+layer has characteristics of the two previous cases. These qualitative features allow an experimentalist to tailor the growth recipe accordingly to achieve the desire film. In this thesis, layer growth is the goal so the sharper and more narrow the RHEED streaks are, the better. Examples of each growth type and corresponding RHEED pattern is shown below.

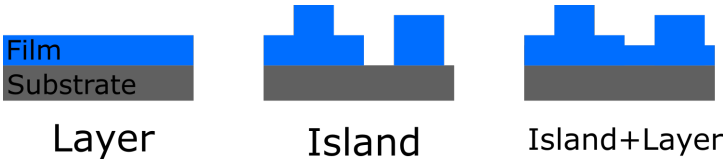

(a) Three types of growth modes.

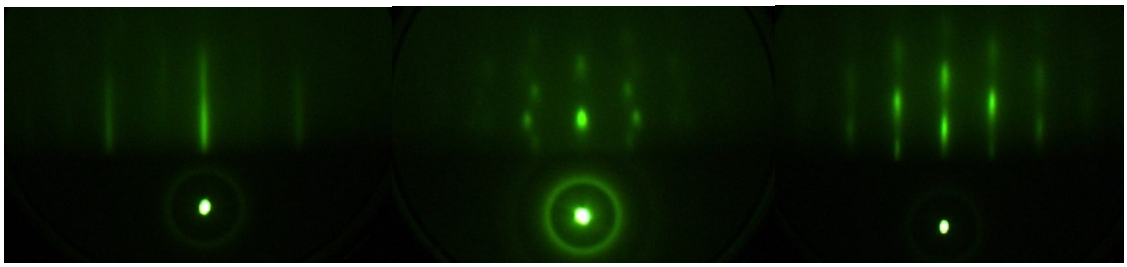

(b) Layer by Layer **(c)** Island **(d)** Island + Layer

Figure 4.5: Corresponding RHEED patterns for the three types of growth modes commonly found in thin films.

Quantitative information is also present within the RHEED pattern. The electron wavevectors $\boldsymbol{k}_i, \boldsymbol{k}_f, \Delta\boldsymbol{k} = \boldsymbol{k}_f - \boldsymbol{k}_i$ form a similar triangle with that of the diffraction spacing w and the distance between point of incidence to the fluorescent screen L [101]. This allows one to calculate the reciprocal lattice constant a^* of the film as:

$$a^* = \frac{2\pi w}{\lambda L} \tag{4.2}$$

Here λ is the wavelength of the RHEED beam. In practice, knowing the wavelength is not necessary, and a^* is calculated by using a reference sample with a known reciprocal lattice constant a_r^* and streak spacing w_r while holding the RHEED wavelength λ and distance L constant. Now we can form a ratio from equation 4.2 giving $a^* = a_r^*(w_r/w)$.

One can also convert this reciprocal distance into the real space lattice constant to confirm the film possesses the correct crystal structure.

A final word about RHEED is that it also allows one to check the in-plane rotational symmetry of the film. In general, 2D crystals only have 2, 3, 4, or 6 fold symmetry with regards to rotation [13]. Therefore, rotating the sample along its azimuthal axis should result in the RHEED pattern repeating every so often in accordance with the crystal symmetry. This simple check is useful to confirm that the correct crystal is growing.

4.2 He3 Cryostat and Measurement

4.2.1 Cryostat Hardware and Software

The cryostat used in this thesis is a 300mK He3 Heliox system from Oxford Instruments. A diagram of the fridge is shown below.

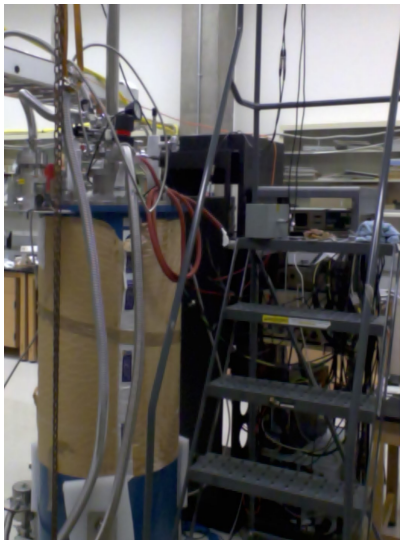

Figure 4.6: Oxford He3 Heliox Cryostat

The cryostat is split into a series of concentric cylinders. From outer to inner, the sections roughly are: outer vacuum chamber, liquid nitrogen jacket, liquid He bath, inner vacuum chamber, and sample space. Samples are inserted into the cryostat top-down via a long probe. Temperature control is achieved by balancing heating from coiled-wire heaters and the cooling power of the liquid He bath. An 8 Tesla superconducting magnet is also available for operation. More about the specific operating procedures of the fridge can be found in the appendix.

The unique aspect of this fridge is its ability to cool down to a base temperature of 240mK using He3, an isotope of Helium. This occurs by condensing He3 into a liquid and then pumping on He3 vapor to reduce its pressure and consequently its temperature. Currently, the fridge is capable of sustaining this base temperature for up to 30 hours. However, hold times can shorten if care is not taken to properly insulate the sample chamber. Convective heat transfer must be kept down to a minimum by ensuring the vacuum chambers are adequately evacuated; $< 10^{-3}$ Torr for the outer vacuum chamber and $< 5 \times 10^{-6}$ Torr for the inner vacuum chamber. In addition, the radiation baffles on the sample probe must fall into place to block thermal radiation coming from the warmer portions of the sample chamber. For instance if no baffles were inserted, the Stefan-Boltzmann law indicates that the room temperature section of the sample space can emit up to $\approx 46 mW/cm^2$ down to the base area. With a baffle in place that is held at 77K, an emittance of only $\approx 0.2 mW/cm^2$ is possible, which is two orders of magnitude smaller. The use of a liquid nitrogen jacket also aids in this purpose. Finally, electrical wiring with low thermal conductivity must be used in the sample chamber to prevent further heat transfer.

Below shows a diagram of the sample probe used to mount the devices for measurement. All wiring on the probe that runs from the vacuum feed-through down to the base uses Constantan wire due to its low thermal conductivity and low variation in resistivity with respect to temperature. Custom PCB low-pass filters are mounted along the length of the probe using copper brackets. Custom PCB boards are also used as the holder for the samples to be measured. Interconnects between different sections of the probe use standard PCB headers purchased from Digikey.

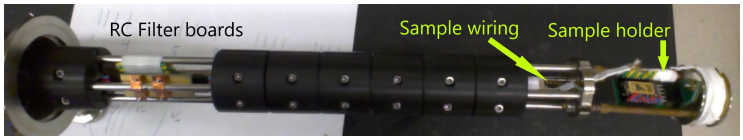

(a) Heliox Probe

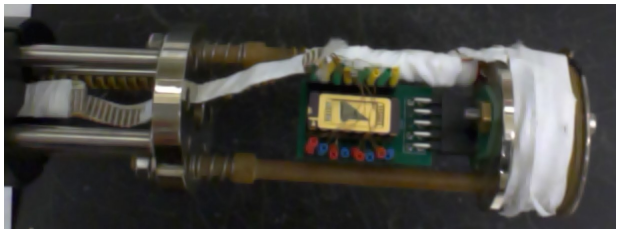

(b) Close-up of sample space

Figure 4.7: Heliox Sample Probe. All wiring is Constatan wire. The sample mount is custom designed PCB boards using commercially available connectors. The RC filter boards are mounted further away from the sample to reduce the thermal load so that the system can achieve its base temperature.

All control of the fridge is done using a suite of homemade LabView programs. This includes temperature control and magnet control. Below shows the main LabView program used to operate the cryostat. Temperature readings, cryogen levels, and system

status is all displayed. Information about the He level is also uploaded to a Google drive on the cloud for record keeping. The software is setup as a state machine that communicates using a message-based queue. Auxiliary programs can write commands to the queue that the program will process. This provides a simple interface for controlling the fridge.

4.2.2 Measurement Electronics

The measurements in this thesis are mainly focused on transport. Here we will discuss the process for a differential conductance measurement. A schematic of this setup is shown below. Differential conductance dI/dV is simply the derivative of the I(V) curve. One could simply measure this curve then numerically differentiate the data to obtain the dI/dV, but the sensitivity is limited by the resolution of the voltage data points and the noise in the measured current. A more commonly used methodology is to DC bias a small AC voltage signal to use as the probe for the differential conductance. The validity of this approach is based on the small signal expansion of the I(V) curve.

$$I(V + \delta V) = I(V) + \frac{dI}{dV}\delta V + \mathcal{O}(\delta V^2) \tag{4.3}$$

Here δV represents the small AC signal. We see that the first order component is now proportional to dI/dV. Feeding this signal into a lock-in amplifier locked on to the AC probe frequency allows for accurate extraction of the differential conductance. This ideas serves as the basis for the above setup. A lock-in amplifier provides an AC signal that is DC biased using a transformer. The output is put through a double RC low pass filter with

a roll-off of $\approx$ 1KHz to reduce extraneous noise. The signal is then scaled down using a resistive voltage divider and sent to the sample probe. Additional passive filtering is done at the input to the sample probe using π-filters before passing through another RC filter at low temperature. Once the probing signal passes through the sample, the current is then filtered to remove the DC component. The AC component is sent to a sensitive current-to-voltage amplifier who output is in turn fed into the input of the lock-in amplifier. The measurement process consists of successive adjusting the DC bias applied and measuring the differential conductance signal from the lock-in.

(a) Full K-Cell **(b)** Heating Cage

Figure 4.2: (a) One of the homemade K-cells used in the MBE system. The K-cell is constructed from a CF flange feed-through that supports a heating cage. The cage is wrapped in tantalum foil to contain the thermal heat from the cage. Ceramic tubes are used to insulate the wires from surrounding support rods. (b) The heating cage with the foil removed. The wiring is tantalum. The cage is kept in shape by PBN rings.

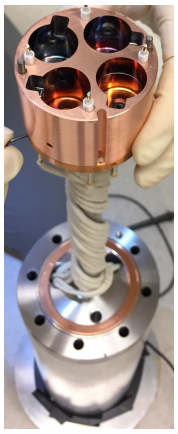

Figure 4.3: E-Beam Evaporator. The copper head contains 4 pockets to allow loading of 4 different evaporation sources. Temperatures of the head are kept low by active water cooling.

Figure 4.8: Cryostat LabView control program.

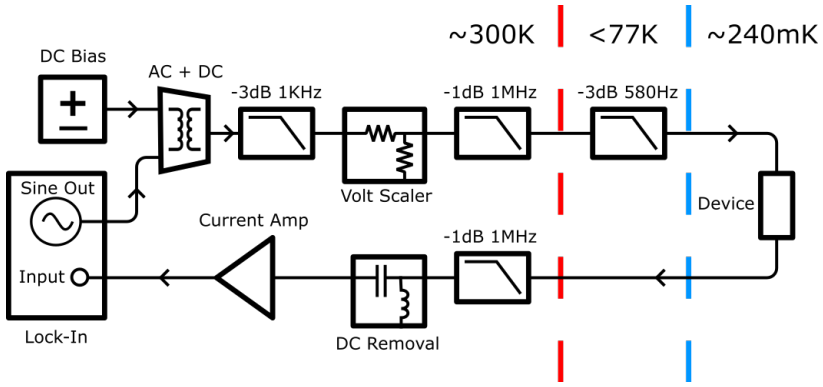

Figure 4.9: Schematic of dI/dV measurement

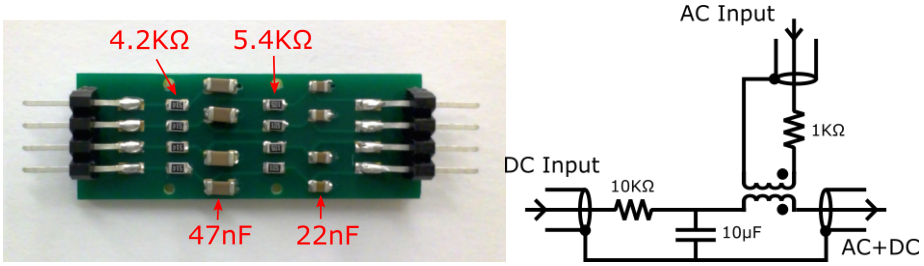

(a) Homemade double RC filter PCB **(b)** AC + DC circuit schematic

Figure 4.10: (a) The board material is standard FR4 with an immersion gold finish for the soldering pads. The backside is a large copper pour, also with immersion gold finish, that serves as the ground plane. The surface mounted components are metal film resistors and C0G dielectric capacitors. These specific types of components do not suffer from significant variations in electrical values with respect to temperature making them ideal for cryogenic circuits. (c) Homemade audio voltage transformer circuit to DC bias the AC signal. An AC signal is fed into the primary winding to generate a small AC signal on the secondary. The series resistor in the secondary is used to prevent saturation of the transformer's magnetic core. The capacitor provides a low impedance shunt for the AC signal to return back to the transformer.

Chapter 5

Topological Superconductivity in Au Thin Films

As it was stated earlier in Chapter 2, evidence of Majorana zero modes was observed in Au (111) films proximitized by superconducting vanadium and EuS islands [169, 105]. In this thesis we wish to expand upon this approach by exchanging the vanadium for niobium. The rationale is to enhance the size of the topological gap by increasing the size of the superconducting gap in the surface states. Bulk vanadium superconducts at around 5K whereas niobium does so at 9K. Since both materials are conventional s-wave superconductors, BCS theory predicts that the magnitude of the pairing gap at $T \approx 0$ proportional to the transition temperature: $|\Delta| = 1.76 k_B T_c$ [158]. Therefore, simply swapping to niobium can almost double the gap.

This chapter presents the successful growth of Au (111) films on top of niobium with a sapphire substrate; MBE and e-beam evaporation are the deposition methods used.

The films are characterized by a combination of RHEED, AFM, and resistivity measurements. Additional conductance measurements are studied using point contact spectroscopy in the tunneling limit. The results indicate that superconductivity is induced in the surface bands and that a tellurium capping layer enhances the Landé g-factor of the Au film. We discuss possible origins for this effect and next steps.

5.1 Growth of Nb-Au Thin Films

Niobium in its bulk form possesses a BCC (body centered cubic) structure with a cubic lattice constant of 3.3Å. However, the (110) crystal plane has a 2D hexagonal structure with lattice constant of 2.86Å. It has been found that deposition on A-plane sapphire results in a Nb film that is naturally oriented in the (110) direction [167]. Furthermore, the Au (111) crystal plane is also hexagonal with a closely matching lattice constant of 2.88Å. Such minimal mismatch suggests that growth of Au (111) on niobium should be possible.

We purchase the A-plane sapphire from MTI Corporation and clean the substrates using a specialized detergent solution. After loading the sample into the MBE chamber, the Nb-Au film is grown according to the following recipe. Representative RHEED images of the two films are also shown below.

1. Outgas substrate for 30 minutes at 500°C.

2. Cool down to 100°C.

3. Deposit 1nm of Nb using the e-beam evaporator. Substrate temperature is held at 100°C.

4. Anneal "seed" layer until RHEED pattern appears, approx. 400-450°C.

5. Continue Nb deposition at current substrate temperature. Substrate heating is adjusted as needed depending on the evolution of the RHEED pattern.

6. Once desired thickness is achieved, cool down sample to room temperature.

7. Deposit desired thickness of Au using a K-cell. Substrate is held at room temperature.

8. Anneal film ≈ 100°C to improve Au RHEED.

9. Let sample cool to room temperature before removing from chamber.

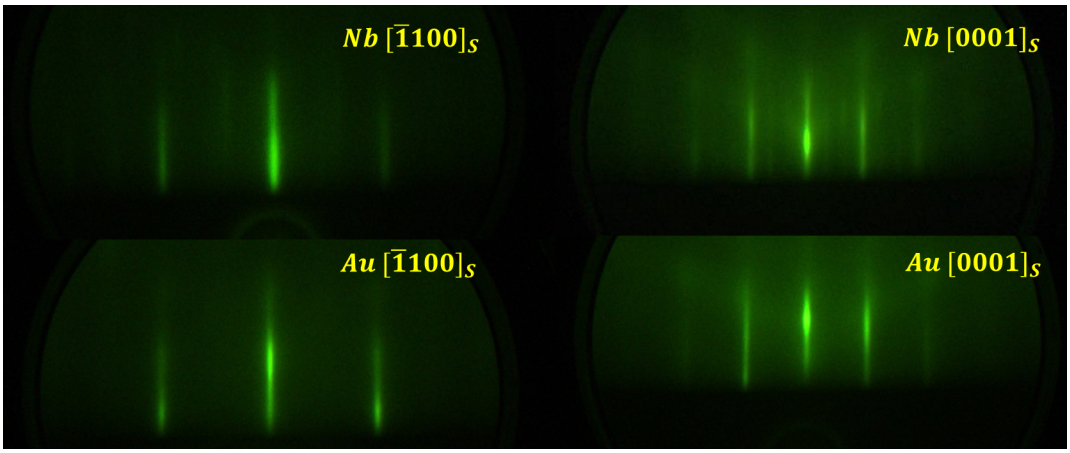

Figure 5.1: Representative RHEED patterns for the Nb and Au layers grown. The directions shown are relative to the sapphire crystal plane.

Figure 5.1 shows some example RHEED images of the Nb and Au films. The images are taken along two distinct symmetry directions that are 30° apart from each other rotated along the azimuthal axis; the directions indicate the crystal orientation with respect to the A-plane sapphire plane. The sharp lines in the RHEED patterns indicate that

the growth of the Nb and Au films is epitaxial and follows the layer-by-layer growth mode. Moreover, the niobium and gold RHEED streaks have similar spacings along both directions as expected with calculated surface lattice constants of 2.92Å and 2.83Å respectively.

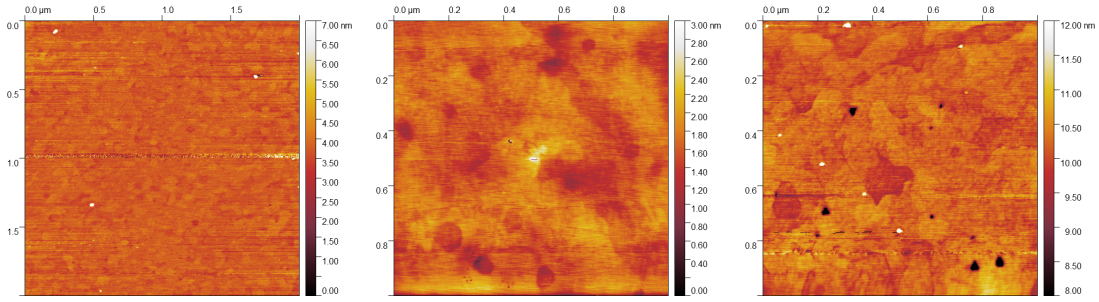

(a) 5nm Au film **(b)** 15nm Au film **(c)** 15nm Au film

Figure 5.2: AFM image showing the smooth surface of a 5nm and 15nm Au film grown on top of niobium.

The smooth surface of the film is corroborated by atomic force microscopy (AFM) images shown in Figure 5.2. The images are taken using a Brudker 5000 Dimension AFM system with the tip engaged in tapping mode. The scans indicate uniform coverage of the sapphire substrate and are even capable of resolving the granular structure of the Au film. These features are the terraces that form from the layer by layer growth observed in RHEED. Occasionally the edges of these terraces will curve at 60° or 120° angles in line with the hexagonal structure of Au (111); this can be seen in the center dark region of Figure 5.2 (c). Some artifacts are present in the AFM scans caused by external vibrations to the equipment during measurement. In addition, pinholes can be observed in some samples which is most likely the result of impurities adsorbed onto the substrate surface prior to growth.

The AFM images shown above correspond to Au films deposited close to room temperature. Normally deposition of Au occurs at elevated substrate temperatures to increase surface mobility of the adsorbed atoms to achieve epitaxial growth [168], but we have found that our films are surprisingly sensitive to temperature. Attempting to deposit Au films at temperatures $\approx 150^{\circ}$ already leads to dissociation of the layer. This is seen in Figure 5.3 in which the Au layer is now composed of a large network of plateaus that percolate across the substrate surface. The surface of the plateaus are quite flat and one can even see repetition of the terraces which indicate layer by layer growth. However, the canyons and valleys that appear are problematic for further deposition of additional materials. The cause of this dissociation at such low temperatures is still unclear and more effort needs to be taken to understand the mechanism driving this effect.

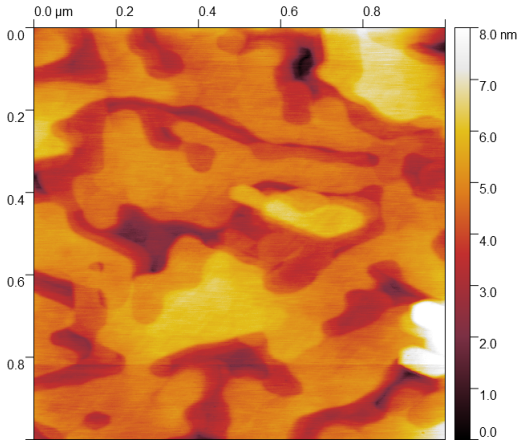

Figure 5.3: AFM image showing the formation of irregular canyons and valleys in the Au film as a result of deposition at elevated temperatures.

5.2 Point Contact Spectroscopy and BTK Theory

A point contact is when two banks of material touch each other but only at a minuscule point. Unlike tunnel junctions where the two banks are separated by an insulating barrier, here the materials are typically in intimate contact, and this changes the physics of the junction. Electrons no longer tunnel due to quantum probability but instead travel in ballistic fashion from side to the other. The condition for this to occur is when the mean free path l is much greater than that of the contact radius a. Surprisingly, a potential difference can still develop across the point contact despite what appears to be a lack of scattering in the contact. The reason is that only a finite current can flow through such a small orifice for a given voltage giving rise to a measurable resistance. This is known as the Sharvin resistance, and it is purely a geometric consequence of the junction [149, 117]. One may also think of this resistance as the result of limiting the number of transverse transmission channels between the two reservoirs of material.

Point contacts can be used to study a number of phenomena, and in this chapter we use this technique to probe superconductors. We consider a point contact made between a normal metal and superconductor. The theory of transport through such a junction is most commonly captured in the framework of BTK (Blonder, Tinkham, Klapwijk) theory [21]. There are four types of scattering processes available for an incident electron from the metal encountering the contact shown in Figure 5.5:

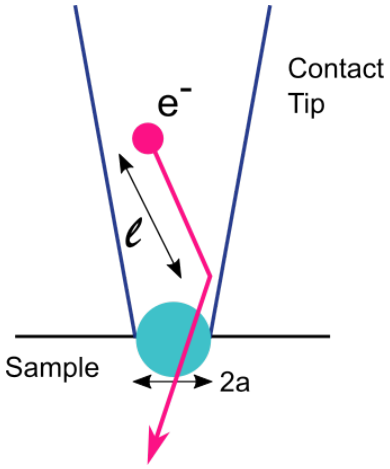

Figure 5.4: Setup of a point contact. Here l is the mean free path of the electron and a is the contact radius. When $l >> a$, the electrons can travel through the contact without any backscattering due to the improbable nature for an electron to make it pass the small orifice and then reflect back through.

1. Andreev reflection with probability amplitude A. A hole is created below the Fermi surface.

2. Normal reflection with probability amplitude B.

3. Transmission as an electron-like quasi-particle (above the Fermi surface) with probability amplitude C.

4. Transmission as a hole-like quasi-particle (below the Fermi surface) with probability amplitude D.

Total probability for all possible events must sum to one: $|A|^2+|B|^2+|C|^2+|D|^2 = 1$. These amplitudes can be found by solving the Bogoliubov-de Gennes equation for the wavefunctions on the normal and superconducting sides with a Dirac delta potential at the

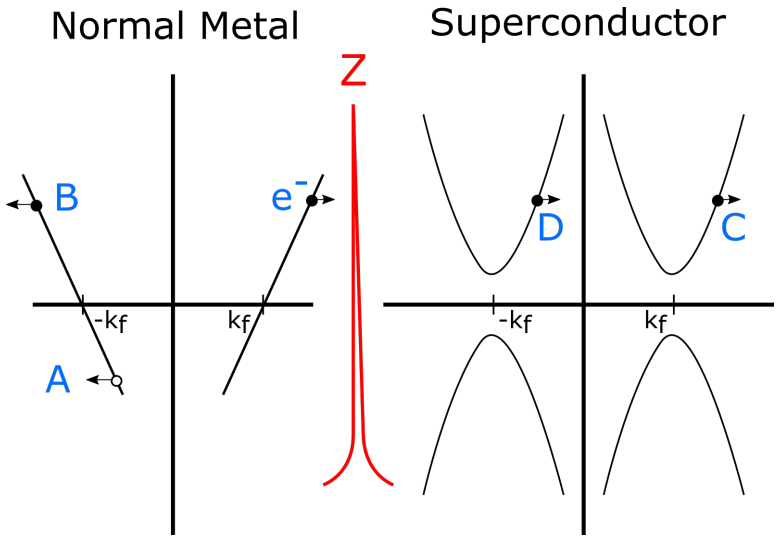

Figure 5.5: Different scattering processes available in a point contact. The black curves are the dispersion relations for the normal metal and superconductor. The figure focuses on the dispersions near the Fermi surface hence the reason the metal's quadratic dispersion appears linear. Here an incident e^- from the normal metal can scatter into 4 possibilities. The red curve is a Dirac delta potential with amplitude Z that separates the two materials and accounts for any barrier that is created from an imperfect contact.

interface to account for any barrier caused by an imperfect contact. One will find that the probability amplitudes will depend on energy E. Following reference [21], we can use these probability amplitudes to find the total current through the junction as:

$$I = 2N_n A e v_f \int_{-\infty}^{\infty} f_{\rightarrow}(E) - f_{\leftarrow}(E) dE \tag{5.1}$$

Here N_n is the density of states of the normal metal, A the contact area, v_f the Fermi velocity, $f_{\rightarrow}$ the electron distribution function for electrons flowing metal $\rightarrow$ superconductor, and $f_{\leftarrow}$ the distribution function for electrons flowing the other way. We

make the assumption that all particles that are incident on the interface, whether it be from the normal or superconducting side, can be described by the Fermi-Dirac distribution $f(E) = 1/(1 + e^{E/k_bT})$. Therefore, $f_{\rightarrow} = f(E - eV)$. As for $f_{\leftarrow}$, we use the fact that all electrons passing through the contact must undergo one of the four processes described above so that we have:

$$f_{\leftarrow} = |A|^2(1 - f_{\rightarrow}(-E)) + |B|^2 f_{\rightarrow}(E) + (|C|^2 + |D|^2)f(E) \tag{5.2}$$

The first term is simply a statement of Andreev reflection in reverse: a hole incident on the interface will drag an electron out of the superconductor and back into the metal; $1 - f_{\rightarrow}(-E)$ is the distribution of holes approaching the interface with the negative energy accounting for the fact that holes lie below the Fermi level μ. Second term is simply the portion of normal reflected electrons that contribute to the reverse current. And the last term is the number of quasi-particles in the superconductor that transmit across as electrons. The total current expression and differential conductance can now be simplified down to:

$$I = 2N_n Aev_f \int_{-\infty}^{\infty} (f(E - ev) - f(e))(1 + |A|^2 - |B|^2) \tag{5.3}$$

$$\frac{dI}{dV} = 2N_n Aev_f \int_{-\infty}^{\infty} (-\frac{\partial f(E - eV)}{\partial V})(1 + |A|^2 - |B|^2) \tag{5.4}$$

This equation simply states that the current through a contact is enhanced by Andreev reflection due to the fact that it is a process that moves *two* electrons across the interface and that normal reflection reduces the current. The specific values for A, B can be found in reference [21], and they differ significantly depending on if $E < \Delta$ or $E > \Delta$. In addition, the strength Z of the Dirac delta potential at the interface also drastically changes

the shape of the differential conductance curve. We plot below several different dI/dV curves with varying Z values showing a transition from a Andreev reflection dominated regime to a tunneling regime.

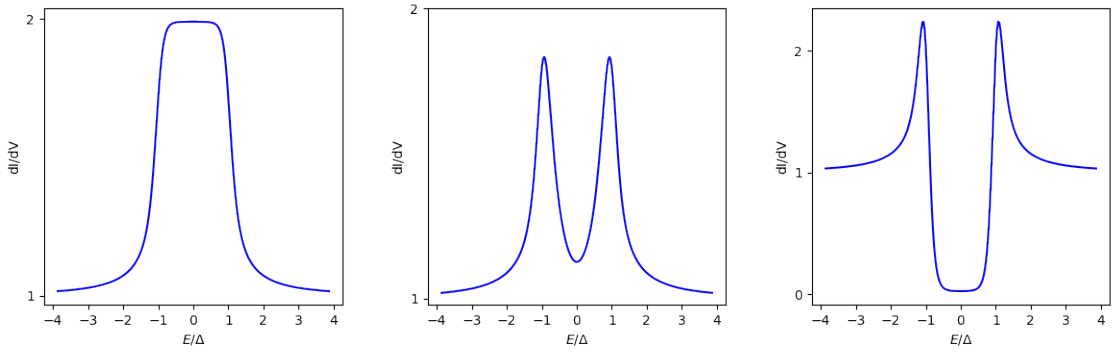

(a) Z = 0 **(b)** Z = 0.5 **(c)** Z = 5

Figure 5.6: Evolution of the differential conductance through a point contact as the barrier strength Z is changed.

At $Z = 0$, the contact is perfect, and below the gap Δ there is a doubling of the conductance compared to that above the gap as expected for Andreev reflection. At $Z = 0.5$, the barrier introduces normal reflection that reduces conductivity below the gap. Finally, at $Z = 5$, the differential conductance mirrors that of a tunnel junction. This evolution is expected because a stronger strength Dirac delta potential isolates the two banks from each other more effectively. Therefore, it is possible for a point contact to convert into a tunnel junction in the limit of high Z. We will take advantage of this fact later in the chapter.

We conclude this section with some final words about generalized models of point contact spectroscopy. The first point is that an additional term Γ can be included in the expressions for the probability amplitudes, A, B, C, D. This accounts for any inelastic

scattering that contributes to broadening of the differential conductance that cannot be accounted for by temperature [128, 28]. The second point is that point contact spectroscopy is actually a "directional" process. This means that the differential conductance depends on the angle with which the electrons are injected into the sample surface [28]. The BTK theory presented above is treated in the 1D limit, but realistic point contacts are 3D. This fact actually allows one to probe for the pairing symmetry in a superconductor and study the Fermi surface topology [124, 56, 29]. Lastly, point contacts can be used to measure the electron-phonon interaction in metals. Backscattering in point contacts introduces a measurable correction to the current that is detectable in the derivative of the differential conductance $\frac{d^2I}{dV^2}$ [28].

5.3 Point Contact Spectra of Au Films

Surprisingly, point contacts can be made using silver paste. Numerous studies of superconductivity using silver paste point contacts have been reported in the literature [28, 30]. The goal is to attach a thin wire, typically gold, onto the surface of the desired material using a small droplet of silver paste. The gold wire serves as one of the source-drain electrodes in the device. A picture of the setup is depicted below.

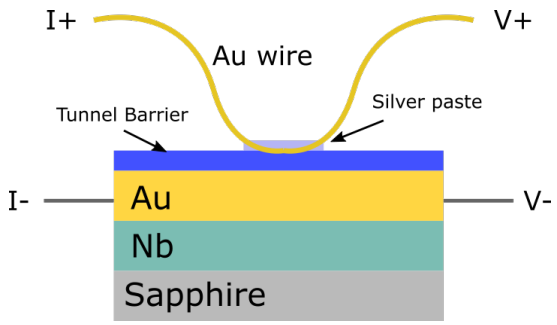

Figure 5.7: Setup of a silver-paste point contact. A thin Au wire is held down by a small droplet of silver paste. A capping layer of Se or Te serves as the tunnel barrier to limit the flow of silver paste onto the Au surface.

This approach may seem counterintuitive as silver paste contacts are macroscopic in size, and one may wonder how a minuscule contact area is achieved with this rough approach. The prevailing theory is that many superconducting materials possess an intrinsic oxide layer on their surface which serves as an insulating barrier. When silver paste is placed on the surface, the silver particles in the paste can migrate into pinholes and imperfections within the oxide layer forming a series of microbridges in the spot area [56]. The size of these defects and the silver particles is microscopic allowing for the surprising formation of point contacts. It should be kept in mind that this approach most likely results in many point contacts in parallel as there is no control over how and where the silver paste diffuses to on the surface.

One issue arises, however, in the Nb-Au films considered here: Au does not oxidized readily. Therefore, there is no intrinsic barrier that forms upon which silver paste can be placed without electrically shorting the electrode to the film. We overcome this problem by depositing a capping layer of selenium (Se) or tellurium (Te) to serve as an artificial

barrier. Both elements are semiconductors with direct bandgaps of 400meV for tellurium and 1.6eV for selenium [66, 63]. Therefore, these materials act as insulators within the range of the low probing voltages used in this study. The selenium or tellurium capping layer is deposited at room temperature in-situ using the MBE chamber after the growth of the Au (111) film. Capping layer thicknesses ranged from 2 - 5nm for Se and 7 - 10nm for Te.

Initial tests were done using Se capping. Figure 5.8 below plot the differential conductance of Se capped Au films taken at 4.2K under zero magnetic field; the data is normalized to the normal state conductance. We observe that adjusting the thickness of the Se capping layer allows for a transition from Andreev reflection dominated transport to tunneling. For 2nm of Se, a single peak at $V_{sd} = 0$mV is found. As the thickness of the Se increases, the peak splits into two coherence peaks and the conductivity below the gap depresses to below that of the normal state value. This fits well with schematic setup of silver paste point contacts. Thinner barriers tend to have larger pinholes or imperfections which increases the likelihood of the silver paste coming into intimate contact with the film. As thicknesses increase, the defects in the capping layer appear less and the only method of transport is through tunneling across the Se barrier.

The transition between the two regimes can be taken into account with BTK theory. The black dotted lines plot the corresponding BTK fits with the Γ parameter included to account for additional possible broadening. The curves fit well with the data (fitting values presented in the table) but indicate that the external broadening Γ is quite large, almost as large as the superconducting gap. This is problematic as any possible finer

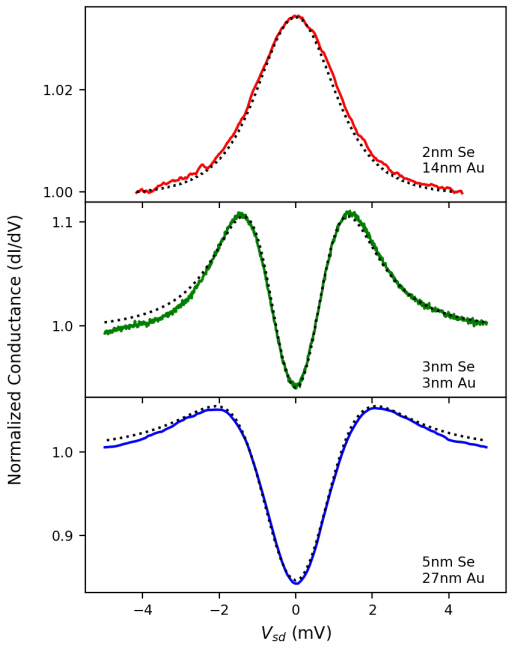

Barrier Thickness	Broadening (meV)	Superconducting Gap (meV)
2nm Se	0.59	0.34
3nm Se	0.73	0.98
5nm Se	0.34	0.92

Figure 5.8: Differential conductance of point contact devices with different Se barrier thicknesses taken at 4.2K. The table shows the fitting parameters used for the BTK fits (black dotted lines). Tuning the Se thickness allows one to transition from an Andreev reflection dominated regime to a tunneling regime.

features are most likely obscured. Furthermore, the subgap conductance is still quite high in comparison to the normal state conductance; in other words, no hard gap is observed.

These problems are summarized in another device shown in Figure 5.9. This plots the differential conductance at 300mK of a 8nm Nb/5nm Au film capped with 6nm of Se as a function of the out of plane magnetic field; the data is normalized in units of the conductance quantum $G_0 = 2e^2/h$. We observe that the measured conductance in the subgap region to be quite large, $\approx$ 8-9 G_0, even though theoretically the superconducting gap should prevent all conduction at these low temperatures. The most probable explanation is provided by

the Landauer formalism [33] which suggests that this is the result of a leaky barrier which allows for multiple transmission channels to remain present even in the superconducting phase. Furthermore, while not shown in the plot, BTK fits to the different slices of the density plot produce broadening values Γ that is on the order of 0.2-0.3 meV, which is once again comparable to the magnitude of the superconducting gap. These results demonstrate that using an Se capping layer as a tunnel barrier is insufficient for detection of Majorana zero modes via tunneling spectroscopy.

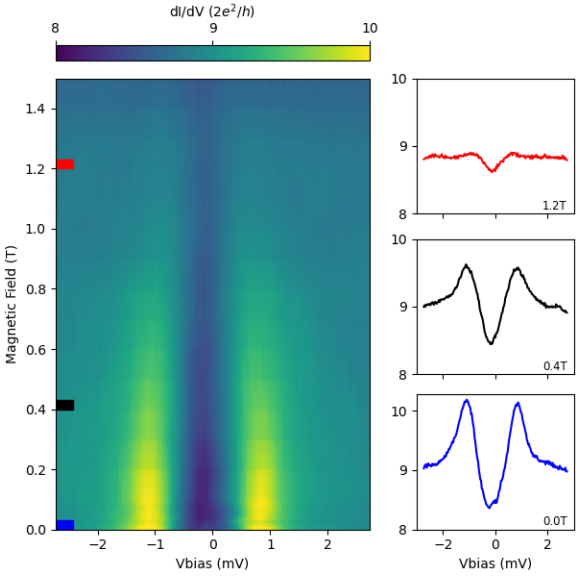

Figure 5.9: Density of plot of the differential conductance of a 8nm Nb/5nm Au point contact device capped with 6nm of Se as a function of out of plane magnetic field at 300mK. The conductance is quite high even in the subgap regime indicating a leaky barrier.

5.4 Tunneling into Gold and Topological Superconductivity

We switch to tellurium as the next choice of tunnel barrier materials. Using 7nm of Te, we immediately find a substantial reduction in the broadening Γ. We believe this is the result of better crystalline quality and uniform coverage of the tellurium film. Figure 5.10 plots the differential conductance taken at 300mK of a 15nm Au / 8nm Nb bilayer capped with 7nm Te. Here we observe a bulk superconducting gap of $\Delta_B \approx 0.85$meV and the appearance of two smaller subgap peaks at ± 0.33meV. We claim these smaller peaks are in fact the coherence peaks of a second superconducting gap forming in the surface bands of Au (111). Two points support this notion. First, the conductance at $V_{sd} = 0$mV is dramatically reduced in comparison to the Se capped samples which demonstrates the device operates as a tunnel junction instead of a metallic point contact. This fact is corroborated by fitting the data to a superposition of two BTK curves of equal weights (black dotted line) with the broadening Γ limited by the resolution of the dV voltage sweep used in the measurement. The fit gives a barrier strength of $Z \approx 2.57$ for the BTK curve corresponding to the bulk gap which means the contact lies within the tunneling regime. Therefore, the conductivity is dominated by quantum tunneling at the interface instead of ballistic transport into the bulk Au film.

Secondly, the smaller peaks retain their position under application of a magnetic field. Figure 5.11 plots the differential conductance of the device at 300mK as a function of the in-plane magnetic field. The density plot shows the subgap peaks maintain their location with increasing field in contrast to possible spinful Andreev bound states which would shift in energy in response to the Zeeman interaction. As a result, it is reasonable to

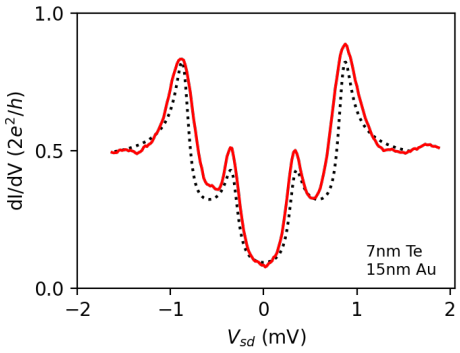

Figure 5.10: Differential conductance of a 8nm Nb/15nm Au/7nm Te point contact device. The extrinsic broadening Γ is reduced significantly allowing for the observation of a second superconducting gap. The subgap conductance also approaches zero indicating that the device is truly in the tunneling regime.

conclude that the smaller peaks correspond to a surface gap of $\Delta_s \approx 0.33$meV.

Interestingly, the surface gap does not persist for all values of the magnetic field. In Fig 5.11, the surface coherence peaks disappear around 1.2-1.4T when the tunneling spectra changes from a "U" to a "V" shape, but the bulk gap persists beyond. Closing the surface gap but maintaining bulk superconductivity marks a boundary between two superconducting regimes that may be attributed to a possible phase transition. In a superconductor with Rashba spin-orbit coupling such as this one, the influence of the in-plane magnetic field can drive the system into a gapless phase where the ungapped portions of the Fermi surface correspond to Bogoliubons with zero energy [182, 123, 177]. The transition is predicted to occur when $\Delta = g\mu_B$ with g, μ_B corresponding to the Landé g-factor and Bohr magneton, respectively. Substituting in the value of the surface gap and corresponding magnetic field allows us to get a rough estimate of the g-factor as ≈ 4, twice the usual value of 2. This is

a most unusual result as gold is known to have the standard g-factor of 2 [110], and we will see further evidence of changes in the gyromagnetic ratio is subsequent devices.

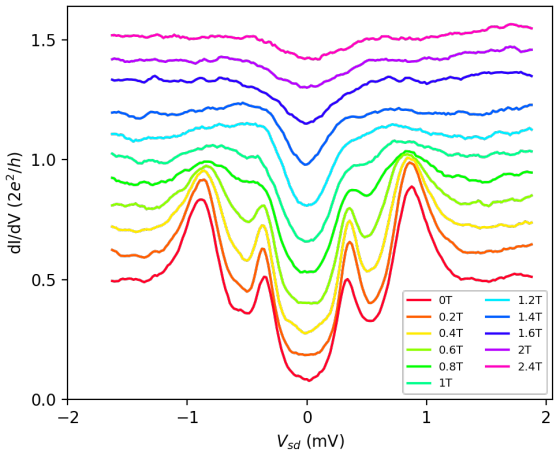

Figure 5.11: In-plane magnetic field dependence of the dI/dV of the device listed in Figure 5.10. As the field increases, the two peaks at ± 0.33meV do not change in energy which helps to solidify that they are in fact the coherence peaks of the surface gap.

A cleaner transition between the two superconducting regimes is observed in a thinner 5nm Au/8nm Nb bilayer sample capped with 10nm Te. The differential conductance taken at 300mK as a function of the in-plane magnetic field is plotted in Fig 5.12a. As before with the 15nm Au sample, the zero field subgap conductance at $V_{sd} = 0$mV approaches zero indicating the device operates within the tunneling regime. However, the presence of the additional coherence peaks from the surface gap is noticeably missing. It should be pointed out that the Au film in this device is only 5nm thick so the proximity effect is expected to induce a larger gap into the Au (111) surface bands in comparison to the 15nm Au sample shown in Fig. 5.11. Therefore, the superficial disappearance of the surface gap is most

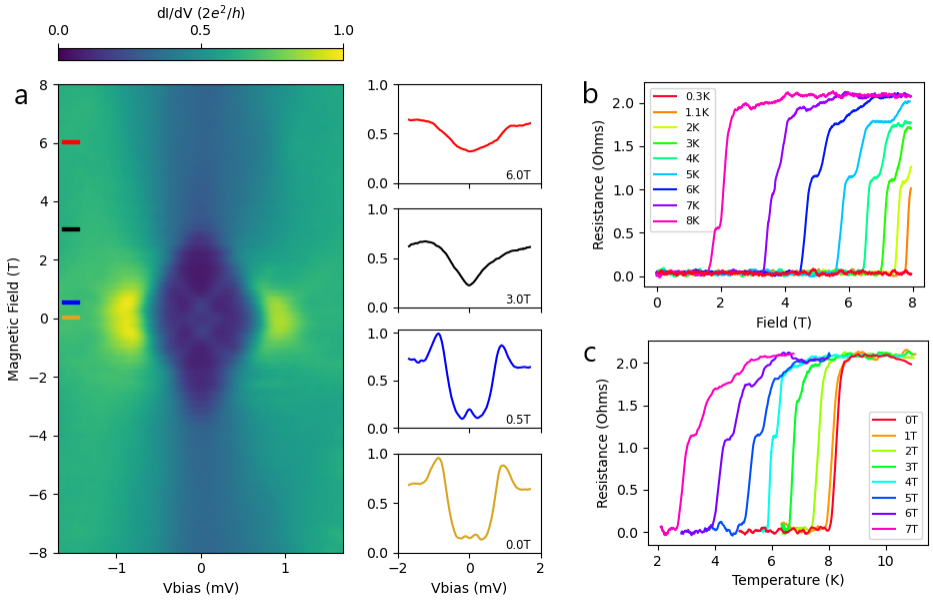

Figure 5.12: (a)Differential conductance of a 9nmTe/5nm Au/12nm Nb film at 300mK as a function of the in-plane magnetic field. A diamond-shaped gap structure is observed along with the appearance of Andreev bound states (b) 4-terminal resistance vs. field at different temperature. (c) 4-terminal resistance vs. temperature at different in-plane magnetic fields.

likely the result of significant overlap with the bulk gap.

Still, the presence of superconductivity in the surface states is detectable from its magnetic field dependence. The density plot in Figure 5.12 reveals the presence of a diamond-shaped structure which we attribute to be opening and closing of the surface gap. The upper and lower tips of the diamond at ± 3T are where a noticeable transition occurs in the shape of the tunneling spectra as the curves change from a "U" to a "V" shape. From this point onwards, the tunneling gap continues to persist albeit wider and shallower. We emphasize that superconductivity is still present in the sample as indicated in Fig 5.12b,c; the four terminal resistance measurements clearly indicated that the film remains

superconducting at 300mK for all ranges of the magnetic field. This further points to the possibility of gapless superconductivity present in the surface states of Au (111) [182, 123].

A subsequent sample of 8nm Nb/10nm Au/9nm Te showed similar behavior. Figure 5.13 plots the differential conductance through a point contact on the 10nm Au film in the tunneling regime at 300mK. We observed only a single set of coherence peaks at $\pm$0.5meV, and the associated gap closed much faster, disappearing at only around 0.5T for in-plane fields. The presence of Andreev bound states is also observed, as seen in the zero field plot. Furthermore, these states appeared to shift in energy as the in-plane field changes but the fast closing gap obscures the traces. We emphasize as before that bulk superconductivity is still present in the film as shown in Figure 5.14. A broad but noticeable gap feature is still observed and the resistance of the film remains at zero at 300mK through the sweep of the magnetic up to 3.25T. Therefore, we have further evidence of the ability to close the gap without the destruction of bulk superconductivity.

The origin of the rapid reduction of the gap at small in-plane fields is unclear given that the prior 14nm Au thick film showed a gap closing closer to 1T. Moreover, the lack of a second pair of coherence peaks calls into question whether the features correspond to the surface gap or the bulk gap. Current evidence suggests the former claim for two reasons. First, the zero field transition temperature suggests an estimated BCS gap of approximately which does not correspond to the $\pm$0.5meV peaks. Secondly, the subgap conductance is lower in this device in comparison to previous point contacts. This further suggests that conductivity is strictly limited to only the tunneling at the interface between the gold and tellurium layers, and it should not have significant contributions from the bulk. But, neither

of these reasons account for the closing of the gap at small fields. In the next section we discuss evidence of a possible mechanism that could result in this effect.

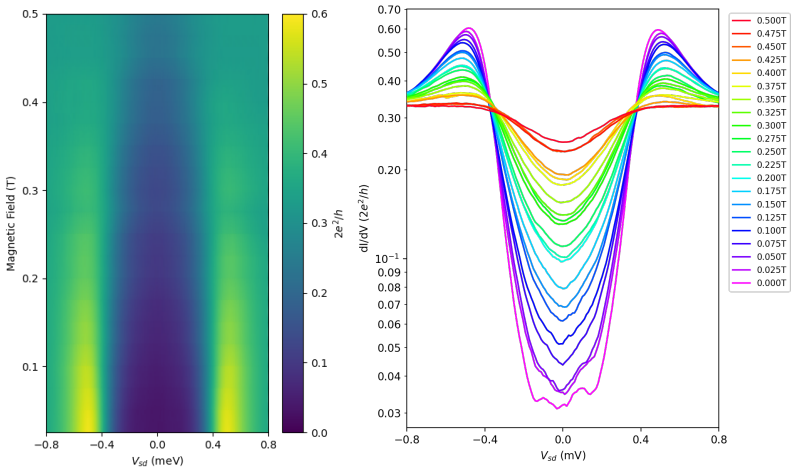

(a) **(b)**

Figure 5.13: (a)Differential conductance of a 9nmTe/10nm Au/8nm Nb film using silver paste point contacts in the tunneling regime as a function of the in-plane magnetic field at 300mK. Unlike prior films, the in-plane field appears to close the superconducting gap much sooner at only $\approx$ 0.5T. (b) Logarithmic plot of the data in sub-figure (a). The appearance of subgap Andreev bound states is visible at zero field.

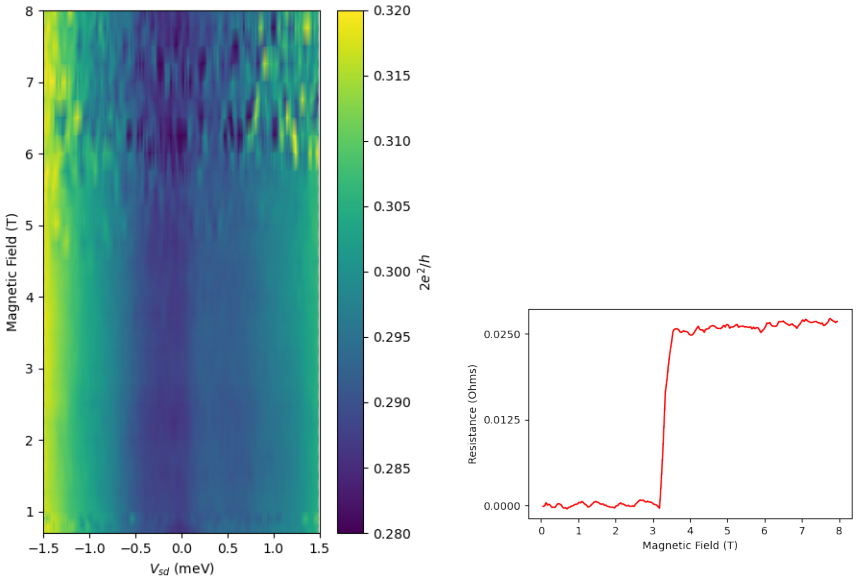

(a) **(b)**

Figure 5.14: (a)Differential conductance of a 9nmTe/10nm Au/8nm Nb film using silver paste point contacts in the tunneling regime as a function of the in-plane magnetic field at 300mK at higher fields. A broad but noticeable gap feature is still observable. (b) 4-terminal resistance vs. field at 300mK. This shows that superconductivity is still present up to $\approx$ 3.25T.

5.5 The Enhanced Landé g-Factor

In addition to the surface gap, we also observe two smaller subgap peaks corresponding to the formation of Andreev bound states in the 5nm Au/12nm Nb film. These symmetric peaks are present at zero field and shift in opposite directions as the in-plane field is changed. They coalesce at zero bias at around $\pm$0.5T before merging into the coherence peaks at +/-1T; their paths are traced out in Fig. 5.15a. The fusion of two Andreev bound states at zero bias has previously been discussed as possible evidence of the formation of

Majorana bound states [35], but we emphasize that this is not the case here. A line cut at zero bias shown in Fig. 5.15b makes it clear that the zero bias peak is unstable with respect to the magnetic field. A true zero bias peak corresponding to a Majorana zero mode would appear only after the gap closes and persist until superconductivity is destroyed [6, 40].

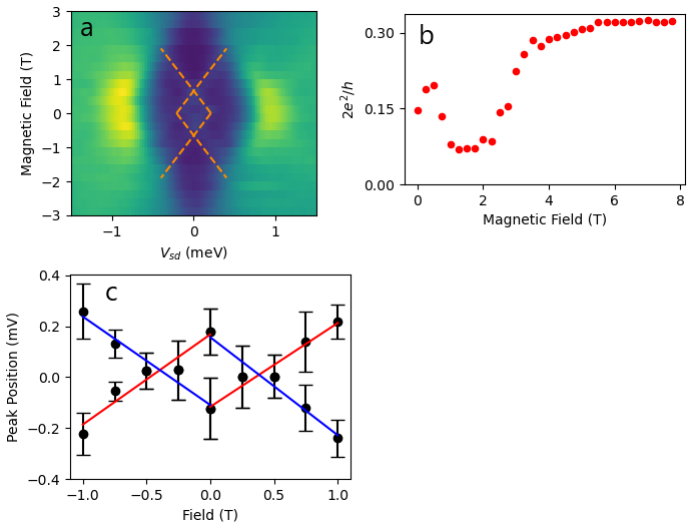

Figure 5.15: (a) Highlighted paths of the Andreev bound states. (b) Line cut at $V_{sd} =$ 0mV of the density plot in Figure 5.12a. The zero bias peak appears at 0.5T but does not persist indicating that it cannot correspond to a Majorana zero mode. (c) Position of the Andreev bound states as a function of the magnetic field. The colored lines correspond to linear fits with red (blue) corresponding to up (down) spins. The average g-factor is ≈ 12 based on the fits.

However, the slope of the trace lines in Fig. 4a suggests that the Zeeman energy acquired by the bound states is quite large. To confirm this, we plot out the subgap peak positions with respect to the field in Fig. 4c. The data is fitted to the Zeeman energy $g\mu_B B$ with spin S $= \frac{1}{2}(-\frac{1}{2})$ corresponding to the red (blue) lines. From this, we extract an

average Landé g-factor of ≈12, a six-fold increase above the conventional $g = 2$. This large g-factor associated with states at the interface between the Au and Te layers increases the acquired Zeeman energy and allows the magnetic field to overcome the surface pairing gap sooner than the bulk; this also corroborates well with the early closing of the surface gap in the device featured in Figure 5.11 and in Figure 5.13. Enhanced g-factors are desirable for topological superconductors because they allow for a topological phase transition using smaller magnetic fields that will not destroy superconductivity [80, 98]. Furthermore, this effect is a local one: it only occurs at the interface between Au and Te. Reducing the lateral dimensions of the Te layer to a thin quasi-1D nano-wire on top of the Nb/Au film can can serve as a fruitful playground for exploring the formation of Majorana zero modes [123, 177].

Now we discuss possible origins for this enhanced g-factor. Given that gold and niobium both possess the standard g-factor of 2 [177], it suggests that the observed effect is caused by the tellurium barrier. The g-factor of a bound state is determined not just by the main host material but also the confining barriers where the tails of the wavefunction leak into the classically forbidden area. This effect has been observed in GaAs/$Al_xGa_{1-x}As$ quantum wells in which electrostatic gates are used to push the confining potential, and consequently the bound state, into the barriers thereby changing the gyromagnetic ratio [139, 155]. However, it is not clear whether leakage into the tellurium barrier can account for the observed six-fold increase in the g-factor in this scenario. This is especially true considering that there is no obvious mechanism which would shift the Andreev bound states further into the barrier.

Another possible cause may lie in the effects of spin-orbit coupling. Deviations from the free electron $g = 2$ can occur as a consequence of spin-orbit interaction on the band structure of a semiconductor; this was shown to account for the large $g \approx 50$ seen in InSb [136]. The Roth-Lax-Zwerdling formula for the gyromagnetic ratio in semiconductors depends on both the spin-orbit interaction strength and the size of the band gap [136]. Smaller band gaps and larger spin-orbit strengths can lead to higher g-factors. Tellurium is a narrow, direct band gap (≈ 0.4eV) semiconductor and since it is in proximity with the Au (111) surface which has large spin-orbit strengths of ≈ 50meV, this would naively suggest a possibly larger value for g [10, 85].

However, the aforementioned formula is typically applied to semiconductors with zinc-blende structure in which the Dresselhaus spin-orbit interaction is of primary concern [38]. The scenario here is that the bound state observe lives within the gold film and not within the tellurium capping layer, at least not a significant portion of it. Therefore, it is not clear how spin-orbit effects in the tellurium play a role in the apparent shift. An alternative explanation might suggest that spin-orbit effects in the Au (111) surface are responsible, but, to the author's knowledge, no prior work has been done to reveal any discrepancies between the surface and bulk g-factors in gold. Moreover, it remains to be seen if the observed g-factor is anisotropic as only one field direction has been measured.

One final point arises in this discussion in regards to the origin of the Andreev bound states. These states can appear whenever there are variations in the superconducting gap that allow for multiple Andreev reflections to create a bound state. Reports of similar Andreev bound state behavior was seen previously in aluminum/iron interfaces [19]. These

subgap states are the result of spin-dependent phase shifts caused by the ferromagnetic iron lead. However, it is not clear if this is the mechanism behind the observed states as tellurium is not inherently magnetic. Previous reports of current induced magnetization have been observed in bulk trigonal tellurium [49], but whether this effect is present in thin films remains to be seen.

Another probable cause may come from magnetic impurities in the silver paste used to form the contact. But, prior reports indicate that silver paste is not hysteretic [51], and no magnetization should be present at zero field. Therefore, one might expect the Andreev bound states to coalesce at zero bias when the field is zero because there is no magnetization present to create spin-dependent scattering to differentiate up and down spins. Yet, the trace lines in Figure 5.15 (a) clearly shows the bound states split at zero field. The cause of this splitting is currently still unknown and more investigation is required.

To conclude, the enhanced g-factor that appears to be caused by the deposition of tellurium is attractive because it allows for a larger Zeeman effect. However, it is still an open question whether this material can meet the requirements for topological superconductivity in gold. In particular, it has yet to be established that deposition of tellurium is capable of tuning the Fermi energy of the gold surface. This is a necessary ingredient as it dictates the size of the topological regimes one can achieve. More work must be done in either point contact devices or tunnel junctions to observe whether the surface band edge has shifted after tellurium deposition. Additional studies must also be conducted to uncover the origin of the enhanced gyromagnetic ratio. This is important as it can determine whether the effect is electrically tunable, a powerful capability for the control and manipu-

lation of possible Majorana zero modes. For example, Ge/Si nano-wires and quantum dots can experience significant changes in the g-factor for holes as a consequence of spin-orbit interaction which can be modified via electric fields [46, 75]. These experiments can also help to further elucidate the origin behind the Andreev bound states and determine if they are a consequence of tellurium or magnetic impurities.

Chapter 6

Tunable Superconductivity in NbSe2 Thin Films

6.1 Transition Metal Dichalcogenides (TMDs)

6.1.1 First there was graphene

The 2010 Nobel prize in Physics was awarded to Andre Geim and Konstatin Novoselov for their ground-breaking work in graphene, an atomically flat sheet of carbon organized in a honeycomb lattice [1, 119]. The key ingredient to this achievement laid in the successful isolation and identification of graphene using a combination of sticky tape, high quality graphite crystals, and properly tuned thicknesses of silicon oxide on silicon wafers [53]. This discovery has put graphene in the spotlight as researchers eagerly explore new applications for this material [118, 15].

One of graphene's main selling points is the effect of dimensionality. Whittling the thickness of a crystal down to a nanometer or less does more than simply reduce the amount of material present. For one, the surface area to volume ratio increases dramatically which allows graphene to act as an excellent sensor for chemical detection [144]. Structural integrity can also ironically improve due to the removal of weak van der Waals interactions. This is why graphite appears weak and yet graphene is one of the strongest tensile materials to date [87]. In this thesis, we are concerned with another important effect of dimensionality, and that is confinement. Quantum mechanics starts to play a large effect on the electronic properties of solids when the electrons are confined to small regions and what better way to confine electrons than by reducing the size of the crystal in which they live. A famous example in the context of graphene is the photon-like dispersion of the electrons which leads to a half-integer quantum Hall effect [187]. This is why graphene and other layered materials serve as ideal playgrounds for studying physics in a truly 2D world.

6.1.2 Now comes transition metal dichalcognides (TMD)

In the wake of graphene's success came the next generation of 2D materials, and amongst them a family of compounds known as transition metal dichalcogenides (TMDs) rose to the forefront. These materials are similar to graphene in that bulk crystals are composed of 2D sheets stacked on top of each other, however their elemental composition distinctly separates them from their carbon counterparts.

Firstly, in contrast to graphene's singular and signature honeycomb lattice, monolayer TMDs possess three commonly found structural phases: 1T (octahedral), 1H (trigonal prismatic), and 1T' (orthorombic) [183]. The 1H polytype is of particular interest because it has a honeycomb lattice like graphene except that the two sub-lattices are composed of different elements resulting in a crystal that lacks inversion symmetry. Consequently, the band structure at the K and K' valleys of the Brillouin zone are no longer equivalent, and this allows one to distinguish the two points by a new "valley" degree of freedom [176, 175]. The Hall effect has been used to confirm this fact by showing that charge carriers from different valleys move in opposite directions resulting in a opposite Hall voltages depending on the carrier type [102]. In fact, a new field of research dubbed "valleytronics" has arisen from the ability to tune this extra knob in 1H TMDs [143]. Similar structure-driven physics has also been discovered in the case of 1T' TMDs in regards to the quantum spin Hall effect [133].

Structural considerations aside, the variety of elemental compositions and ability to adjust the thickness with sub-nanometer resolution have allowed TMDs to occupy a wide variety of possible electronic behavior from insulator all to way to superconductor [106]. For example, the inclusion of heavier elements leads to stronger spin-orbit interaction in TMDs than in graphene allowing for new spin-correlated phenomena to be explored [166]. In addition, reducing the number of layers causes a dimensional crossover from the 3D to the 2D limit where confinement effects can significantly alter the physics. In the case of MoS_2, multi-layer samples are indirect bandgap semiconductors whereas a monolayer has a direct gap [103]. Similarly, monolayer $NiTe_2$ has been theoretically predicted to superconduct

despite the bulk lacking any such ability [188]. The reduction in dimension also permits researchers to use gating to tune the electron density over a significant portion of the sample. An famous example is the ability for thin flakes of MoS_2 to transition from a band insulator to a superconductor under high doping from ionic liquids [180].

Furthermore, there is no a priori reason why one must limit themselves to just one TMD material. The van der Waals structure of these layered crystals offer a convenient path for researchers to engineer new designer materials by stacking different TMDs on top of each other to form heterostructures [96]. The interaction between layers can enable new physics and applications not present in naturally occurring substances [190, 89]. One can go even further and adjust the relative angle with which one stacks a layer on top another. This can alter the electronic properties of the total structure through the creation of Moire superlattices and has opened up a whole new field of "twistronics" [25]. This idea was first demonstrated in "magic-angle" graphene in which superconductivity emerged as a result of the angular misalignment of two graphene sheets [185, 24].

6.1.3 Superconductivity in NbSe2

A number of TMDs are known to exhibit superconductivity. The transition to this phase can either occur naturally, be induced by gating, or through chemical intercalation [173, 150, 180, 12, 106]. The unique crystalline structure of TMDs endows superconductivity in these systems with novel properties. Among the possible candidates, we focus on 2H-$NbSe_2$ in this thesis.

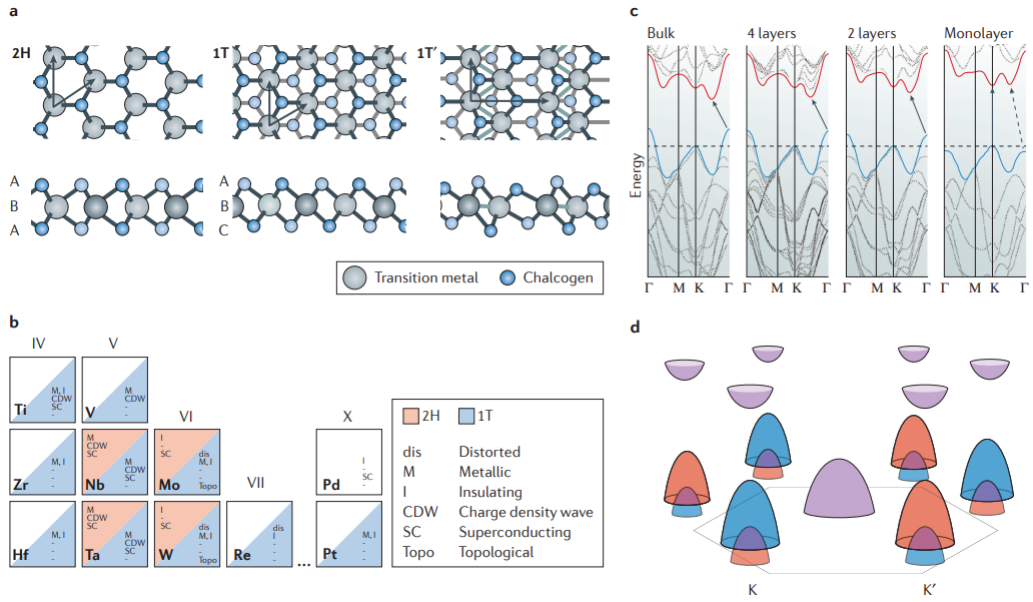

Figure 6.1: (a) Diagram showing the different polytypes commonly found in layered TMD materials. (b) Table of different layered TMDs. (c) Band structure of MoS_2 as number of layers changes. (d) Schematic representation of the band structure of 1H MoS_2. The orange and blue colors correspond to up and down spin bands. The K and K' valleys have opposite spin splitting as a result of inversion symmetry breaking and spin-orbit interaction. Figures adapted with permission from Springer Nature: Nature Review Materials, reference [106], Copyright 2017.

2H-$NbSe_2$ is an type-II s-wave superconductor that can superconduct down to even a monolayer [43, 161]. As discussed before, the honeycomb lattice of TMD materials results in a lack of inversion symmetry. Consequently, a strong spin-orbit field at the K and K' valleys of the Brillouin zone appears and polarizes the spins of the electrons to the out of plane direction. This is commonly referred to as Ising spin-orbit coupling and the effect as spin-valley locking [138, 58]. Therefore, pairing electrons at the K and K' valleys results in Cooper pairs that are unusually robust against in-plane magnetic fields because of their affinity to align along the spin-orbit field instead.

Evidence of this effect has been observed in mono and few layer $NbSe_2$ [173]. In fact, the spin-valley locking is so strong that superconductivity persists even beyond the Pauli limit which is defined as the field needed for the Zeeman effect to align the spins in a singlet Cooper pairs, $H_p \approx 1.86T_c$. The estimated upper critical in-plane field H_{c2} was determined be $\approx$ 35T, over six times larger than the Pauli limit. Similar observations have also been seen in gated MoS_2 [97, 137]. Enhancement of the in-plane critical field has been discussed previously in terms of spin-orbit scattering in which disorder randomizes the electrons spins and prevents alignment by magnetic fields [74]. However, the TMD samples studied were crystalline exfoliated flakes in which disorder was low and mean free paths were long so scattering effects were ruled out as a viable explanation. This novel type of spin-orbit enhanced superconductivity has been dubbed Ising superconductivity and serves as an example of new correlated physics present in TMD materials.

However, enhancement of the critical field is not the primary motivation for exploring $NbSe_2$ in this work. Rather, the presence of strong, intrinsic spin-orbit interaction in a superconductor like $NbSe_2$ makes it an attractive candidate for realizing Majorana fermions. Several theoretical proposals have already explored this possibility in a number of ways. In particular, it has been demonstrated a priori that pushing monolayer 2H-$NbSe_2$ beyond the Pauli limit induces a transition to a nodal topological superconductor [58, 146]. The band structure in this phase is characterized by gapless nodes that are connected by Majorana flat bands which allow for chiral Majorana edge states to appear. The ability to tune this transition via only the magnetic field is particularly enticing when compared to the semiconducting nano-wire approach that involves multiple parameters. So far, no

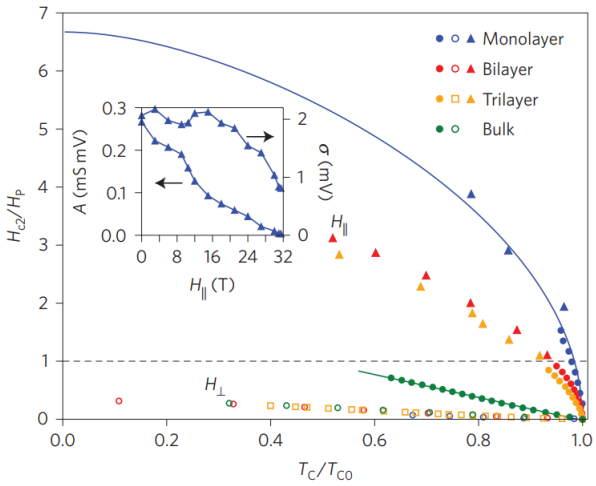

Figure 6.2: H-T phase diagram of few layer $NbSe_2$. As the sample thickness approaches the monolayer limit, the in-plane critical field can easily rise above the Pauli limit. Reprinted/adapted by permission from Springer Nature: Nature Physics, reference [173], Copyright 2015.

experimental observation of Majorana states have been reported using this approach. Another suggestion for achieving topological superconductivity is to p-dope monolayer TMDs to promote triplet pairing between electrons in the same K or K' valley that results in p-wave superconductivity [60]. Another is to leverage the Ising spin-orbit coupling in TMDs to generate Majorana zero modes in chains of magnetic impurities [148]. In general, bulk $NbSe_2$ is a popular substrate for exploring 2D topological superconductivity. Recent experiments have observed evidence of Majorana fermions present at the interface between $NbSe_2$ and 2D ferromagnets or topological insulators [70, 17, 178].

In summary, $NbSe_2$ has demonstrated to be a fertile playground for exploring novel superconducting phenomena, and it is for these reasons why we explore the synthesis and characterization of this material.

6.2 Growth of NbSe2 Thin Films

A vast portion of TMD research utilizes the scotch-tape method for acquiring thin flakes. This approach is fine in a research setting but severely lacks in scalability. Here we detail efforts taken to synthesize thin films of $NbSe_2$ in the 2H-phase using MBE on c-plane sapphire substrates [27].

The substrates were purchased from Shinkosha Co. Through various tests, we found that Shinkosha's STEP c-plane sapphire yielded the best results. Growth of $NbSe_2$ on c-plane sapphire might seem counterintuitive given the lattice constants for sapphire (a $\approx 4.76\mathring{A}$) and $NbSe_2$ (a $\approx 3.44\mathring{A}$) differ quite a bit [107]. However, the crystal structure of TMDs suggest growth is still possible as the out of plane bonds are van der Waals in nature so interfacial coupling between the substrate and deposited layers is reduced. Furthermore, if one examines supercells of $NbSe_2$ and sapphire, the lattice mismatch reduces to only $\approx$7.8%. This type of superlattice matching has been reported in the growth of WSe_2 on c-plane sapphire [114]. Below we outline the general growth procedure taken in Figure 6.3. All samples used in this study are capped with Se to prevent oxidation.

We find that deposition of a half to one monolayer buffer layer aids in the growth of subsequent layers for low temperature growth samples. In addition, we also employ Nb-flux interruption during the growth to extend the reaction time between the adsorbed Nb and Se atoms on the substrate. The elevated substrate temperatures used in the deposition are above the sublimation temperature of selenium so the sticking probability of Se atoms is quite low in comparison to Nb. By closing the shutter to the Nb source at regular intervals, we can oversupply Se and extend the Nb:Se ratio. This strategy has been previously

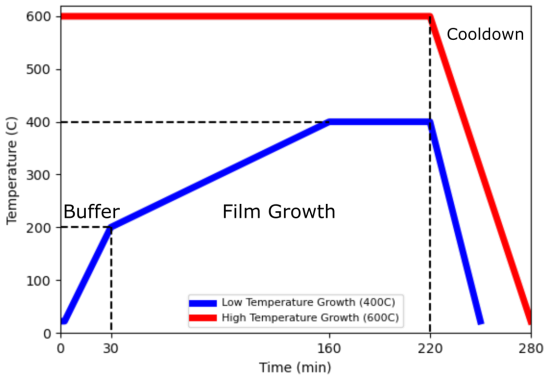

Figure 6.3: General temperature profile of $NbSe_2$ growth. For the low temperature growth, an initial buffer layer is grown at room temperature and then annealed to 200°C. From there the main film growth occurs. We find that the best results involve a slow heating ramp to the final temperature of 400°C. The high temperature growth samples do not utilize a seed layer and simply start at 600°C.

employed to achieve epitaxial growth of $NbSe_2$ on GaAs, WTe_2 on MoS_2, and WSe_2 on sapphire [179, 183, 184]. The effective flux ratio (Se:Nb) used is approximately 120:1.

Quality of the films is confirmed in several ways. Representative RHEED of the deposited films are shown in Figure 6.4. Six-fold repetition of the RHEED pattern is observed when the substrate is rotated about its azimuthal axis as expected for a film with a honeycomb lattice. A TEM cross section of a 5 monolayer film further proves that the growth is layer by layer by clearly resolving each individual layer. Moreover, the layers are continuous over a wide distance. X-ray diffraction also confirms the uniform spacing of the layers as shown in Figure 6.5 (a) in which the characteristic c-axis diffraction peaks appear. The corresponding Miller indices are all even because the unit cell of 2H-$NbSe_2$ encapsulates

two monolayers [107]. Element-selective x-ray spectroscopy (EDX), shown in Figure 6.5 (d) further highlights the clear interface formed between the deposited film and the substrate. The relative signals from the Nb and Se also found to follow the stoichiometric ratio of 1:2 as expected for $NbSe_2$.

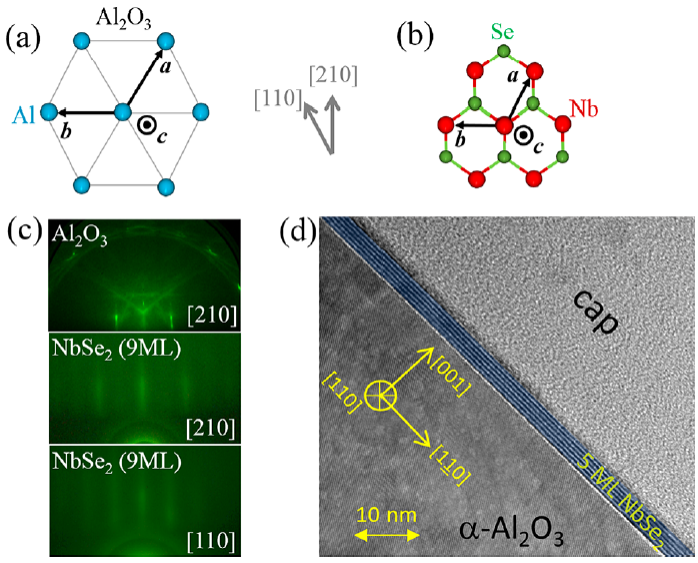

Figure 6.4: (a) Schematic showing the Al atoms on sapphire (0001) surface. (b) Schematic of NbSe2 surface and its epitaxial orientation with respect to the substrate in a. (c) RHEED patterns: sapphire substrate along the [210] direction (top), 9 ML NbSe2 along the [210] direction (middle), and along the [110] direction (bottom). (d) TEM image of a 5 ML NbSe2 sample. It can be clearly seen that each NbSe2 monolayer extends continuously over a large scale. Reprinted with permission from reference [27], Copyright 2020 American Chemical Society.

6.3 Strain Controlled Superconductivity in NbSe2

Surprisingly, we find that the transport properties of the $NbSe_2$ films can be tuned by adjusting the substrate temperature during growth. Shown in Figure 6.6 a,b, the film resistance versus temperature indicates a transition from superconducting to insulating behavior as the growth temperature of the film increases. With a 400 °C substrate temperature during deposition, the film is wholly superconducting. But once temperatures approach 600 °C, an upward U-turn is seen in the data. The samples were measured in a custom liquid He dipping probe with a base temperature of 1.6K which is why some plots do not show the full resistivity drop as the $NbSe_2$ film becomes superconducting. Attempting to fit the data to a variable-range hopping model does not work well which indicates the transition is not the result of film degradation induced by elevated temperatures [112]. Instead, fitting the plot of ln(R) vs T^{-1} (Figure 6.6 (a, inset) to a linear curve describes the data more adequately. The conductivity is therefore governed by an energy gap: $\sigma \approx e^{-E/k_BT}$ with $E/k_B \approx 6.7K$.

Despite the obvious change in transport behavior, RHEED does not reveal any noticeable changes. Therefore, we turn to Raman spectroscopy to elucidate the cause as it provides a more sensitive probe of the structural changes in a material [140, 14]. Figure 6.6 (c, d) shows the Raman spectra for a 5ML $NbSe_2$ film and a bulk crystal. Identification of the peaks is done via polarized Raman in which the p-polarization turns off the A_{1g} peak while maintaining the E^1_{2g} peak, consistent with prior reports of 2H-$NbSe_2$ [174]. Both spectra resemble each other, but there is a clear blue-shift of the E^1_{2g} peak in the MBE grown film while the A_{1g} peak red-shifts. This implies a hardening of the in-plane phonon

modes as the E^1_{2g} peak corresponds to an in-plane shearing vibration [126]. The hardening of a mode is often unfavorable for superconductivity.

Additional measurements of the Raman spectra were taken to further study the changes in the E^1_{2g} and A_{1g} peaks. Three samples with different transport properties (insulating, superconducting, and one in between) were used in the study shown in Figure 6.7 (a); the corresponding resistance versus temperature plots are shown in Figure 6.5 (a). We quantify the E^1_{2g} and A_{1g} peak positions via Gaussian peak fitting. A clear wavenumber shift from 245 to 260 cm^{-1} is observed for the E^1_{2g} peak when comparing the superconducting sample ($T_g \approx 400°C$) to the insulating one ($T_g \approx 600°C$). This shift is validated by alignment of the sapphire peak at 418 cm^{-1} which remains constant because the growth temperatures are too low to cause substantial changes to the substrate's crystal structure. The cause for this shift is most likely due to in-plane compressive strain that arises from the film coupling to the sapphire. Additional confirmation is provided by selective area diffraction of the film. Figure 6.7 (b) plots the line profile of the diffraction peaks for a superconducting and insulating sample. The (122) diffraction spot shifts to higher k-values for the insulating sample when compared to the superconducting one which confirms the formation of in-plane compressive strain. The red-shift of the A_{1g} is corroborated by XRD measurements of the c-axis lattice constant. We find that the insulating films possess a lower (002) peak as shown in Figure 6.7 (c) indicating expansion in the c-axis direction. This expansion can also be the result of in-plane compression bunching the film.

The results presented here qualitatively match well with the predictions of BCS theory which states that the electron-phonon coupling strength is weakened when the lattice

stiffens, such as when compressive strain is present [18]. Similar results were also observed in the TMD material MoS_2 [48]. One possible alternative explanation is that the film undergoes a structural phase transition from the 2H to the 1T phase under high temperature growth. Prior work showed that 1T-$NbSe_2$ is a Mott insulator which can be achieved by growth at higher substrate temperatures, and this could account for the insulating transport behavior seen in some samples [115]. However, density functional theory calculations from collaborators determined that the active Raman modes are very different between the two polytypes. We instead infer that strain is the main culprit behind the film's transition from a superconductor to an insulator at low temperature. This is supported by the fact that strain can modify the band structure of TMD materials which can account for the observed gap seen in the resistance measurements [61].

To conclude, we have observed the tuning of superconductivity in $NbSe_2$ via strain. Moreover, achieving this effect was accomplished entirely in-situ via temperature adjustments to the MBE growth procedure. This can allow one to induce specific properties in superconducting devices through the tuning of a single knob. In addition, the thin layered structure of $NbSe_2$ makes it a fertile playground for exploring all manners of proximity effects that can lead to topological superconductivity [189, 58, 60].

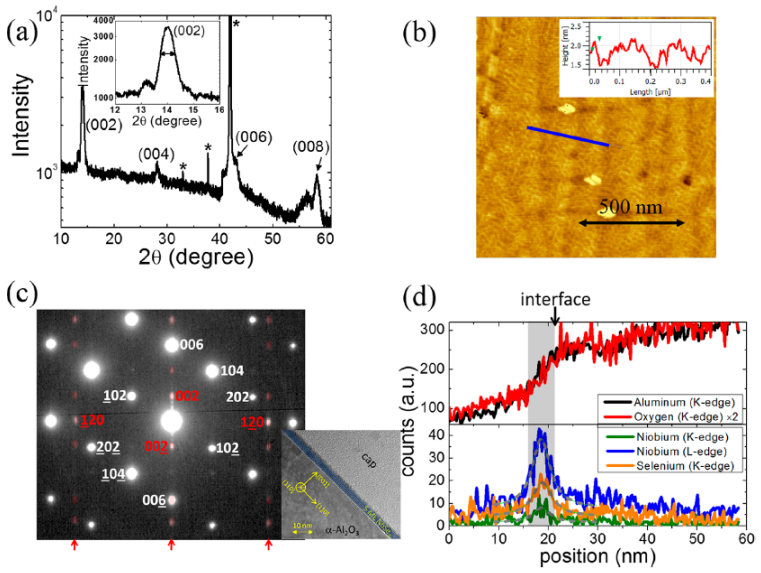

Figure 6.5: (a) X-ray diffraction of a $NbSe_2$ sample. The starred peaks correspond to the substrate and the background from the instrument. The inset provides a magnified image of the (002) peak which also shows signatures of thickness fringes. (b) AFM image of a continuous (island-free) 3 ML $NbSe_2$ sample. The visible substrate terraces indicate good surface coverage. (c) TEM based selective area diffraction (SAD) data of the 5 ML $NbSe_2$ sample (inset). The substrate diffraction peaks are labeled in white and the $NbSe_2$ diffraction peaks are in red. The c-axis (002) diffraction of $NbSe_2$ is aligned with the c-axis (006) diffraction of sapphire. (d) Element-selective spatially resolved energy-dispersive X-ray spectroscopy (EDX) data of a line across the interface of the layer. The data shows no element segregation in the film and a clear interface with the substrate. The stoichiometric ratio between Nb and Se is determined to be 1:2. Reprinted with permission from reference [27], Copyright 2020 American Chemical Society.

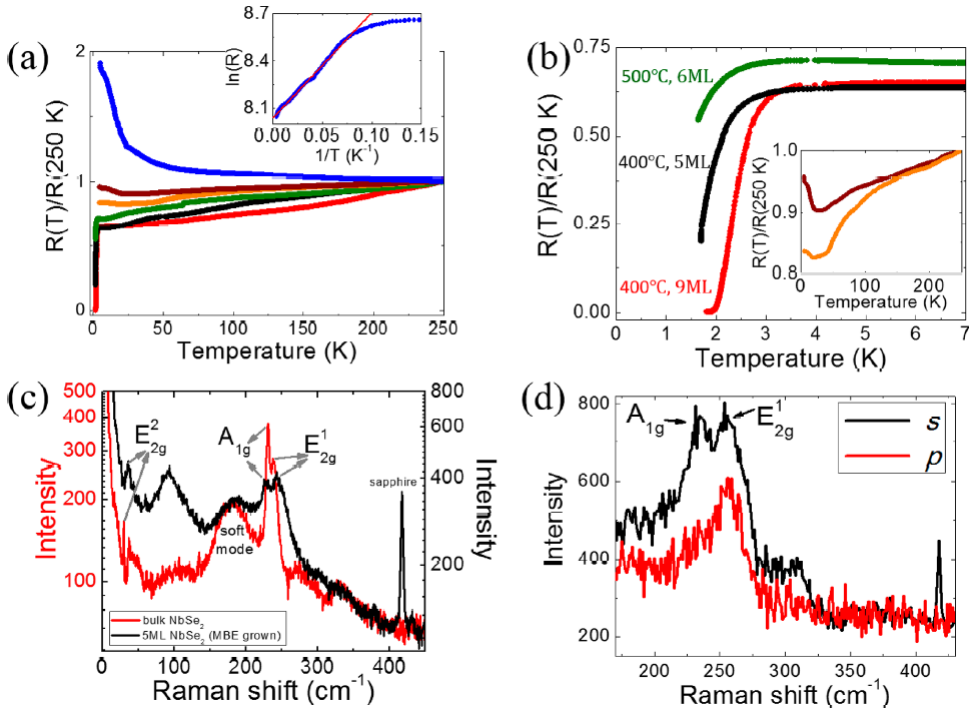

Figure 6.6: (a) Resistance measurements of the superconductor to insulator transition in NbSe2 samples systematically tuned by varying the growth temperature (from 400 to 600 °C). Inset: the ln(R) vs 1/T plot of the insulating sample. The linear fit works in the full temperature range from 13K and above, which gives an excitation gap $E/k_BT \approx 6.7K$. (b) Low-temperature zoomed-in plot of the superconducting samples. Inset: the metallic samples demonstrating low temperature insulating behavior. The color of each curve matches that of a. (c) Raman spectra comparison between MBE grown superconducting NbSe2 (black) and a bulk sample (red). (d) Polarized Raman spectroscopy identifying both the A_{1g} and E^1_{2g} Raman modes of the sample shown in the middle panel of Figure 6.7 (a). The A_{1g} is turned off when switching from s- to p-polarization, whereas the E^1_{2g} peak survives. Reprinted with permission from reference [27], Copyright 2020 American Chemical Society.

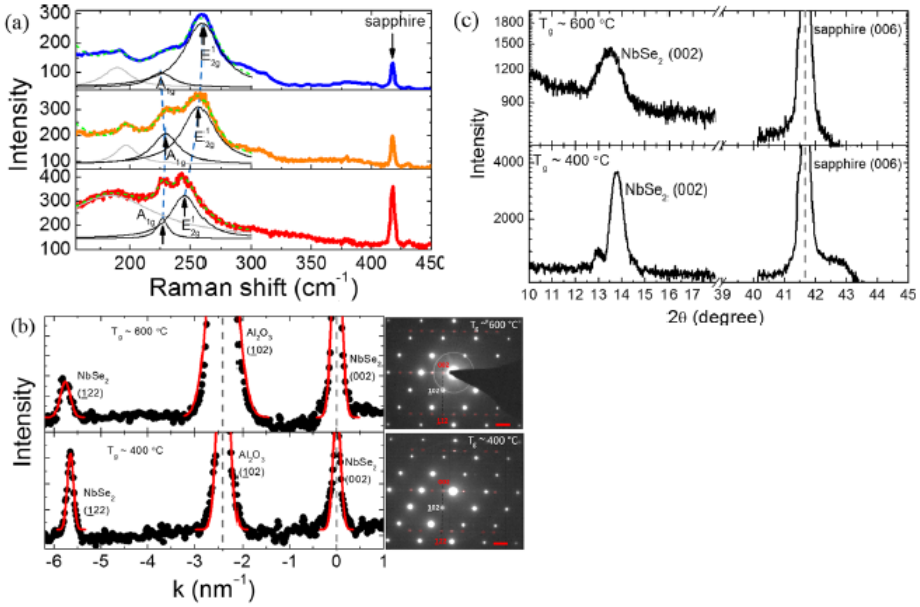

Figure 6.7: (a) Comparison of the Raman spectra among three samples having different electrical properties (insulating, superconducting and sample in between). The color of the data matches that in Figure 6.6 a. Gaussian fit (dashed line) is used to identify the locations of the E^1_{2g} and A_{1g} peaks. A red shift of the A_{1g} peak and a blue shift of the E^1_{2g} peak are observed, which accompanies the loss of superconductivity. (b) The comparison of the SAD results of two samples grown at $T_g \approx 600C^\circ$ (top, insulating) and at $T_g \approx 400C^\circ$ (bottom, superconducting), respectively. A line cut is made from the $NbSe_2$ SAD (002) peak to the $NbSe_2$ SAD (122) peak crossing the sapphire SAD (102) peak. The line cut is indicated by the dashed line shown in the TEM images (right). Gaussian fit is used to identify the locations of the diffraction peaks. By aligning the $NbSe_2$ (002) and sapphire (102) peaks (left), a clear shift of the $NbSe_2$ (122) peak is seen, indicating that the sample grown at $T_g \approx 600C^\circ$ has a slightly smaller lattice constant. (c) XRD results of two samples grown at $T_g \approx 600C^\circ$ (top) and at $T_g \approx 400C^\circ$ (bottom). The $NbSe_2$ (002) XRD peak shifts to lower angle for the sample grown at Tg ≈ 600 °C suggesting an expanded c-axis lattice constant. The comparison is based on the aligned sapphire (006) XRD peak. Reprinted with permission from reference [27], Copyright 2020 American Chemical Society.

Chapter 7

Conclusions and Future Work

Topological superconductivity and Majorana zero modes constitute some of the most exciting developments in condensed matter physics. Beside their obvious applications for quantum computing, the fundamental physics behind these materials, which ties in ideas from topology, make them interesting to study in their own right. This thesis explored the synthesis and characterization of materials for topological superconductivity. We would like to conclude this work with a brief summary of the salient results and provide some thoughts on future research and outlooks for the field.

The first path towards Majorana zero modes this thesis tackled utilized epitaxial Au (111) films proximitized by a base superconductor. We started from prior work done on this system and explored new upgrades to better it [169, 105]. We successfully demonstrated epitaxial growth of Au (111) on top of Nb (110) and the presence of superconductivity in the surface bands of the Au film. Furthermore, our results showcased evidence of the closing of the surface gap but persistence of bulk superconductivity. This is a necessary step towards

engineering a topological phase transition. The use of tellurium as a tunnel barrier also exhibited an enhancement of the g-factor to $g \approx 12$, a six-fold increase from the standard value of $g = 2$.

The second approach this thesis explored utilized $NbSe_2$, a member of the "new generation" of 2D materials. This layered material has been shown to superconduct down to the monolayer limit, and theoretically been predicted to host chiral Majorana edge modes once the material is pushed past the Pauli limit [173, 58, 60]. We demonstrated successful growth of the $NbSe_2$ films on c-plane sapphire and characterized the films with an array of tools. Our results show that temperature adjustments during MBE synthesis can drastically alter the transport properties of the films. Raman is used to identify in-plane strain as the most plausible culprit behind this change.

These results demonstrated that appropriate growth conditions and combination of materials can be used to engineer the necessary conditions for topological superconductivity. This is particularly important given that inherent topological superconductors are rare, and existing candidates are still under heavy debate [100, 142]. With this spirit in mind, we would like to discuss next steps for the work presented here.

In regards to the Au (111) system, there are several experiments in mind that should be completed. First, tunnel junctions using tellurium as the barrier should be fabricated in order to rule out effects of silver paste on the observed features in the conductance spectra. This would also provide further clarity into origin of the enhanced g-factor as possible magnetic impurities are not present in this type of device.

Secondly, differential conductance measurements need to be taken to confirm that the Au (111) surface band bottoms shift closer to the Fermi level after tellurium deposition. This shift is a result of the modification of the dielectric environment of the gold surface, and it is needed to enhance the size of the topological regions in the topological phase diagram [177]. Prior work cites tellurium to have a dielectric constant of $\epsilon \approx 30$ which is comparable to that of EuS so potential results from this experiment seem promising [16, 2].

Secondly, more effort must be put into device fabrication of planar tellurium nano-wires on top the Au surface. Theory has predicted that a topological gap can be opened in such a wire that results in localized Majorana zero modes [123, 177]. Tunneling measurements into the ends of the wire should reveal the presence of a zero bias peak [86]. This work would not be definitive proof of Majorana zero modes, rather it provides a necessary stepping stone to confirm that this approach is heading in the right direction. More conclusive evidence must be demonstrated through experiments such as electron teleportation [47]. This experiment would also further test the origin of the enhanced Landé g-factor. The current sentiment in this work is that its origin is a result of tellurium deposition, but whether this effect continues to persist when the tellurium layer is reduced to a quasi-1D nano-wire remains to be seen.

The $NbSe_2$ approach must also head down similar paths. We have shown that temperature plays a major role in determining the transport properties, and now efforts must be made to narrow down the conditions that enable large grain growth of films that superconduct [184, 183]. To the author's knowledge, there is still no reported evidence of MBE grown $NbSe_2$ on sapphire that superconducts to the same level as that reported in

exfoliated flakes [173]. Demonstrating such proof would be a major milestone as it showcases scalable synthesis of a possible topological superconductor. In addition, combining these films with other layered materials would provide a fertile playground for all manner of quantum phenomena [96].

It would be an understatement to say that the pursuit of Majorana zero modes and topological superconductors is hard. In fact, recent experiment work has been retracted in response to controversy over the accuracy of the results [186, 45]. But, physicists and engineers should not despair. With every new breakthrough, no matter how small, we shrink the uncertainty in our knowledge and bolster the confidence in our approach, and our goal inches ever closer.

Bibliography

[1] The nobel prize in physics 2010.

[2] Tellurium (te) dielectric constants: Datasheet from landolt-börnstein - group iii condensed matter · volume 41c: "non-tetrahedrally bonded elements and binary compounds i" in springermaterials (https://doi.org/10.1007/10681727_1299). Copyright 1998 Springer-Verlag Berlin Heidelberg.

[3] Hiroki Ago, Satoru Fukamachi, Hiroko Endo, Pablo SolÃs-FernÃ¡ndez, Rozan Mohamad Yunus, Yuki Uchida, Vishal Panchal, Olga Kazakova, and Masaharu Tsuji. Visualization of grain structure and boundaries of polycrystalline graphene and two-dimensional materials by epitaxial growth of transition metal dichalcogenides. *ACS Nano*, 10(3):3233–3240, 2016. PMID: 26943750.

[4] S. M. Albrecht, E. B. Hansen, A. P. Higginbotham, F. Kuemmeth, T. S. Jespersen, J. Nygård, P. Krogstrup, J. Danon, K. Flensberg, and C. M. Marcus. Transport signatures of quasiparticle poisoning in a majorana island. *Phys. Rev. Lett.*, 118:137701, Mar 2017.

[5] Jason Alicea. Majorana fermions in a tunable semiconductor device. *Phys. Rev. B*, 81:125318, Mar 2010.

[6] Jason Alicea. New directions in the pursuit of majorana fermions in solid state systems. *Reports on Progress in Physics*, 75(7):076501, jun 2012.

[7] Jason Alicea, Yuval Oreg, Gil Refael, Felix von Oppen, and Matthew P. A. Fisher. Non-abelian statistics and topological quantum information processing in 1d wire networks. *Nature Physics*, 7(5):412–417, May 2011.

[8] Yoichi Ando and Liang Fu. Topological crystalline insulators and topological superconductors: From concepts to materials. *Annual Review of Condensed Matter Physics*, 6(1):361–381, 2015.

[9] Bernard van Heck Sebastian Rubbert Rafal Skolasinski Bas Nijholt Irfan Muhammad Tomas Orn Rosdahl Anton Akhmerov, Jay Sau. Online course on topology in condensed matter. `https://topocondmat.org/index.html`. Accessed: 2021-09-27, Topology in Toy Models, Majoranas I.

[10] Swati Arora and Y. K. Vijay. Electrical, structural and optical properties of tellurium thin films on silicon substrate. *AIP Conference Proceedings*, 1953(1):030083, 2018.

[11] Frank Arute, Kunal Arya, Ryan Babbush, Dave Bacon, Joseph C. Bardin, Rami Barends, Rupak Biswas, Sergio Boixo, Fernando G. S. L. Brandao, David A. Buell, Brian Burkett, Yu Chen, Zijun Chen, Ben Chiaro, Roberto Collins, William Courtney, Andrew Dunsworth, Edward Farhi, Brooks Foxen, Austin Fowler, Craig Gidney, Marissa Giustina, Rob Graff, Keith Guerin, Steve Habegger, Matthew P. Harrigan, Michael J. Hartmann, Alan Ho, Markus Hoffmann, Trent Huang, Travis S. Humble, Sergei V. Isakov, Evan Jeffrey, Zhang Jiang, Dvir Kafri, Kostyantyn Kechedzhi, Julian Kelly, Paul V. Klimov, Sergey Knysh, Alexander Korotkov, Fedor Kostritsa, David Landhuis, Mike Lindmark, Erik Lucero, Dmitry Lyakh, Salvatore Mandrà, Jarrod R. McClean, Matthew McEwen, Anthony Megrant, Xiao Mi, Kristel Michielsen, Masoud Mohseni, Josh Mutus, Ofer Naaman, Matthew Neeley, Charles Neill, Murphy Yuezhen Niu, Eric Ostby, Andre Petukhov, John C. Platt, Chris Quintana, Eleanor G. Rieffel, Pedram Roushan, Nicholas C. Rubin, Daniel Sank, Kevin J. Satzinger, Vadim Smelyanskiy, Kevin J. Sung, Matthew D. Trevithick, Amit Vainsencher, Benjamin Villalonga, Theodore White, Z. Jamie Yao, Ping Yeh, Adam Zalcman, Hartmut Neven, and John M. Martinis. Quantum supremacy using a programmable superconducting processor. *Nature*, 574(7779):505–510, Oct 2019.

[12] Tomoya Asaba, Yongjie Wang, Gang Li, Ziji Xiang, Colin Tinsman, Lu Chen, Shangnan Zhou, Songrui Zhao, David Laleyan, Yi Li, Zetian Mi, and Lu Li. Magnetic field enhanced superconductivity in epitaxial thin film wte2. *Scientific Reports*, 8(1):6520, Apr 2018.

[13] Neil W. Ashcroft and N. David Mermin. *Solid State Physics*. Brooks/Cole, 1976.

[14] E. Aytan, B. Debnath, F. Kargar, Y. Barlas, M. M. Lacerda, J. X. Li, R. K. Lake, J. Shi, and A. A. Balandin. Spin-phonon coupling in antiferromagnetic nickel oxide. *Applied Physics Letters*, 111(25):252402, 2017.

[15] Alexander A. Balandin, Suchismita Ghosh, Wenzhong Bao, Irene Calizo, Desalegne Teweldebrhan, Feng Miao, and Chun Ning Lau. Superior thermal conductivity of single-layer graphene. *Nano Letters*, 8(3):902–907, 2008. PMID: 18284217.

[16] T. Balasubramaniam, Sa K. Narayandass, and D. Mangalaraj. Electrical properties of thermally evaporated tellurium thin films. *Bulletin of Materials Science*, 20(1):79–92, Feb 1997.

[17] Abhishek Banerjee, Ananthesh Sundaresh, Rajamanickam Ganesan, and P. S. Anil Kumar. Signatures of topological superconductivity in bulk-insulating topological insulator bisbte1.25se1.75 in proximity with superconducting nbse2. *ACS Nano*, 12(12):12665–12672, 2018.

[18] J. Bardeen, L. N. Cooper, and J. R. Schrieffer. Theory of superconductivity. *Phys. Rev.*, 108:1175–1204, Dec 1957.

[19] D. Beckmann, F. HÃ$\frac{1}{4}$bler, M. J. Wolf, and H. v. LÃ¶hneysen. Andreev bound states at spin-active interfaces. *Philosophical Transactions of the Royal Society A: Mathematical, Physical and Engineering Sciences*, 376(2125):20150002, 2018.

[20] Aron J. Beekman, Louk Rademaker, and Jasper van Wezel. An Introduction to Spontaneous Symmetry Breaking. *SciPost Phys. Lect. Notes*, page 11, 2019.

[21] G. E. Blonder, M. Tinkham, and T. M. Klapwijk. Transition from metallic to tunneling regimes in superconducting microconstrictions: Excess current, charge imbalance, and supercurrent conversion. *Phys. Rev. B*, 25:4515–4532, Apr 1982.

[22] N. N. Bogoljubov. On a new method in the theory of superconductivity. *Il Nuovo Cimento (1955-1965)*, 7(6):794–805, Mar 1958.

[23] C.J. Burroughs and C.A. Hamilton. Voltage calibration systems using josephson junction arrays. *IEEE Transactions on Instrumentation and Measurement*, 39(6):972–975, 1990.

[24] Yuan Cao, Valla Fatemi, Shiang Fang, Kenji Watanabe, Takashi Taniguchi, Efthimios Kaxiras, and Pablo Jarillo-Herrero. Unconventional superconductivity in magic-angle graphene superlattices. *Nature*, 556(7699):43–50, Apr 2018.

[25] Stephen Carr, Daniel Massatt, Shiang Fang, Paul Cazeaux, Mitchell Luskin, and Efthimios Kaxiras. Twistronics: Manipulating the electronic properties of two-dimensional layered structures through their twist angle. *Phys. Rev. B*, 95:075420, Feb 2017.

[26] Davide Castelvecchi. Ibm's quantum cloud computer goes commercial. *Nature*, 543(7644):159–159, Mar 2017.

[27] Cliff Chen, Protik Das, Ece Aytan, Weimin Zhou, Justin Horowitz, Biswarup Satpati, Alexander A. Balandin, Roger K. Lake, and Peng Wei. Strain-controlled superconductivity in few-layer nbse2. *ACS Applied Materials & Interfaces*, 12(34):38744–38750, 2020. PMID: 32805977.

[28] D Daghero and R S Gonnelli. Probing multiband superconductivity by point-contact spectroscopy. *Superconductor Science and Technology*, 23(4):043001, mar 2010.

[29] D Daghero, M Tortello, G A Ummarino, and R S Gonnelli. Directional point-contact andreev-reflection spectroscopy of fe-based superconductors: Fermi surface topology, gap symmetry, and electron–boson interaction. 74(12):124509, nov 2011.

[30] Wenqing Dai, Anthony Richardella, Renzhong Du, Weiwei Zhao, Xin Liu, C. X. Liu, Song-Hsun Huang, Raman Sankar, Fangcheng Chou, Nitin Samarth, and Qi Li. Proximity-effect-induced superconducting gap in topological surface states – a point contact spectroscopy study of nbse2/bi2se3 superconductor-topological insulator heterostructures. *Scientific Reports*, 7(1):7631, Aug 2017.

[31] Matthieu C. Dartiailh, Joseph J. Cuozzo, Bassel H. Elfeky, William Mayer, Joseph Yuan, Kaushini S. Wickramasinghe, Enrico Rossi, and Javad Shabani. Missing shapiro steps in topologically trivial josephson junction on inas quantum well. *Nature Communications*, 12(1):78, Jan 2021.

[32] Anindya Das, Yuval Ronen, Yonatan Most, Yuval Oreg, Moty Heiblum, and Hadas Shtrikman. Zero-bias peaks and splitting in an al–inas nanowire topological superconductor as a signature of majorana fermions. *Nature Physics*, 8(12):887–895, Dec 2012.

[33] Supriyo Datta. *Electron Transport in Mesoscopic Systems*. Cambridge University Press, June 2013.

[34] P.G. de Gennes. *Superconductivity of Metals and Alloys*. CRC Press, 1999.

[35] M. T. Deng, S. Vaitiekenas, E. B. Hansen, J. Danon, M. Leijnse, K. Flensberg, J. Nygard, P. Krogstrup, and C. M. Marcus. Majorana bound state in a coupled quantum-dot hybrid-nanowire system. *Science*, 354(6319):1557–1562, 2016.

[36] Nima Djavid, Gen Yin, Yafis Barlas, and Roger K. Lake. Gate controlled majorana zero modes of a two-dimensional topological superconductor. *Applied Physics Letters*, 113(1):012601, 2018.

[37] Fernando Domínguez, Fabian Hassler, and Gloria Platero. Dynamical detection of majorana fermions in current-biased nanowires. *Phys. Rev. B*, 86:140503, Oct 2012.

[38] G. Dresselhaus. Spin-orbit coupling effects in zinc blende structures. *Phys. Rev.*, 100:580–586, Oct 1955.

[39] D. Drung, C. Abmann, J. Beyer, A. Kirste, M. Peters, F. Ruede, and Th. Schurig. Highly sensitive and easy-to-use squid sensors. *IEEE Transactions on Applied Superconductivity*, 17(2):699–704, 2007.

[40] Steven R. Elliott and Marcel Franz. Colloquium: Majorana fermions in nuclear, particle, and solid-state physics. *Rev. Mod. Phys.*, 87:137–163, Feb 2015.

[41] Peter J. Eng, Thomas P. Trainor, Gordon E. Brown Jr., Glenn A. Waychunas, Matthew Newville, Stephen R. Sutton, and Mark L. Rivers. Structure of the hydrated α-al¡sub¿2¡/sub¿o¡sub¿3¡/sub¿ (0001) surface. *Science*, 288(5468):1029–1033, 2000.

[42] A. D. K. Finck, D. J. Van Harlingen, P. K. Mohseni, K. , and X. Li. Anomalous modulation of a zero-bias peak in a hybrid nanowire-superconductor device. *Phys. Rev. Lett.*, 110:126406, Mar 2013.

[43] S. Foner and E.J. McNiff. Upper critical fields of layered superconducting nbse2 at low temperature. *Physics Letters A*, 45(6):429–430, 1973.

[44] Austin G. Fowler, Matteo Mariantoni, John M. Martinis, and Andrew N. Cleland. Surface codes: Towards practical large-scale quantum computation. *Phys. Rev. A*, 86:032324, Sep 2012.

[45] Sergey Frolov. Quantum computing's reproducibility crisis. *Nature*, 592:350–352.

[46] F. N. M. Froning, M. J. Rančić, B. Hetényi, S. Bosco, M. K. Rehmann, A. Li, E. P. A. M. Bakkers, F. A. Zwanenburg, D. Loss, D. M. Zumbühl, and F. R. Braakman. Strong spin-orbit interaction and g-factor renormalization of hole spins in ge/si nanowire quantum dots. *Phys. Rev. Research*, 3:013081, Jan 2021.

[47] Liang Fu. Electron teleportation via majorana bound states in a mesoscopic superconductor. *Phys. Rev. Lett.*, 104:056402, Feb 2010.

[48] Yajun Fu, Erfu Liu, Hongtao Yuan, Peizhe Tang, Biao Lian, Gang Xu, Junwen Zeng, Zhuoyu Chen, Yaojia Wang, Wei Zhou, Kang Xu, Anyuan Gao, Chen Pan, Miao Wang, Baigeng Wang, Shou-Cheng Zhang, Yi Cui, Harold Y. Hwang, and Feng Miao. Gated tuned superconductivity and phonon softening in monolayer and bilayer mos2. *npj Quantum Materials*, 2(1):52, Sep 2017.

[49] Tetsuya Furukawa, Yuri Shimokawa, Kaya Kobayashi, and Tetsuaki Itou. Observation of current-induced bulk magnetization in elemental tellurium. *Nature Communications*, 8(1):954, Oct 2017.

[50] Paul A. Gabrys, Soyoung E. Seo, Mary X. Wang, EunBi Oh, Robert J. Macfarlane, and Chad A. Mirkin. Lattice mismatch in crystalline nanoparticle thin films. *Nano Letters*, 18(1):579–585, 2018. PMID: 29271207.

[51] M. A. Garcia, E. Fernandez Pinel, J. de la Venta, A. Quesada, V. Bouzas, J. F. Fernandez, J. J. Romero, M. S. MartÃn Gonzalez, and J. L. Costa-Kramer. Sources of experimental errors in the observation of nanoscale magnetism. *Journal of Applied Physics*, 105(1):013925, 2009.

[52] Sasa Gazibegovic, Diana Car, Hao Zhang, Stijn C. Balk, John A. Logan, Michiel W. A. de Moor, Maja C. Cassidy, Rudi Schmits, Di Xu, Guanzhong Wang, Peter Krogstrup, Roy L. M. Op het Veld, Kun Zuo, Yoram Vos, Jie Shen, Daniël Bouman, Borzoyeh Shojaei, Daniel Pennachio, Joon Sue Lee, Petrus J. van Veldhoven, Sebastian Koelling, Marcel A. Verheijen, Leo P. Kouwenhoven, Chris J. Palmstrøm, and Erik P. A. M. Bakkers. Epitaxy of advanced nanowire quantum devices. *Nature*, 548(7668):434–438, Aug 2017.

[53] A. K. Geim and K. S. Novoselov. The rise of graphene. *Nature Materials*, 6(3):183–191, Mar 2007.

[54] V. B. Geshkenbein, A. I. Larkin, and A. Barone. Vortices with half magnetic flux quanta in "heavy-fermion" superconductors. *Phys. Rev. B*, 36:235–238, Jul 1987.

[55] Theresa P. Ginley, Yong Wang, and Stephanie Law. Topological insulator film growth by molecular beam epitaxy: A review. *Crystals*, 6(11), 2016.

[56] R. S. Gonnelli, D. Daghero, G. A. Ummarino, V. A. Stepanov, J. Jun, S. M. Kazakov, and J. Karpinski. Direct evidence for two-band superconductivity in mgb_2 single crystals from directional point-contact spectroscopy in magnetic fields. *Phys. Rev. Lett.*, 89:247004, Nov 2002.

[57] M. Z. Hasan and C. L. Kane. Colloquium: Topological insulators. *Rev. Mod. Phys.*, 82:3045–3067, Nov 2010.

[58] Wen-Yu He, Benjamin T. Zhou, James J. He, Noah F. Q. Yuan, Ting Zhang, and K. T. Law. Magnetic field driven nodal topological superconductivity in monolayer transition metal dichalcogenides. *Communications Physics*, 1(1):40, Jul 2018.

[59] Ricardo Heras. Dirac quantisation condition: a comprehensive review. *Contemporary Physics*, 59(4):331–355, Oct 2018.

[60] Yi-Ting Hsu, Abolhassan Vaezi, Mark H. Fischer, and Eun-Ah Kim. Topological superconductivity in monolayer transition metal dichalcogenides. *Nature Communications*, 8(1):14985, Apr 2017.

[61] Yeung Yu Hui, Xiaofei Liu, Wenjing Jie, Ngai Yui Chan, Jianhua Hao, Yu-Te Hsu, Lain-Jong Li, Wanlin Guo, and Shu Ping Lau. Exceptional tunability of band energy in a compressively strained trilayer mos2 sheet. *ACS Nano*, 7(8):7126–7131, 2013. PMID: 23844893.

[62] Colin Humphreys. Controlling crystal growth. *Nature*, 341(6244):689–689, Oct 1989.

[63] Fengrui Jiang, Weiquan Cai, and Guolong Tan. Facile synthesis and optical properties of small selenium nanocrystals and nanorods. *Nanoscale Research Letters*, 12(1):401, Jun 2017.

[64] Liang Jiang, David Pekker, Jason Alicea, Gil Refael, Yuval Oreg, and Felix von Oppen. Unconventional josephson signatures of majorana bound states. *Phys. Rev. Lett.*, 107:236401, Nov 2011.

[65] B A Joyce. Molecular beam epitaxy. *Reports on Progress in Physics*, 48(12):1637–1697, dec 1985.

[66] H.-G. Junginger. Electronic band structure of tellurium. *Solid State Communications*, 5(7):509–511, 1967.

[67] Charles L. Kane. An insulator with a twist. *Nature Physics*, 4(5):348–349, May 2008.

[68] Mehran Kardar. *Statistical Physics of Fields*. Cambridge University Press, 2007.

[69] Torsten Karzig, William S. Cole, and Dmitry I. Pikulin. Quasiparticle poisoning of majorana qubits. *Phys. Rev. Lett.*, 126:057702, Feb 2021.

[70] Shawulienu Kezilebieke, Md Nurul Huda, Viliam Vaňo, Markus Aapro, Somesh C. Ganguli, Orlando J. Silveira, Szczepan Głodzik, Adam S. Foster, Teemu Ojanen, and Peter Liljeroth. Topological superconductivity in a van der waals heterostructure. *Nature*, 588(7838):424–428, Dec 2020.

[71] A Yu Kitaev. Unpaired majorana fermions in quantum wires. *Physics-Uspekhi*, 44(10S):131–136, oct 2001.

[72] A.Yu. Kitaev. Fault-tolerant quantum computation by anyons. *Annals of Physics*, 303(1):2–30, 2003.

[73] Charles Kittel. *Introduction to Solid State Physics*. John Wiley & Sons, 8 edition, 2005.

[74] R. A. Klemm, A. Luther, and M. R. Beasley. Theory of the upper critical field in layered superconductors. *Phys. Rev. B*, 12:877–891, Aug 1975.

[75] Christoph Kloeffel, Mircea Trif, and Daniel Loss. Strong spin-orbit interaction and helical hole states in ge/si nanowires. *Phys. Rev. B*, 84:195314, Nov 2011.

[76] Jens Koch, Terri M. Yu, Jay Gambetta, A. A. Houck, D. I. Schuster, J. Majer, Alexandre Blais, M. H. Devoret, S. M. Girvin, and R. J. Schoelkopf. Charge-insensitive qubit design derived from the cooper pair box. *Phys. Rev. A*, 76:042319, Oct 2007.

[77] Atsushi Koma, Kazumasa Sunouchi, and Takao Miyajima. Fabrication and characterization of heterostructures with subnanometer thickness. *Microelectronic Engineering*, 2(1):129–136, 1984. Special Issue on Nanometer Structure Electronics.

[78] Markus Konig, Steffen Wiedmann, Christoph BrÃ$\frac{1}{4}$ne, Andreas Roth, Hartmut Buhmann, Laurens W. Molenkamp, Xiao-Liang Qi, and Shou-Cheng Zhang. Quantum spin hall insulator state in hgte quantum wells. *Science*, 318(5851):766–770, 2007.

[79] N.B. Kopnin. *Introduction to the Theory of Superconductivity*, September 2009. (Lecture Notes).

[80] P. Krogstrup, N. L. B. Ziino, W. Chang, S. M. Albrecht, M. H. Madsen, E. Johnson, J. Nygård, C. Â M. Marcus, and T. S. Jespersen. Epitaxy of semiconductor–superconductor nanowires. *Nature Materials*, 14(4):400–406, Apr 2015.

[81] Z. D. Kvon, E. B. Olshanetsky, N. N. Mikhailov, and D. A. Kozlov. Two-dimensional electron systems in hgte quantum wells. *Low Temperature Physics*, 35(1):6–14, 2009.

[82] H.-J. Kwon, K. Sengupta, and V. M. Yakovenko. Fractional ac josephson effect in p- and d-wave superconductors. *The European Physical Journal B - Condensed Matter and Complex Systems*, 37(3):349–361, Feb 2004.

[83] Jason Lapano, Lauren Nuckols, Alessandro R. Mazza, Yun-Yi Pai, Jie Zhang, Ben Lawrie, Rob G. Moore, Gyula Eres, Ho Nyung Lee, Mao-Hua Du, T. Zac Ward, Joon Sue Lee, William J. Weber, Yanwen Zhang, and Matthew Brahlek. Adsorption-controlled growth of $MnTe(Bi_2Te_3)_n$ by molecular beam epitaxy exhibiting stoichiometry-controlled magnetism. *Phys. Rev. Materials*, 4:111201, Nov 2020.

[84] Dominique Laroche, Daniël Bouman, David J. van Woerkom, Alex Proutski, Chaitanya Murthy, Dmitry I. Pikulin, Chetan Nayak, Ruben J. J. van Gulik, Jesper

Nygård, Peter Krogstrup, Leo P. Kouwenhoven, and Attila Geresdi. Observation of the 4π-periodic josephson effect in indium arsenide nanowires. *Nature Communications*, 10(1):245, Jan 2019.

[85] S. LaShell, B. A. McDougall, and E. Jensen. Spin splitting of an au(111) surface state band observed with angle resolved photoelectron spectroscopy. *Phys. Rev. Lett.*, 77:3419–3422, Oct 1996.

[86] K. T. Law, Patrick A. Lee, and T. K. Ng. Majorana fermion induced resonant andreev reflection. *Phys. Rev. Lett.*, 103:237001, Dec 2009.

[87] Changgu Lee, Xiaoding Wei, Jeffrey W. Kysar, and James Hone. Measurement of the elastic properties and intrinsic strength of monolayer graphene. *Science*, 321(5887):385–388, 2008.

[88] Martin Leijnse and Karsten Flensberg. Introduction to topological superconductivity and majorana fermions. *Semiconductor Science and Technology*, 27(12):124003, nov 2012.

[89] Ming-Yang Li, Chang-Hsiao Chen, Yumeng Shi, and Lain-Jong Li. Heterostructures based on two-dimensional layered materials and their potential applications. *Materials Today*, 19(6):322–335, 2016.

[90] Yufan Li, Xiaoying Xu, M.-H. Lee, M.-W. Chu, and C. L. Chien. Observation of half-quantum flux in the unconventional superconductor β-Bi_2Pd. *Science*, 366(6462):238–241, 2019.

[91] Jacob Linder and Alexander V. Balatsky. Odd-frequency superconductivity. *Rev. Mod. Phys.*, 91:045005, Dec 2019.

[92] W. A. Little and R. D. Parks. Observation of quantum periodicity in the transition temperature of a superconducting cylinder. *Phys. Rev. Lett.*, 9:9–12, Jul 1962.

[93] Cheng-Wei Liu, Jin-Ji Dai, Ssu-Kuan Wu, Nhu-Quynh Diep, Sa-Hoang Huynh, Thi-Thu Mai, Hua-Chiang Wen, Chi-Tsu Yuan, Wu-Ching Chou, Ji-Lin Shen, and Huy-Hoang Luc. Substrate-induced strain in 2d layered gase materials grown by molecular beam epitaxy. *Scientific Reports*, 10(1):12972, Jul 2020.

[94] Chun-Xiao Liu, Jay D. Sau, Tudor D. Stanescu, and S. Das Sarma. Andreev bound states versus majorana bound states in quantum dot-nanowire-superconductor hybrid structures: Trivial versus topological zero-bias conductance peaks. *Phys. Rev. B*, 96:075161, Aug 2017.

[95] Jie Liu, Andrew C. Potter, K. T. Law, and Patrick A. Lee. Zero-bias peaks in the tunneling conductance of spin-orbit-coupled superconducting wires with and without majorana end-states. *Phys. Rev. Lett.*, 109:267002, Dec 2012.

[96] Yuan Liu, Nathan O. Weiss, Xidong Duan, Hung-Chieh Cheng, Yu Huang, and Xiangfeng Duan. Van der waals heterostructures and devices. *Nature Reviews Materials*, 1(9):16042, Jul 2016.

[97] J. M. Lu, O. Zheliuk, I. Leermakers, N. F. Q. Yuan, U. Zeitler, K. T. Law, and J. T. Ye. Evidence for two-dimensional ising superconductivity in gated mos¡sub¿2¡/sub¿. *Science*, 350(6266):1353–1357, 2015.

[98] R. M. Lutchyn, E. P. A. M. Bakkers, L. P. Kouwenhoven, P. Krogstrup, C. M. Marcus, and Y. Oreg. Majorana zero modes in superconductor–semiconductor heterostructures. *Nature Reviews Materials*, 3(5):52–68, May 2018.

[99] Roman M. Lutchyn, Jay D. Sau, and S. Das Sarma. Majorana fermions and a topological phase transition in semiconductor-superconductor heterostructures. *Phys. Rev. Lett.*, 105:077001, Aug 2010.

[100] A.P Mackenzie and Y Maeno. p-wave superconductivity. *Physica B: Condensed Matter*, 280(1):148–153, 2000.

[101] John E. Mahan, Kent M. Geib, G. Y. Robinson, and Robert G. Long. A review of the geometrical fundamentals of reflection high-energy electron diffraction with application to silicon surfaces. *Journal of Vacuum Science & Technology A*, 8(5):3692–3700, 1990.

[102] K. F. Mak, K. L. McGill, J. Park, and P. L. McEuen. The valley hall effect in mos¡sub¿2¡/sub¿ transistors. *Science*, 344(6191):1489–1492, 2014.

[103] Kin Fai Mak, Changgu Lee, James Hone, Jie Shan, and Tony F. Heinz. Atomically thin mos_2: A new direct-gap semiconductor. *Phys. Rev. Lett.*, 105:136805, Sep 2010.

[104] A. Manchon, H. C. Koo, J. Nitta, S. M. Frolov, and R. A. Duine. New perspectives for rashba spin–orbit coupling. *Nature Materials*, 14(9):871–882, Sep 2015.

[105] Sujit Manna, Peng Wei, Yingming Xie, Kam Tuen Law, Patrick A. Lee, and Jagadeesh S. Moodera. Signature of a pair of majorana zero modes in superconducting gold surface states. *Proceedings of the National Academy of Sciences*, 117(16):8775–8782, 2020.

[106] Sajedeh Manzeli, Dmitry Ovchinnikov, Diego Pasquier, Oleg V. Yazyev, and Andras Kis. 2d transition metal dichalcogenides. *Nature Reviews Materials*, 2(8):17033, Jun 2017.

[107] L. F. Mattheiss. Band structures of transition-metal-dichalcogenide layer compounds. *Phys. Rev. B*, 8:3719–3740, Oct 1973.

[108] Paul McClarty. Topological magnons: A review, 2021.

[109] W. Meissner and R. Ochsenfeld. Ein neuer effekt bei eintritt der supraleitfähigkeit. *Naturwissenschaften*, 21(44):787–788, Nov 1933.

[110] P. Monod and A. Janossy. Conduction electron spin resonance in gold. *Journal of Low Temperature Physics*, 26(1):311–316, Jan 1977.

[111] Christopher Moore, Tudor D. Stanescu, and Sumanta Tewari. Two-terminal charge tunneling: Disentangling majorana zero modes from partially separated andreev bound states in semiconductor-superconductor heterostructures. *Phys. Rev. B*, 97:165302, Apr 2018.

[112] N. F. Mott. Conduction in non-crystalline materials. *The Philosophical Magazine: A Journal of Theoretical Experimental and Applied Physics*, 19(160):835–852, 1969.

[113] V. Mourik, K. Zuo, S. M. Frolov, S. R. Plissard, E. P. A. M. Bakkers, and L. P. Kouwenhoven. Signatures of majorana fermions in hybrid superconductor-semiconductor nanowire devices. *Science*, 336(6084):1003–1007, 2012.

[114] Masaki Nakano, Yue Wang, Yuta Kashiwabara, Hideki Matsuoka, and Yoshihiro Iwasa. Layer-by-layer epitaxial growth of scalable wse2 on sapphire by molecular beam epitaxy. *Nano Letters*, 17(9):5595–5599, 2017. PMID: 28849935.

[115] Yuki Nakata, Katsuaki Sugawara, Ryota Shimizu, Yoshinori Okada, Patrick Han, Taro Hitosugi, Keiji Ueno, Takafumi Sato, and Takashi Takahashi. Monolayer 1t-nbse2 as a mott insulator. *NPG Asia Materials*, 8(11):e321–e321, Nov 2016.

[116] M. Nielsen and I. Chuang. *Quantum Computation and Quantum Information*. Cambridge University Press, 10 edition, 2010.

[117] Branislav Nikolić and Philip B. Allen. Electron transport through a circular constriction. *Phys. Rev. B*, 60:3963–3969, Aug 1999.

[118] K. S. Novoselov, V. I. Falko, L. Colombo, P. R. Gellert, M. G. Schwab, and K. Kim. A roadmap for graphene. *Nature*, 490(7419):192–200, Oct 2012.

[119] K. S. Novoselov, A. K. Geim, S. V. Morozov, D. Jiang, Y. Zhang, S. V. Dubonos, I. V. Grigorieva, and A. A. Firsov. Electric field effect in atomically thin carbon films. *Science*, 306(5696):666–669, 2004.

[120] Sang Ho Oh, Christina Scheu, Thomas Wagner, and Manfred RÃ$\frac{1}{4}$hle. Control of bonding and epitaxy at copper/sapphire interface. *Applied Physics Letters*, 91(14):141912, 2007.

[121] Roy L. M. Op het Veld, Di Xu, Vanessa Schaller, Marcel A. Verheijen, Stan M. E. Peters, Jason Jung, Chuyao Tong, Qingzhen Wang, Michiel W. A. de Moor, Bart Hesselmann, Kiefer Vermeulen, Jouri D. S. Bommer, Joon Sue Lee, Andrey Sarikov, Mihir Pendharkar, Anna Marzegalli, Sebastian Koelling, Leo P. Kouwenhoven, Leo Miglio, Chris J. Palmstrøm, Hao Zhang, and Erik P. A. M. Bakkers. In-plane selective area insb–al nanowire quantum networks. *Communications Physics*, 3(1):59, Mar 2020.

[122] Yuval Oreg, Gil Refael, and Felix von Oppen. Helical liquids and majorana bound states in quantum wires. *Phys. Rev. Lett.*, 105:177002, Oct 2010.

[123] Michał Papaj and Liang Fu. Creating majorana modes from segmented fermi surface. *Nature Communications*, 12(1):577, Jan 2021.

[124] Pradnya Parab, Deepak Singh, Santosh Haram, R. P. Singh, and Sangita Bose. Point contact andreev reflection studies of a non-centro symmetric superconductor re6zr. *Scientific Reports*, 9(1):2498, Feb 2019.

[125] Jihwey Park, Yeong-Ah Soh, Gabriel Aeppli, Xiao Feng, Yunbo Ou, Ke He, and Qi-Kun Xue. Crystallinity of tellurium capping and epitaxy of ferromagnetic topological insulator films on srtio3. *Scientific Reports*, 5(1):11595, Jun 2015.

[126] C M Pereira and W Y Liang. Raman studies of the normal phase of 2h-NbSe2. 15(27):L991–L995, sep 1982.

[127] J. M. Pino, J. M. Dreiling, C. Figgatt, J. P. Gaebler, S. A. Moses, M. S. Allman, C. H. Baldwin, M. Foss-Feig, D. Hayes, K. Mayer, C. Ryan-Anderson, and B. Neyenhuis. Demonstration of the trapped-ion quantum ccd computer architecture. *Nature*, 592(7853):209–213, Apr 2021.

[128] A. Plecenník, M. Grajcar, Š. Beňačka, P. Seidel, and A. Pfuch. Finite-quasiparticle-lifetime effects in the differential conductance of $bi_2sr_2cacu_2o_y$/au junctions. *Phys. Rev. B*, 49:10016–10019, Apr 1994.

[129] Andrew C. Potter and Patrick A. Lee. Multichannel generalization of kitaev's majorana end states and a practical route to realize them in thin films. *Phys. Rev. Lett.*, 105:227003, Nov 2010.

[130] Andrew C. Potter and Patrick A. Lee. Topological superconductivity and majorana fermions in metallic surface states. *Phys. Rev. B*, 85:094516, Mar 2012.

[131] J. Preskill. *Lecture Notes for Ph219/CS219*, July 2015. (Lecture Notes).

[132] Xiao-Liang Qi and Shou-Cheng Zhang. Topological insulators and superconductors. *Rev. Mod. Phys.*, 83:1057–1110, Oct 2011.

[133] Xiaofeng Qian, Junwei Liu, Liang Fu, and Ju Li. Quantum spin hall effect in two-dimensional transition metal dichalcogenides. *Science*, 346(6215):1344–1347, 2014.

[134] N. Read and Dmitry Green. Paired states of fermions in two dimensions with breaking of parity and time-reversal symmetries and the fractional quantum hall effect. *Phys. Rev. B*, 61:10267–10297, Apr 2000.

[135] Leonid P. Rokhinson, Xinyu Liu, and Jacek K. Furdyna. The fractional a.c. josephson effect in a semiconductor–superconductor nanowire as a signature of majorana particles. *Nature Physics*, 8(11):795–799, Nov 2012.

[136] Laura M. Roth, Benjamin Lax, and Solomon Zwerdling. Theory of optical magneto-absorption effects in semiconductors. *Phys. Rev.*, 114:90–104, Apr 1959.

[137] Yu Saito, Yasuharu Nakamura, Mohammad Saeed Bahramy, Yoshimitsu Kohama, Jianting Ye, Yuichi Kasahara, Yuji Nakagawa, Masaru Onga, Masashi Tokunaga, Tsutomu Nojima, Youichi Yanase, and Yoshihiro Iwasa. Superconductivity protected by spin–valley locking in ion-gated mos2. *Nature Physics*, 12(2):144–149, Feb 2016.

[138] Yu Saito, Tsutomu Nojima, and Yoshihiro Iwasa. Highly crystalline 2d superconductors. *Nature Reviews Materials*, 2(1):16094, Dec 2016.

[139] G. Salis, Y. Kato, K. Ensslin, D. C. Driscoll, A. C. Gossard, and D. D. Awschalom. Electrical control of spin coherence in semiconductor nanostructures. *Nature*, 414(6864):619–622, Dec 2001.

[140] R. Samnakay, D. Wickramaratne, T. R. Pope, R. K. Lake, T. T. Salguero, and A. A. Balandin. Zone-folded phonons and the commensurate-incommensurate charge-density-wave transition in 1t-tase2 thin films. *Nano Letters*, 15(5):2965–2973, 2015. PMID: 25927475.

[141] Sankar Das Sarma, Michael Freedman, and Chetan Nayak. Majorana zero modes and topological quantum computation. *npj Quantum Information*, 1(1):15001, Oct 2015.

[142] Masatoshi Sato and Yoichi Ando. Topological superconductors: a review. 80(7):076501, may 2017.

[143] John R. Schaibley, Hongyi Yu, Genevieve Clark, Pasqual Rivera, Jason S. Ross, Kyle L. Seyler, Wang Yao, and Xiaodong Xu. Valleytronics in 2d materials. *Nature Reviews Materials*, 1(11):16055, Aug 2016.

[144] F. Schedin, A. K. Geim, S. V. Morozov, E. W. Hill, P. Blake, M. I. Katsnelson, and K. S. Novoselov. Detection of individual gas molecules adsorbed on graphene. *Nature Materials*, 6(9):652–655, Sep 2007.

[145] Nicholas Sedlmayr, Vardan Kaladzhyan, Clément Dutreix, and Cristina Bena. Bulk boundary correspondence and the existence of majorana bound states on the edges of 2d topological superconductors. *Phys. Rev. B*, 96:184516, Nov 2017.

[146] Daniel Shaffer, Jian Kang, F. J. Burnell, and Rafael M. Fernandes. Crystalline nodal topological superconductivity and bogolyubov fermi surfaces in monolayer $nbse_2$. *Phys. Rev. B*, 101:224503, Jun 2020.

[147] Sidney Shapiro. Josephson currents in superconducting tunneling: The effect of microwaves and other observations. *Phys. Rev. Lett.*, 11:80–82, Jul 1963.

[148] Girish Sharma and Sumanta Tewari. Yu-shiba-rusinov states and topological superconductivity in ising paired superconductors. *Phys. Rev. B*, 94:094515, Sep 2016.

[149] Yu. V. Sharvin. A possible method for studying fermi surfaces. *Soviet Physics JETP*, 21:655, March 1965.

[150] Wu Shi, Jianting Ye, Yijin Zhang, Ryuji Suzuki, Masaro Yoshida, Jun Miyazaki, Naoko Inoue, Yu Saito, and Yoshihiro Iwasa. Superconductivity series in transition metal dichalcogenides by ionic gating. *Scientific Reports*, 5(1):12534, Aug 2015.

[151] Peter W. Shor. Scheme for reducing decoherence in quantum computer memory. *Phys. Rev. A*, 52:R2493–R2496, Oct 1995.

[152] Manfred Sigrist. *Introduction Unconventional Superconductivity.* (Lecture Notes).

[153] Manfred Sigrist and Kazuo Ueda. Phenomenological theory of unconventional superconductivity. *Rev. Mod. Phys.*, 63:239–311, Apr 1991.

[154] David S Simon. Topology and physics: a historical overview. In *Tying Light in Knots*, 2053-2571, pages 1–1 to 1–7. Morgan & Claypool Publishers, 2018.

[155] M. J. Snelling, G. P. Flinn, A. S. Plaut, R. T. Harley, A. C. Tropper, R. Eccleston, and C. C. Phillips. Magnetic g factor of electrons in gaas/al$_x$ga$_{1-x}$as quantum wells. *Phys. Rev. B*, 44:11345–11352, Nov 1991.

[156] Philip F. Bagwell Supriyo Datta and M.P. Anantram. Scattering theory of transport for mesoscopic superconductors. Technical Report 107, Purdue University, January 1996.

[157] Carsten Timm. *Theory of Superconductivity*, February 2016. (Lecture Notes).

[158] Michael Tinkham. *Introduction to Superconductivity.* McGraw-Hill, Inc., 2 edition, 1996.

[159] Polychronis Tsipas, Evangelia Xenogiannopoulou, Spyridon Kassavetis, Dimitra Tsoutsou, Evangelos Golias, Calliope Bazioti, George P. Dimitrakopulos, Philomela Komninou, Hu Liang, Matty Caymax, and Athanasios Dimoulas. Observation of surface dirac cone in high-quality ultrathin epitaxial bi2se3 topological insulator on aln(0001) dielectric. *ACS Nano*, 8(7):6614–6619, 2014. PMID: 24915126.

[160] C. C. Tsuei and J. R. Kirtley. Pairing symmetry in cuprate superconductors. *Rev. Mod. Phys.*, 72:969–1016, Oct 2000.

[161] Miguel M. Ugeda, Aaron J. Bradley, Yi Zhang, Seita Onishi, Yi Chen, Wei Ruan, Claudia Ojeda-Aristizabal, Hyejin Ryu, Mark T. Edmonds, Hsin-Zon Tsai, Alexander Riss, Sung-Kwan Mo, Dunghai Lee, Alex Zettl, Zahid Hussain, Zhi-Xun Shen, and Michael F. Crommie. Characterization of collective ground states in single-layer nbse2. *Nature Physics*, 12(1):92–97, Jan 2016.

[162] S. Vaitiekenas, G. W. Winkler, B. van Heck, T. Karzig, M.-T. Deng, K. Flensberg, L. I. Glazman, C. Nayak, P. Krogstrup, R. M. Lutchyn, and C. M. Marcus. Flux-induced topological superconductivity in full-shell nanowires. *Science*, 367(6485):eaav3392, 2020.

[163] Dirk van Delft and Peter Kes. The discovery of superconductivity. *Physics Today*, 63(9):38–43, 2010.

[164] Sagar Vijay and Liang Fu. Teleportation-based quantum information processing with majorana zero modes. *Phys. Rev. B*, 94:235446, Dec 2016.

[165] Lee A. Walsh, Rafik Addou, Robert M. Wallace, and Christopher L. Hinkle. Chapter 22 - molecular beam epitaxy of transition metal dichalcogenides. In Mohamed Henini, editor, *Molecular Beam Epitaxy (Second Edition)*, pages 515–531. Elsevier, second edition edition, 2018.

[166] Gang Wang, Alexey Chernikov, Mikhail M. Glazov, Tony F. Heinz, Xavier Marie, Thierry Amand, and Bernhard Urbaszek. Colloquium: Excitons in atomically thin transition metal dichalcogenides. *Rev. Mod. Phys.*, 90:021001, Apr 2018.

[167] R. C. C. Ward, E. J. Grier, and A. K. Petford-Long. Mbe growth of (1 1 0) refractory metals on a-plane sapphire. *Journal of Materials Science: Materials in Electronics*, 14(9):533–539, Sep 2003.

[168] Peng Wei, Ferhat Katmis, Cui-Zu Chang, and Jagadeesh S. Moodera. Induced superconductivity and engineered josephson tunneling devices in epitaxial (111)-oriented gold/vanadium heterostructures. *Nano Letters*, 16(4):2714–2719, 2016. PMID: 26943807.

[169] Peng Wei, Sujit Manna, Marius Eich, Patrick Lee, and Jagadeesh Moodera. Superconductivity in the surface state of noble metal gold and its fermi level tuning by eus dielectric. *Phys. Rev. Lett.*, 122:247002, Jun 2019.

[170] Fabian Wenger and Stellan Östlund. d-wave pairing in tetragonal superconductors. *Phys. Rev. B*, 47:5977–5983, Mar 1993.

[171] A. M. Whiticar, A. Fornieri, E. C. T. O'Farrell, A. C. C. Drachmann, T. Wang, C. Thomas, S. Gronin, R. Kallaher, G. C. Gardner, M. J. Manfra, C. M. Marcus, and F. Nichele. Coherent transport through a majorana island in an aharonov–bohm interferometer. *Nature Communications*, 11(1):3212, Jun 2020.

[172] A.R. Wildes, J. Mayer, and K. Theis-BrÃ¶hl. The growth and structure of epitaxial niobium on sapphire. *Thin Solid Films*, 401(1):7–34, 2001.

[173] Xiaoxiang Xi, Zefang Wang, Weiwei Zhao, Ju-Hyun Park, Kam Tuen Law, Helmuth Berger, László Forró, Jie Shan, and Kin Fai Mak. Ising pairing in superconducting nbse2 atomicÂ layers. *Nature Physics*, 12(2):139–143, Feb 2016.

[174] Xiaoxiang Xi, Liang Zhao, Zefang Wang, Helmuth Berger, László Forró, Jie Shan, and Kin Fai Mak. Strongly enhanced charge-density-wave order in monolayer nbse2. *Nature Nanotechnology*, 10(9):765–769, Sep 2015.

[175] Di Xiao, Gui-Bin Liu, Wanxiang Feng, Xiaodong Xu, and Wang Yao. Coupled spin and valley physics in monolayers of mos_2 and other group-vi dichalcogenides. *Phys. Rev. Lett.*, 108:196802, May 2012.

[176] Di Xiao, Wang Yao, and Qian Niu. Valley-contrasting physics in graphene: Magnetic moment and topological transport. *Phys. Rev. Lett.*, 99:236809, Dec 2007.

[177] Ying-Ming Xie, K. T. Law, and Patrick A. Lee. Topological superconductivity in eus/au/superconductor heterostructures. *Phys. Rev. Research*, 3:043086, Oct 2021.

[178] Jin-Peng Xu, Mei-Xiao Wang, Zhi Long Liu, Jian-Feng Ge, Xiaojun Yang, Canhua Liu, Zhu An Xu, Dandan Guan, Chun Lei Gao, Dong Qian, Ying Liu, Qiang-Hua Wang, Fu-Chun Zhang, Qi-Kun Xue, and Jin-Feng Jia. Experimental detection of a majorana mode in the core of a magnetic vortex inside a topological insulator-superconductor $bi_2te_3/nbse_2$ heterostructure. *Phys. Rev. Lett.*, 114:017001, Jan 2015.

[179] Hideki Yamamoto, Kenji Yoshii, Koichiro Saiki, and Atsushi Koma. Improved heteroepitaxial growth of layered nbse2 on gaas (111)b. *Journal of Vacuum Science & Technology A*, 12(1):125–129, 1994.

[180] J. T. Ye, Y. J. Zhang, R. Akashi, M. S. Bahramy, R. Arita, and Y. Iwasa. Superconducting dome in a gate-tuned band insulator. *Science*, 338(6111):1193–1196, 2012.

[181] P. Yu, J. Chen, M. Gomanko, G. Badawy, E. P. A. M. Bakkers, K. Zuo, V. Mourik, and S. M. Frolov. Non-majorana states yield nearly quantized conductance in proximatized nanowires. *Nature Physics*, 17(4):482–488, Apr 2021.

[182] Noah F. Q. Yuan and Liang Fu. Zeeman-induced gapless superconductivity with a partial fermi surface. *Phys. Rev. B*, 97:115139, Mar 2018.

[183] Ruoyu Yue. *Molecular Beam Epitaxy of Transition Metal Dichalcogenides*. PhD thesis, University of Texax at Dallas, Dallas, TX, December 2017.

[184] Ruoyu Yue, Yifan Nie, Lee A Walsh, Rafik Addou, Chaoping Liang, Ning Lu, Adam T Barton, Hui Zhu, Zifan Che, Diego Barrera, Lanxia Cheng, Pil-Ryung Cha, Yves J Chabal, Julia W P Hsu, Jiyoung Kim, Moon J Kim, Luigi Colombo, Robert M Wallace, Kyeongjae Cho, and Christopher L Hinkle. Nucleation and growth of WSe 2 : enabling large grain transition metal dichalcogenides. *2D Materials*, 4(4):045019, sep 2017.

[185] Hao Zhang, Chun-Xiao Liu, Sasa Gazibegovic, Di Xu, John A. Logan, Guanzhong Wang, Nick van Loo, Jouri D. S. Bommer, Michiel W. A. de Moor, Diana Car, Roy L. M. Op het Veld, Petrus J. van Veldhoven, Sebastian Koelling, Marcel A. Verheijen, Mihir Pendharkar, Daniel J. Pennachio, Borzoyeh Shojaei, Joon Sue Lee, Chris J. Palmstrøm, Erik P. A. M. Bakkers, S. Das Sarma, and Leo P. Kouwenhoven. Retraction note: Quantized majorana conductance. *Nature*, 591(7851):E30–E30, Mar 2021.

[186] Hao Zhang, Chun-Xiao Liu, Sasa Gazibegovic, Di Xu, John A. Logan, Guanzhong Wang, Nick van Loo, Jouri D. S. Bommer, Michiel W. A. de Moor, Diana Car, Roy L. M. Op het Veld, Petrus J. van Veldhoven, Sebastian Koelling, Marcel A. Verheijen, Mihir Pendharkar, Daniel J. Pennachio, Borzoyeh Shojaei, Joon Sue Lee,

Chris J. Palmstrøm, Erik P. A. M. Bakkers, S. Das Sarma, and Leo P. Kouwenhoven. Retracted article: Quantized majorana conductance. *Nature*, 556(7699):74–79, Apr 2018.

[187] Yuanbo Zhang, Yan-Wen Tan, Horst L. Stormer, and Philip Kim. Experimental observation of the quantum hall effect and berry's phase in graphene. *Nature*, 438(7065):201–204, Nov 2005.

[188] Feipeng Zheng, Xi-Bo Li, Peng Tan, Yiping Lin, Lingxiao Xiong, Xiaobo Chen, and Ji Feng. Emergent superconductivity in two-dimensional $nite_2$ crystals. *Phys. Rev. B*, 101:100505, Mar 2020.

[189] Benjamin T. Zhou, Noah F. Q. Yuan, Hong-Liang Jiang, and K. T. Law. Ising superconductivity and majorana fermions in transition-metal dichalcogenides. *Phys. Rev. B*, 93:180501, May 2016.

[190] You Zhou, Jiho Sung, Elise Brutschea, Ilya Esterlis, Yao Wang, Giovanni Scuri, Ryan J. Gelly, Hoseok Heo, Takashi Taniguchi, Kenji Watanabe, Gergely Zaránd, Mikhail D. Lukin, Philip Kim, Eugene Demler, and Hongkun Park. Bilayer wigner crystals in a transition metal dichalcogenide heterostructure. *Nature*, 595(7865):48–52, Jul 2021.